Coventry University

DOCTOR OF PHILOSOPHY

Mathematical modelling of contactless electromagnetic flow meters for liquid metals

Looney, Richard

Award date:
2018

Link to publication

General rights
Copyright and moral rights for the publications made accessible in the public portal are retained by the authors and/or other copyright owners and it is a condition of accessing publications that users recognise and abide by the legal requirements associated with these rights.

- Users may download and print one copy of this thesis for personal non-commercial research or study
- This thesis cannot be reproduced or quoted extensively from without first obtaining permission from the copyright holder(s)
- You may not further distribute the material or use it for any profit-making activity or commercial gain
- You may freely distribute the URL identifying the publication in the public portal

Take down policy
If you believe that this document breaches copyright please contact us providing details, and we will remove access to the work immediately and investigate your claim.

Download date: 29. May. 2021

Coventry University

School of Computing, Electronics and Mathematics

PhD Mathematics and Physics

Mathematical modelling of contactless electromagnetic flow meters for liquid metals

Author
Richard Looney

Supervisor
Dr. Jānis Priede

25th March 2018

Abstract

This work presents numerical analysis of contactless eddy current flowmetering methods including phase-shift and transient eddy current techniques. Simple 2D and axisymmetric theoretical models are considered where the flow is approximated by a solid conducting medium in the presence of a time varying magnetic field. A 3D model is presented which has been developed for the further improvement of these flowmetering techniques. The 3D model is designed to incorporate arbitrary exciting coils, in contrast to the fixed coils of the 2D models. The 3D model presented is verified against the previous 2D models.

The concept of a rescaled phase shift flowmeter, an improved phase shift flowmeter with reduced sensitivity to the variation of electrical conductivity of the liquid metals, is presented. This improved design incorporates the medium-induced phase shift between the sending and receiving coils to the measurement scheme, whilst the original design utilises only the phase shift induced by the flow between receiving coils. We show that the effect of conductivity to the flow-induced phase shift can be greatly reduced by rescaling with the medium-induced phase shift. Two rescalings are found: at lower ac frequencies of the applied field rescaling of the flow-induced phase shift with the square of the medium-induced phase shift effectively reduces the effect of conductivity in the former. At higher ac frequencies, the same is achieved by rescaling the flow-induced phase shift directly with the medium-induced phase shift.

Transient eddy current flowmeters operate by tracking eddy-current markers excited in the conducting flow by magnetic field pulses. The velocity is measured by tracking zero crossing points, spatial extrema or temporal extrema of the electromotive force induced by the eddy currents. It is found that temporal extrema of emf experience a time delay which depends on the conductivity of the medium and can be eliminated by taking the difference of multiple-coil measurements. Zero crossing points and spatial extrema travel synchronously with the medium. It is pointed out that symmetry of the system is essential to the operation of transient eddy current flowmeters. Asymmetry of a few percent in the eddy current distribution yields a drift in the detection point with a velocity corresponding to the magnetic Reynolds number $Rm = 0.1$. This means that a more accurate symmetric adjustment or calibration may be required for the transient eddy current technique to be reliable at lower velocities ($Rm \lesssim 1$).

The results of this study may be useful for designing next generation phase-shift and transient eddy-current flowmeters with higher accuracy and increased robustness to the variations of the electrical conductivity of liquid metal, which may be required in some metallurgical and other applications.

Contents

1 Introduction

The measurement of liquid metal flows in an accurate and reliable way is important to many metallurgical processes, such as dosing and casting, and also to the nuclear industry where molten metals are used as coolants for advanced reactors. There are many problems with the measurement of liquid metal flows using traditional flowmeters, including induction flowmeters, due to the problems associated with liquid metals such as chemical aggressiveness or high temperatures which can use corrosion and other contact problems. To solve the problems of contact with liquid metals contactless approaches have been developed for liquid metal flow measurement. Induction flowmeters have been made contactless by using capacitively-coupled electrodes [20, 27]. Most contactless electromagnetic flowmeters now operate based on effects related to the eddy currents, which are the loops of electrical current induced within the conducting flow by an applied magnetic field. Both the time variation of the magnetic field or the movement of the conductive media within a stationary field can cause these eddy currents. These eddy currents, by Lenz's law, will induce a magnetic field which will oppose the changes to the external field. The effect of this field can be measured outside of the flow thus avoiding the need for electrical contact with the liquid metal.

An issue which typically arises when taking measurements based on this induced magnetic field is the way in with velocity appears in the measurements. The velocity measurement that can be taken of the flow generally depend on the conductivity, as the value which is measured is determined by the product of conductivity and velocity and not by the flow velocity. System which measure the magnetic Reynolds number require calibration depending on the conductivity. This leads to another problem based on the thermal variation of conductivity. The main objective of this work is to identify measurement systems which are less affected by the conductivity of the liquid metal flow.

This thesis is split into 6 chapters. Following this introduction is a review of the development of liquid metal flow measurement, with special focus on the phase shift and transient eddy current flowmeters, this is accompanied by further discussion on the problems associated with liquid metal flow measurement. In chapter 3 the underlying equations which are used to develop the models presented later are introduced and discussed alongside discussion of boundary conditions typically found in the modelling of flows including those which will be used in this work. Chapters 4 and 5 introduce and implement two simple 2D models which leads to recommendations on measurement systems with reduced dependence on conductivity. Chapter 4 will focus of further development of the phase shift flowmeter approach whilst chapter 5 will focus on the pulsed field, or transient eddy current flowmeter. Both chapters include some extra material relating to the optimisation or sensitivities of the designs, with the important consideration of symmetry appearing in the latter chapter. Chapter 6 Introduces a further, fully three dimensional,

model which is designed to further investigate these optimisations, or sensitivities, by allowing more complete descriptions of the wire loops represented in the earlier models. The model presented in this chapter is a basis for further work, and could be used to further develop the ideas in the previous chapters. Finally a summary of the conclusions which were developed throughout the work is given by chapter 7.

2 Literature Review

In this section a historical background of the development of electromagnetic flowmeters for liquid metals, from the advent of electromagnetic flowmetering, is reviewed. Special attention is given to eddy current phase shift and pulsed field approaches which are developed later in this work. A review of other current developments in liquid metal flowmetering is given next. The section ends with a discussion of the general problems associated with the flowmetering of liquid metals.

2.1 History of electromagnetic flowmeters for liquid metals

The concept of electomagnetic flow measurement dates from Faraday's time. The basic principles are documented from this time, for example in Faraday's own experimental researches in electricity [14] originally published in 1832. In this historic work the concept of magnetic induction is well defined. Faraday is known to have attempted to take an electromagnetic flow measurement of the River Thames. Faraday's experiment consisted of measuring the voltage induced between a pair of electrodes inserted either side of the rivers flow. The fundamental idea being that the conductive flow of the River in the presence of the Earth's magnetic field will induce a voltage across the flow, between the two electrodes. In an idealised model the magnitude of this voltage will be proportional to the flow rate. This type of flowmeter has become the standard electromagnetic flowmeter, generally referred to as an induction flowmeter.

There appears to be little development in the field from the 1830s until a novel application of the induction flowmeter was patented in 1917 [36]. The device specified in the patent measures the velocity of a ship relative to the body of water it is upon. The measurement is taken using an outboard induction flowmeter, measuring how fast the water is flowing in the ships frame of reference. Publications from the 1930s start to introduce the use of induction flowmeters on artificial flows. The publications from the early 1930s appear to be the first which consider flows other than water. For example the experiments of Williams with copper sulphate[46] which also not only suggests a liquid metal flow, in the form or mercury, as a means to reduce sensitivity to spurious effects but also recognises the potential downfall that electrodes introduced into the liquid can cause a disturbance to the flow. It was around this time that publications for the application of electromagnetic flowmeters for blood flow measurement start, for example the Faraday type induction flowmeter was employed in [22]. In this work Kolin recognises that the electromagnetic flowmeter has the advantage of providing instantaneous results.

With the advent of nuclear reactors the need for liquid metal systems developed, for example the sodium-potassium alloy cooled Dounreay Fast Reactor which started operation in 1959 [8]. The development of control systems for these fast reactors required accurate measurement of of the liquid metal coolants and as such flow meters for liquid

metals became a topic of interest and remained so for many years with investigations continuing 20 years later [3].

Today there is still active development in the flowmetering of liquid metals for nuclear control applications. An example of current study of liquid metal flows is given in [6], in which the current state of the study of cooling blankets for fusion reactors is outlined. It is stated in this work that for reliable blanket designs flow distributions will need to be confirmed by experimental data, showing the need for liquid metal flow measurement in research applications. For the new generations of fast breeder reactors, the feasibility of eddy current flowmeters has been shown both numerically through simulation and experimentally in the Phenix reactor [39]. And more recently the application of eddy current flowmeters to detect air pockets in coolants of the next generation of fast breeder reactors has been presented [25]. This shows the flexibility of some liquid metal flow measurement techniques by utilising a flowmeter as a method for detecting the existence of a multi phase flow.

2.1.1 Eddy Current Flowmeters

The development of eddy current flowmeters for liquid metals followed the advent of flowmetering for liquid metals in the 1950s. The use of eddy current, or induced field, flowmeters which measure the the flow-induced perturbation of an externally applied magnetic field can be found in a patent for 1948 [26]. The device presented has a sensor within a streamlined capsule submerged within the flow, the sensor consists of a series of sending and receiving coils. The sending coils generate a magnetic field which due to eddy currents will be advected with the flow and the displacement of this field leads to induced voltages in the receiving coils.

The first appearance of utilising a phase shift for flow measurement appears to come from advances in blood flow measurement [29], where the phase shift is induced by imperfections in construction of the flowmeter . Further use of the induced magnetic field for liquid metal flow measurement can be seen in[9]where a sensor is immersed in a capsule similar to that of Lehde and Lang's 1948 patent. The significance of this paper to this work is the suggestion that phase measurements taken along side magnitude measurements can be used to determine flow velocity independently of conductivity.

A design of an eddy current flowmeter which moved from the submerged capsule can be found in [45] where the flow passes through coils. The coaxial coils are introduced so that the fluid passes through the region with the strongest magnetic field. This paper also highlights a short falling of the measurement technique which is the dependence of the measurement scheme on the temperature, or electrical conductivity, of the fluid. Further work on eddy current flowmeters can be seen in [17] which presents the idea of the arrangements of external sending and receiving coils being utilised such that only

the signal induced by the flow is measured and not any currents induced directly by the applied field. The paper suggests that low frequency measurements, by penetrating the medium well, have an averaging effect on the flow profile which could provide a measure of volumetric flow rate. This idea of optimising the arrangement of electrodes in a contactless measurement scheme depending on the nature of the applied field is further discussed in [20], however in this paper this idea is applied to a transverse exciting field.

Consideration to eddy current flowmeters is given in Shercliffs text [35] under the name of the induced field flowmeter and the problem of conductivity dependence is discussed; it is suggested that empirical calibration may be unavoidable. Many novel uses of the induced field have been developed such as flow tomography [38] and applications to multiphase flow [7], which appears more recently in [25], were published in the early 2000s. The re-imagination of a force detecting induced field flowmeter under the new name of Lorentz force velocimetry [41] seems to have heralded a resurgence in the topic of contactless flow measurement.

The concept of a phase shift flowmeter was introduced in [31]. The phase shift flowmeter operates on the principle that the conducting flow disturbs not only the amplitude but also the phase distribution of the alternating applied field. This technique has the advantage of being robust to many disturbances due to the phase measurements being a ratio of field strengths and not absolute values, however the problem of conductivity variation still exists. The robustness of the phase shift flowmeter to external disturbances such as electromagnetic disturbance and noise has been demonstrated in [5]. A recent experimental investigation into measurements of liquid sodium loops utilised a phase shift flowmeter which was submerged in a capsule [23]. This paper also shows the sensitivity of the device to physical imperfections, which can be addressed to some extent by calibration, and the problem of thermal variation of conductivity.

2.1.2 Pulsed Field Flowmeters

The idea of modifying the design of an induction flowmeter to replace the harmonically alternating applied field with a pulsed field approach is proposed in [37] where it is applied to weakly conducing flows, specifically referring to blood flow measurements . The square-wave approach utilised in this paper was suggested as a compromise between the DC approach, where polarisation of the electrodes and environmental electrical noise are problematic, and an AC approach, where a transformer effect can generate spurious signals.

The application of a pulsed magnetic field to a strongly conducting flow, such as a liquid metal flow was proposed in [47] which again used a transverse field. In this work the authors recognise the potential of a pulsed field approach in removing conductivity from the measurement scheme. The pulsed approach appears again in a contactless way

Some materials have been removed due to 3rd party copyright. The unabridged version can be viewed in Lancester Library - Coventry University.

w e dependence of the measurement scheme on conductivity, and its thermal variation. The paper recognises that the removal of conductivity is a matter for either calibration or additional devices.

The use of a pulsed field with liquid metals in a contactless approach is omitted from the discussions in Shercliff's comprehensive text [35]. This is likely due to the majority of works discussed in this section being published after the books first printing thus the concept of a pulsed field approach not being well formed at the time. The pulsed field approach has reappeared relatively recently under the guise of transient eddy current flowmetering with both external coils [18] and with coils in an immersed capsule [24], both designs operate by exciting and then tracking transient eddy current markers as they are carried along by the moving conductor.

2.2 Some Recent Development in Liquid Metal Flow Measurement

In addition to the eddy current and pulsed field flowmeters discussed above there are two other popular designs of contactless flow measurement for liquid metal applications. The two methods, which both appear in Shercliff's well known text [35], are rotary flowmeters and the Lorentz force flowmeter. The Lorentz force flowmeter originally appeared under the name of force flowmeter the addition of Lorentz to the name was adopted more recently.

The rotary flowmeter can be found in a patent [34] from around the time liquid metal

flow measurement became of interest. The patent presents a design with two flywheels in a spool type arrangement as shown in figure 1. The two wheels have magnets attached to their inner faces with alternating orientations around the wheel. The wheels are attached to an axle in such a way that opposite polarities face each other between the two wheels. The patent claims that speed of rotation to be a measure of fluid flow rate. The exact pattern of magnets varies between different works however the general rule of the layout given in the patent above is maintained. This layout has the direction the poles of the magnets alternating around the axis of rotation. Where multiple disks are utilised, with the fluid flowing between the disks, the magnets are oriented so that opposite poles face each other across the flow. The process of modelling these rotary flowmeters was approached in [4] which include single disk designs. This paper also gives some discussion towards the problem of friction in the bearing and the advantages of it being negligible relative to the torque acting on the measurement system. The advantages of this design including both a reduced dependence on conductivity and the ability to use electrically conducting pipe walls.

A novel rotary flowmeter design where the flywheel is replaced by a cylindrical magnet which is magnetized perpendicularly to its axis is presented in [30, 32]. The magnet is allowed to freely rotate around this axle upon which the magnet is mounted. The single magnet design has the advantage of, in the limit of negligible friction in the bearing, having a contactless measurement technique which is not dependent on conductivity. The rotary flowmeter is not a perfect solution to the problem of liquid metal flow measurement due to the slow response time to changes in the flow which is due to inertia in the flywheel, also a problem which is more pronounced in rotary flowmeters is the problem of mechanical wear of moving parts.

The force flowmeter has become a topic of interest with recent developments being carried out under the name Lorentz force velocimetry [41, 42]. Lorentz force velocimetry is a contactless flowmetering technique which operates by measuring the Lorentz force exerted on a magnet, or coil, by an induced magnetic field. A typical setup is shown in figure 2. This measurement system comes with the problems of other contactless techniques, specifically the problem of conductivity, with the Lorentz force being proportional to the Magnetic Reynolds number and not just the velocity. One of the major issues with the use of the Lorentz force for measurement is that it is weak in relationship to the applied field. In spite of this it seems reasonable to assume that attempting to measure lower conductivity fluids will lead to weaker induced fields and therefore weaker forces to measure. Despite this limitation there has been developments showing that the technique can be applied to fluids with conductivity many orders of magnitude lower that typical liquid metals [44]. The paper demonstrates the method for conductivities of order 10^0 S/m and suggests for practical applications conductivities of magnitude 10^{-3} S/m, and in laboratory applications 10^{-6} S/m, could be measured for comparison typical liquid

Some materials have been removed due to 3rd party copyright. The unabridged version can be viewed in Lancester Library - Coventry University.

F
f

m 10^6

The Lorentz force velocimetry approach has been applied to flow tomography [19] where a series of localised measurements were shown to detect two large jets in the flow profile, which were introduced by an upstream obstruction. More recently a novel method utilising time of flight measurements with Lorentz force flowmeters had been presented as a method to remove the conductivity dependence from the measurements [11, 12]. This is achieved by the use of a pair of Lorentz force velocimetry and a probe. The probe creates vortices in the flow which are detected by both the flowmeters, the time of flight of the vortex gives a measurement of the velocity of the fluid.

2.3 The Difficulties of Liquid Metal Flow Measurement

The measurement of flow rates of liquid metals presents some challenges which are not present when dealing with other media. The first major difference which is considered here is that the conductivity of liquid metals is typically significantly higher than that of non metallic fluids. This higher conductivity leads to differences in how electromagnetic flowmeters are designed for liquid metals. The higher conductivity leads to some electromagnetic effects becoming more significant. For example, when a high frequency alternating magnetic field is used the skin effect can prevent the field from effectively penetrating the fluid [2]. The applied field will introduce eddy currents within the flow

these eddy currents can cause a distortion, or dampening, of the applied magnetic field [35]. Conversely the influence of the magnetic field on the body of the flow is also much higher with the increased conductivity typical of liquid metals this is likely to cause a pressure drop across the flowmeter and may disrupt the flow profile. The skin effect effect can be neglected with low enough magnetic Reynolds numbers, typically a value of $Rm \ll 1$ where inductive effects are outweighed by magnetic diffusion.

In non-metallic fluid flow the use of alternating magnetic fields has some advantages. For example DC fields can lead to temperature gradients between the electrodes causing thermoelectric effects which can adversely affect the flowmeters performance. With an alternating field the thermoelectric potential will be averaged out. They are also not a concern when considering liquid metals as the higher thermal conductivity will reduce temperature gradients.

There are physical effects which occur with liquid metal flows and must be considered when designing flow meters. These effects include the temperature of the flow, which for an application such as nuclear cooling is likely to be high which in turn can lead to increased mechanical wear on components [13]. This is the main reason more traditional measurement systems such as differential pressure flowmeters and Faraday type induction flowmeters are unsuited to liquid metal applications. Another property of many liquid metals is chemical volatility. Great care has to be given to some liquid metals, as for example, sodium is highly oxidising and can react explosively with water. Gallium rapidly weakens aluminium with the capillary effect leading to damage far from the interface of the two materials [21]. Traditional measurement techniques, such as particle image velocimetry [15] and optical Doppler tomography [43, 33], are not possible with liquid metal flow due to the materials opacity.

Many of the problems above are mitigated by using a contactless approach which, by using low frequency applied fields, can be designed to avoid problems such as the skin effect and magnetic braking of the flow. However, there is currently no general solution for such a flowmeter. A significant reason for this is that most contactless flowmeter measurements rely on induced voltages which are dependent on both the velocity and conductivity of the flow. Many flowmeter designs mitigate the dependence on conductivity by calibration. However the thermal variation of conductivity can disrupt this calibration. This thermal variation of the conductivity of liquid metals can be characterised by the Wiedemann–Franz law , $\frac{\kappa}{\sigma} = LT$, where κ is the thermal conductivity, σ is the electrical conductivity, L is the Lorentz number ($2.44 \times 10^{-8} W\Omega K^{-2}$) and T is the temperature. As an example of typical values the electrical conductivity of bismuth for industrial applications for the temperature range $545 - 1423K$ can be found in [16]. The conductivity of bismuth at $600K$ is given as 7.56×10^5 and falls to 6.04×10^5 at $1200K$.

3 Fundamental Equations

3.1 Equations Governing Electrodynamics

Consider a particle carrying a charge q moving with a velocity $\vec{v}$. There are three electromagnetic forces which can act upon the particle,

$$\vec{F} = q\vec{E}_s + q\vec{E}_i + q\vec{v} \times \vec{B}, \tag{1}$$

where $\vec{E}_s$ is the electrostatic field and $\vec{E}_i$ is the electric field induced by changes in the magnetic field. The first term relates to the electrostatic field represents the electrostatic, or Coulomb, force. This force is the mutual attractions, or repulsion, between electric charges. The term relating to the induced electric field is specific to the presence of a magnetic field with varies with time. The final term is caused by of the motion of a charge relative to a magnetic field, which is called the Lorentz force.

At this point to further consider the electrostatic field two laws shall be introduced, namely Coulomb's law and Gauss' law. Firstly, Gauss' law states that the electric flux through a hypothetical closed surface is equal to the net electric charge within that closed surface divided by ϵ_o, the permittivity of free space.

$$\vec{\nabla} \cdot \vec{E}_s = \frac{\rho}{\epsilon_0},$$

where ρ denotes the charge density. Coulomb's law states that the magnitude of electrostatic attraction forces between two point charges is inversely proportional to the square of the distance between them and directly proportional to the product of the magnitudes of the charges. A consequence of this is that the static electric field is irrotational

$$\vec{\nabla} \times \vec{E}_S = 0.$$

As the field is irrotational it can be defined as the gradient of a potential, $\vec{E}_s = -\vec{\nabla}\phi$, where ϕ is the electrostatic potential.

The induced field is governed by Faraday's law of induction, which will be generalised later in the Maxwell-Faraday equation;

$$\vec{\nabla} \times \vec{E}_i = -\frac{\partial \vec{B}}{\partial t}. \tag{2}$$

It is also worth notice that the induced field is divergence free as there are no sources within it giving

$$\vec{\nabla} \cdot \vec{E}_i = 0.$$

The total electric field can be defined as the sum of the electric fields, $\vec{E} = \vec{E}_s + \vec{E}_i$

and has the properties:

$$\begin{aligned} \vec{\nabla} \cdot \vec{E} &= \frac{\rho}{\epsilon_0} \\ \vec{\nabla} \times \vec{E} &= -\frac{\partial \vec{B}}{\partial t} \end{aligned} \tag{3}$$

We can now simplify equation (1), by using the total electric field, giving the Lorentz force law below

$$\vec{F} = q(\vec{E} + \vec{v} \times \vec{B}) \tag{4}$$

where $\vec{F}$ is the force acting upon the charge q. The Lorentz force law, when combined with the Maxwell equations, gives the foundations of classical electromagnetism.

3.2 The Maxwell Equations

The Maxwell equations are a set of partial differential equations underlying classical electromagnetism. The equations consist of Gauss' law, Gauss' law for magnetism, the Maxwell-Farday equation and Ampère's circuital law.

3.2.1 Gauss' Law

Gauss' law has been introduced above and relates the distribution of electric charges to the resulting electric field. The law equates the electric flux,$\vec{\Phi}_E$, through a closed surface S to the to total charge Q contained by the volume V bounded by that surface divided the permittivity of free space,

$$\vec{\Phi}_E = \frac{Q}{\epsilon_0}. \tag{5}$$

The electric flux can be expressed as the surface integral of the electric field,

$$\vec{\Phi}_E = \oiint_S \vec{E} \cdot d\vec{S} \tag{6}$$

where $d\vec{S}$ represents the infinitesimal area which is an element of the surface S. Divergence theorem, often referred to a Gauss' theorem relates the flux out of a region to the the sum of all sinks and sources within the region. This is achieved by equating the flux of a vector field through a closed surface to the divergence of said field over the region enclosed by the surface, in the case of $\vec{E}$ this gives

$$\oiint_S \vec{E} \cdot d\vec{S} = \iiint_V \vec{\nabla} \cdot \vec{E} dV.$$

Substituting the volume integral for the electric flux in (5) gives us Gauss' law in the following form

$$\iiint_V (\vec{\nabla} \cdot \vec{E}) dV = \frac{Q}{\epsilon_0},$$

which can be modified to the form used earlier in equation (3) by moving to charge density ρ which gives the charge when integrated over the volume $Q = \iiint_V \rho dV$.

$$\iiint_V (\vec{\nabla} \cdot \vec{E}) dV = \frac{1}{\epsilon_0} \iiint_V \rho dV$$

the integrands can now be equated giving the differential form of Gauss' law which relates the divergence of the electric field to the total charge density

$$\vec{\nabla} \cdot \vec{E} = \frac{\rho}{\epsilon_0}. \tag{7}$$

3.2.2 Gauss' Law for Magnetism

Gauss' law for magnetism simply states that a magnetic field must be divergence free

$$\vec{\nabla} \cdot \vec{B} = 0. \tag{8}$$

This condition states that a magnetic field has no sinks or sources, that is to say that field lines form closed loops. This is equivalent to stating that a magnetic field is a solenoidal vector field. A more physical interpretation of this is that there are no magnetic monopoles, thus no sources, and a infinitesimal element generating a magnetic field should be represented as a dipole, analogous to how magnets always have a north and a south pole.

3.2.3 Faraday's Law (the Maxwell-Faraday equation)

Faraday's law, or more specifically Faraday's law of induction, states that the induced electromotive force in a closed circuit equals the negative of the rate of change over time of the magnetic flux enclosed by the circuit. The magnetic flux Φ is calculated in a similar way to the electric flux in equation (6). However as we will be considering the rate of change over time of the flux we will specify the time dependence of both the magnetic field and the surface. We may also note that the integral is no longer over a closed surface,

$$\vec{\Phi} = \iint_{S(t)} \vec{B}(\vec{r}, t) \cdot d\vec{S}$$

where $\vec{r}$ is the position vector. The electromotive force (e.m.f.) caused by the change in flux can be defined by

$$\mathcal{E} = -\frac{d\Phi}{dt}. \tag{9}$$

aA generalisation of Faraday's law is provided by the Maxwell-Faraday equation, which was introduced in equation (2). It states that a time-varying magnetic field will always accompany a spatially varying electric field and vice versa. It is worth noticing that the differential form of the Maxwell-Faraday equation,

$$\vec{\nabla} \times \vec{E} = -\frac{\partial \vec{B}}{\partial t},$$

is a weaker definition than the integral form as it is limited to the electric field induced by a time-varying magnetic field as claimed in [10]. The integral form gives the electromotive force which is generated in a conductor by either a time varying magnetic field or the motion of the conductor relative to the magnetic field,

$$\oint_{\partial S} \vec{E_l} \cdot d\vec{l} = -\int_S \frac{\partial \vec{B}}{\partial t} \cdot d\vec{S} \tag{10}$$

where ∂S is the closed contour bounding the surface S and $d\vec{l}$ are the infinitesimal line elements comprising ∂S. $\vec{E_l}$ refers to the effective electric field for each line element which is equivalent to the field measured in the frame of reference moving with the line element $d\vec{l}$ and can be defined as $\vec{E_l} = \vec{E} + \vec{u_l} \times \vec{B}$ where $\vec{u_l}$ is the velocity of the line element. The differential form can be derived from the intergral form by employing the Kelvin-Stokes theorem, which equates the integral over a surface of the curl of a vector field to the line integral of the same field around the boundary of the surface. Applied to the electrostatic field considered here the Kelvin-Stokes theorem yields

$$\oint_{\partial S} \vec{E} \cdot d\vec{l} = \oint_S \vec{\nabla} \times \vec{E} \cdot d\vec{S} \tag{11}$$

Here we have returned to the simplified case where the electromotive force is the result of a time dependent magnetic field and the loop is not in motion. With this assumption combining equations (10) and (11) yields

$$\oint_S (\vec{\nabla} \times \vec{E}) \cdot d\vec{S} = -\int_S \frac{\partial \vec{B}}{\partial t} \cdot d\vec{S}.$$

Equating the integrands yields the differential form of the Maxwell Faraday given in equation (2), thus showing that as described above the differential form is weaker than the integral form as it requires more assumptions and thus is valid in less situations.

3.2.4 Ampère's Circuital Law

Ampère's circuital law equates the line integral of a magnetic field around a closed loop to the current flowing around the loop. The integral form can be written as

$$\oint_{\partial S} \vec{B} \cdot d\vec{l} = \mu_0 \iint_S \vec{j} \cdot d\vec{S} \tag{12}$$

where $\vec{j}$ is the current density and μ_0 is the permeability of free space. As with the Maxwell-Faraday equation the Kelvin-Stokes theorem can be used to move to the differential form. Applying the Kelvin-Stokes theorem to the magnetic field instead of the electrostatic field yields

$$\oint_{\partial S} \vec{B} \cdot d\vec{l} = \oint_S (\vec{\nabla} \times \vec{B}) \cdot d\vec{S},$$

this can be substituted into equation (12) and then the integrands can be equated yielding the differential form of Ampère's circuital Law

$$\vec{\nabla} \times \vec{B} = \mu_0 \vec{j}. \tag{13}$$

We now consider the limitations of this law in the form presented above. In this form the law is accurate only in an magnetostatic environment, which is to say that currents in the system do not change with time. This can be shown by taking the divergence of (13)

$$\vec{\nabla} \cdot (\vec{\nabla} \times \vec{B}) = \mu_0 \vec{\nabla} \cdot \vec{j}$$

which as the divergence of a curl is identically zero,

$$\vec{\nabla} \cdot (\vec{\nabla} \times \vec{B}) = 0$$

implies that the current density is also divergence free,

$$\vec{\nabla} \cdot \vec{j} = 0.$$

While this is possible it is not the general case, this can be seen by considering the continuity equation for electomagnetic charge

$$\vec{\nabla} \cdot \vec{j} = -\frac{\partial \rho}{\partial t}$$

where ρ is the charge density. This continuity equation is more fundamental and is based on charge conservation, in physical terms it means that a charge leaving a differential volume leads to a reduction in the charge contained in the volume, thus a negative rate of change for the charge density. It can be seen that Ampère's circuital law as stated above

agrees with charge conservation when there is a constant charge density, and thus the magnetostatic condition for the law is satisfied. A modification to Ampère's circuital law known as Maxwell's correction provides an extension of the law beyond the magnetostatic environment. The law with the extension, in differential form, becomes

$$\vec{\nabla} \times \vec{B} = \mu_0 \vec{j} + \mu_0 \epsilon_0 \frac{\partial \vec{E}}{\partial t}. \tag{14}$$

The addition term introduced by Maxwell's correction, $\epsilon_0 \frac{\partial \vec{E}}{\partial t}$, is called the displacement current and by again taking the divergence,

$$\vec{\nabla} \cdot (\vec{\nabla} \times \vec{B}) = \mu_0 \vec{\nabla} \cdot (\vec{j} + \epsilon_0 \frac{\partial \vec{E}}{\partial t}),$$

we obtain

$$\vec{\nabla} \cdot \vec{j} = -\epsilon_0 \vec{\nabla} \cdot \frac{\partial \vec{E}}{\partial t}$$

applying Gauss's law given in equation (7) which equates the divergence of the electric field to the charge density divided by the permittivity of free space yields

$$\vec{\nabla} \cdot \vec{j} = -\epsilon_0 \vec{\nabla} \cdot \frac{\partial \vec{E}}{\partial t} = -\frac{\partial \rho}{\partial t}$$

thus showing Maxwell's correction satisfies the continuity equation for electromagnetic charge.

3.2.5 Ohm's Law

Ohm's Law, which states that in a conductor the current between two points is proportional to the voltage across the two points with the constant of proportionality being the reciprocal of the electrical resistance of the conductor. This can be generalised to a current density being proportional to the electric field, with the constant of proportionality being the conductivity of the material,

$$\vec{j} = \sigma \vec{E}.$$

When the conductor is travelling within a magnetic field the Lorentz force term must be added to account for the motion induced currents in the charge carrying medium. Giving the form of Ohm's Law which will be used in this work

$$\vec{j} = \sigma(\vec{E} + \vec{v} \times \vec{B}) \tag{15}$$

this form is commonly referred to as Ohm's law with magnetic effects.

3.2.6 The Vector Potential

Gauss's Law for magnetism shows that magnetic field are solenoidal fields and thus can be defined by a vector potential. A vector potential is defined as a vector field whose curl is a given vector field, i.e. the magnetic field, in our case

$$\vec{\nabla} \times \vec{A} = \vec{B},$$

where $\vec{A}$ is the magnetic vector potential. There is also some freedom in the definition of the vector potential, this comes about as it is defined by its curl. Consider the Maxwell-Faraday equation in terms of the vector potential

$$\vec{\nabla} \times \vec{E} = -\vec{\nabla} \times \frac{\partial \vec{A}}{\partial t}$$

which as the curl of a gradient is zero leads to many solutions,

$$\vec{E} = -\frac{\partial \vec{A}}{\partial t} - \vec{\nabla}\phi \tag{16}$$

where ϕ is the scalar potential, which is a continuously differentiable scalar function. The scalar potential can be further defined as $\phi \rightarrow \phi + f(t)$ where f is an arbitrary continuously differentiable scalar function. This property is referred to as gauge freedom or gauge invariance. Later in this work the gauge invariance of the vector potential field is exploited to simplify calculations (see equation (24) and following).

3.3 Boundary Conditions

Boundary conditions are essential to completely define a problem. The boundaries which are typically considered can include the hypothetical surfaces where fluid enters or leaves the system and interfaces between different materials. The interfaces between different materials will typically represent parts of the model such as pipe walls where there are materials adjacent with different properties, such as velocity and electrical conductivity. Whilst in the models presented in this work a very simplified consideration is given here to some important potential boundary conditions, which could be added to future developments of the models.

This section will discuss some important boundary conditions. Firstly, the electromagnetic boundaries at the pipe walls will be presented. Following this the interfacial conditions which will be used later in this work are introduced. Finally, some geometric boundaries are discussed, including symmetric and periodic conditions.

In the models used in this work, the boundaries are relatively simple, the only physical boundaries that exist are between free space and the conducting medium. There are also

boundaries caused by the calculations which tie together different regions of behaviours.

3.3.1 Electromagnetic Boundary Conditions

There are two formulations of electromagnetism, $(\vec{E}, \vec{B})$ the electric and magnetic fields and $(\vec{A}, \varphi)$ the magnetic vector potential and magnetic scalar potential. Both of these formulations are rigorous and complete. This work is based on the $(\vec{A}, \varphi)$ formulation however the $\vec{B}$ field is also considered in some cases. As such boundary conditions are only required for $\vec{A}$ and φ are needed. The boundary conditions on A and φ which are utilised in this work are derived from the continuity of $\vec{A}$ across an interface and also its non-tangental derivatives at the interface.

The nature of the pipe walls is also important in modelling magnetic fields. In the relatively simple case of non-conducting walls there can be no current flow between the fluid and the wall. Hence the component of the current normal to the wall must be zero

$$\vec{j} \cdot \vec{n} = 0. \tag{17}$$

The condition for the electrostatic potential is derived from equations 15 & 16 which specifies the derivative normal to the boundary to be,

$$\frac{\partial \phi}{\partial n} = \partial_t A_n + \vec{n} \cdot \vec{r} \times \vec{B} = (\partial_t A_n + \vec{B} \cdot \vec{n} \times \vec{r})|_S. \tag{18}$$

In the case of conducting walls, with a non-zero electrical conductivity σ_w, there are two boundaries to consider: the wetted surface and the dry surface of the wall. Inside the conducting wall we will have

$$\vec{j} = -\sigma_w \vec{\nabla} \phi_w$$

where ϕ_w is the electro static potential within the wall. As the wall is at rest the Poisson equation

$$\vec{\nabla}^2 \phi = \vec{\nabla} \cdot (\vec{v} \times \vec{B}) \tag{19}$$

which can be derived by taking the divergence of Ohms Law (15), yields

$$\vec{\nabla}^2 \phi_w = 0 \tag{20}$$

in the pipe wall. The dry surface acts in the same way as the non conducing walls with being subject to equations (17) and (18). The boundary at the wetted surface is subject to the the two following conditions. Firstly, the potential difference normal to and across the boundary gives

$$\phi - \phi_w = \sigma \sigma_w \frac{\partial \phi}{\partial \vec{n}}$$

and secondly the continuity of the current normal to and across the boundary yields

$$\sigma \frac{\partial \phi}{\partial \vec{n}} = \sigma_w \frac{\partial \phi_w}{\partial \vec{n}}.$$

These two conditions are sufficient to solve equations (19) and (20) across the boundary.

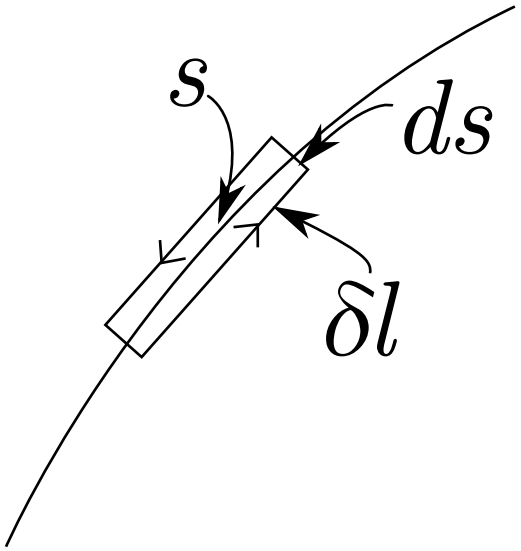

Figure 3: Schematic of the region,s, which appears at the pipe wall and is discussed in the context of the jump condition of the magnetic field

The jump condition for the tangental electric field will now be specified. The fomulation utilises equation 11 and equation 10 which when combined yield

$$\oint_S \vec{\nabla} \times \vec{E} \cdot d\vec{s} = \oint_{ds} \vec{E} \cdot d\vec{l} = \oint_s \frac{\partial \vec{B}}{\partial t} \cdot d\vec{S} \to 0$$

as the length of the section, shown in figure 3, of surface tends to zero, $dl \to 0$ then $[E_T]$, the change in the tangental component of the electic field across the surface, is seen to be zero.,

$$[E_T]dl = 0 \Rightarrow [E_T] = 0.$$

3.3.2 Interfacial Conditions

Interfacial conditions occur between different different regions of the model, such as at the interface between the conducting media and either a pipe wall or free space. The boundary conditions imposed at these interfaces ensure the continuity of the magnetic field components. The condition is that the vector potential of the magnetic field must be continuous across the interface;

$$(\vec{B}_I - \vec{B}_O) \cdot \vec{n} = 0$$

where $\vec{B}_I$ and $\vec{B}_O$ are the vector potentials either side of the boundary and $\vec{n}$ is the vector normal to the boundary.

3.3.3 Symmetry Conditions

Symmetry conditions are conditions imposed on an axis of symmetry. One such boundary is an axis boundary such as that found at $r = 0$, in cylindrical coordinates, with an azimuthally invariant model. In this cylindrical system the value at the axis must be regular and uniquely defined for all angles θ. The solution to this is that the azimuthal component must be equal to zero such that is does not vary with θ. In 2D this can be seen by imposing an odd function between the x and $-x$ axis which also ensured a zero value at the axis.

In the axisymmetric cylindrical case both the magnetic field and velocity field require zero valued normal components at the axis. However, the component of either field along the $r = 0$ axis is not required to be zero valued. Symmetry boundary conditions are typically used to reduce the computational requirement of a model by exploiting or imposing symmetries in the fields and the geometry.

3.3.4 Periodic Boundary Conditions

Another example of a geometry defining boundary is periodic boundary conditions these again can reduce computational effort. Periodic conditions are defined by matching field values and derivatives at either end of the calculation domain along the axis where the periodicity is present. Periodicity is present in the models later in this thesis however it is not included by design and is imposed due to the use of Fourier transforms. The region of interest is relatively far from the periodic boundary and the results of the models will not significantly affected by their usage. Due to the semi-analytic nature of the models presented in this work there is no requirement for a calculation domain to be specified and the fields can be directly calculated at the required location.

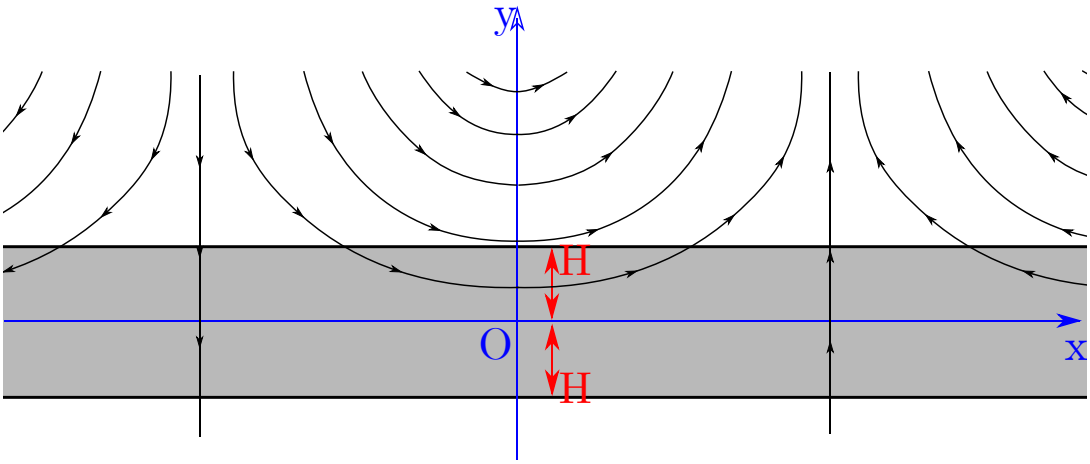

Figure 4: Schematic diagram for the model with the applied field taking the form of a harmonic wave.

4 Rescaled Phase Shift Flowmeter

The phase shift flowmeter as introduced in [31] has become a industrially available measurement method for liquid metal flows. The problem of the thermal variation of conductivity leading to a measurement scheme which is dependent not only on the flow rate but also on the temperature of the conducting medium has been discussed in section 2.3. The purpose of this chapter is to introduce a method which will be demonstrated theoretically to reduce the conductivity dependence of the measurement scheme. The idea behind the method is that phase shifts can be induced not only due to the flow of the medium but also due to the presence of the conducting medium itself. This phase shift induced by the presence of the medium will depend predominately on the conductivity of the medium and as such will be used to rescale the measured phase shift thus reducing the conductivity dependence. This chapter is split into three sections. Firstly the derivation for a two dimensional model for the phase shift flowmeter is presented, with a couple of different exciting fields. Secondly the results of this model are presented including investigating both the rescaling for the phase shift and some physical properties. The chapter will end with a brief summary of the findings.

4.1 Derivation

The model considered in this chapter, which is shown in figure 4 consists of a layer of conducing media of width $2H$ in the presence of an imposed magnetic field. The model is presented in Cartesian coordinates, with axes x and y oriented along the length of the conducting medium and across its width respectively. The model will be considered with 2 exciting fields. Firstly, the field is a standing harmonic wave applied from above the layer as shown in figure 4. The second field is generated by a coil represented by a couple of straight wires oriented along the z axis with oppositely flowing alternating currents.

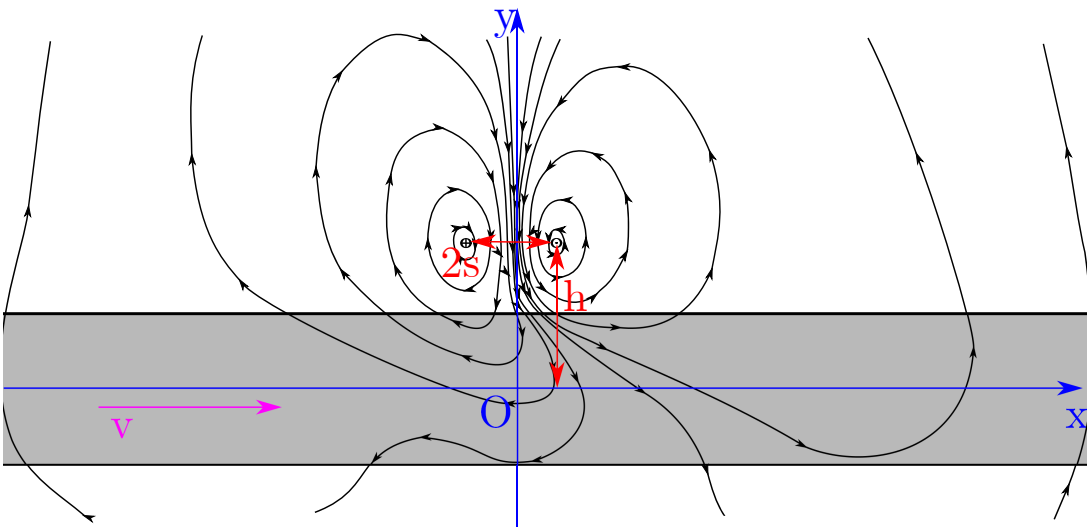

Figure 5: Schematic diagram for the model with the applied field generated by two straight wires with oppositely travelling currents.

The wires are located a distance of h above the x axis with a distance of $2s$ between them, as shown in figure 5.

To derive the model we consider a conducting medium, with electrical conductivity σ, moving with velocity V in the x direction, such that $\vec{v} = \vec{e}_x V$. The exciting field, with induction $\vec{B}$, is alternating harmonically with angular frequency ω.

The Maxwell-Faraday equation introduced in section 3.2.3 gives the electric field induced in the conducting medium by the exciting field

$$\vec{E} = -\nabla\Phi - \partial_t \vec{A} \tag{21}$$

where $\vec{A}$ is the vector potential of the magnetic field, given by $\vec{B} = \nabla \times \vec{A}$, and where Φ is the electric potential.

Ohm's law gives the density of the electric current in the moving medium,

$$\vec{j} = \sigma(\vec{E} + \vec{v} \times \vec{B}), \tag{22}$$

where σ is the conductivity of the medium. This can be presented in terms of the electric and vector potentials as

$$\vec{j} = \sigma(-\nabla\Phi - \partial_t A + \vec{v} \times \nabla \times \vec{A}) \tag{23}$$

The gauge invariance of $\vec{A}$ is used to specify its divergence as

$$\vec{\nabla} \cdot \vec{A} = -\mu_0 \sigma(\Phi - \vec{v} \cdot \vec{A})$$

where μ_0 is the vacuum permeability. This defines the electric potential as

$$\Phi = \vec{v} \cdot \vec{A} - \frac{1}{\mu_0 \sigma} \nabla \cdot \vec{A} \tag{24}$$

which simplifies the derivation of the advection diffusion equation below.

Now the advection diffusion equation can be derived, to do this we shall start with Maxwell's equation

$$\vec{j} = \frac{1}{\mu_0} \nabla \times \vec{B} - \epsilon_0 \partial_t \vec{E}. \tag{25}$$

For this model we will ignore the displacement current, which is negligible. The frequency of the alternation of the magnetic field is sufficiently low. This leads to Ampere's law:

$$\vec{j} = \frac{1}{\mu_0} \nabla \times \vec{B}. \tag{26}$$

To derive the advection diffusion equation, Ohm's law in terms of potentials (23) and Ampere's law (26) shall be equated leading to

$$\sigma(-\nabla \Phi - \partial_t A + \vec{v} \times \nabla \times \vec{A}) \quad = \quad \frac{1}{\mu_0} \nabla \times \vec{B}. \tag{27}$$

Introducing the definition of the scalar potential from above, which utilises the gauge invariance of $\vec{A}$, and taking its gradient we obtain

$$\nabla \Phi = \nabla(\vec{v} \cdot \vec{A}) - \frac{1}{\mu_0 \sigma} \nabla(\nabla \cdot \vec{A})$$

which expands to

$$\nabla(\vec{v} \cdot \vec{A}) - \frac{1}{\mu_0 \sigma}(\nabla^2 \vec{A} + \nabla \times \nabla \times \vec{A})$$

where $\nabla \times \nabla \times \vec{A} = \nabla \times \vec{B}$. Expanding the vector dot product $\nabla(\vec{v} \cdot \vec{A})$ can be done using the identity

$$\nabla(\vec{v} \cdot \vec{A}) = (\vec{v} \cdot \nabla)\vec{A} + (\vec{A} \cdot \nabla)\vec{v} + \vec{v} \times (\nabla \times \vec{A}) + \vec{A} \times (\nabla \times \vec{v}),$$

from which the zero terms shall be removed. These zero terms are $(\vec{A} \cdot \nabla)\vec{v} = 0$ and $\vec{A} \times (\nabla \times \vec{v}) = 0$ and can both be explained by to the solid body motion described above by $\vec{v} = \vec{e}_x V$.

In the case of a simple laminar flow profile with a velocity $\vec{v}_p$ which has some y-dependence such that $\vec{v}_p = \vec{e}_x V(y)$ this simplification becomes impossible as $(\vec{A} \cdot \nabla)\vec{v_p} \neq 0$. If this laminar case was considered the derivation from this point would differ significantly. It is likely that an analytic solution would no longer prove suitable and the flow inside the conductive layer would need to be solved numerically.

The gradient of the scalar potential can now be given as

$$\nabla\Phi = (\vec{v}\cdot\nabla)\vec{A} + \vec{v}\times(\nabla\times\vec{A}) - \frac{1}{\mu_0\sigma}(\nabla^2\vec{A} + \nabla\times\vec{B})$$

Substituting this into equation (27) yields

$$-(\vec{v}\cdot\nabla)\vec{A} - \vec{v}\times(\nabla\times\vec{A}) + \frac{1}{\mu_0\sigma}\nabla^2\vec{A} + \frac{1}{\mu_0\sigma}\nabla\times\vec{B} - \partial_t A + \vec{v}\times\nabla\times\vec{A} = \frac{1}{\mu_0\sigma}\nabla\times\vec{B},$$

which simply reduces to

$$\partial_t\vec{A} + (\vec{v}\cdot\vec{\nabla})\vec{A} = \frac{1}{\mu_0\sigma}\nabla^2\vec{A}, \tag{28}$$

which is the advection diffusion equation for the magnetic vector potential.

We consider that the system is invariant in the z direction. Because of this we can define the field by a single component of the vector potential $\vec{A} = \vec{e_z}A$. This is because $\vec{B}$ has only two components, which are both perpendicular to $\vec{e_z}$. This can be shown by inspecting the components of $\nabla\times\vec{A} = \vec{B}$. We can see that for $\vec{A} = \vec{e_z}A$ the field is given by $\vec{B} = [\partial_y A, -\partial_x A, 0]$. Applying this to equation (28) along side the definition $\vec{v} = \vec{e_x}V$ yields

$$\partial_t A + V\partial_x A = \frac{1}{\mu_0\sigma}\nabla^2 A, \tag{29}$$

The boundary conditions in this system are required at the interfaces S between the conducting layer and free space, which occurs at $y = \pm H$. The continuity of $\vec{B}$ across this boundary implies the continuity of the derivative of $\vec{A}$. The continuity of $\vec{A}$ follows by considering the field through a region on the surface of the interface, S, and the boundary of this region δS gives $\int_S \vec{B}dS = \oint_{\delta S}\vec{A}\cdot dl$ shrinking the region S to an infinitesimal width shows the continuity of $\vec{A}$ is required by the regularity (non-singularity) of $\vec{B}$. The continuity of $\vec{A}$ and its derivatives leads to the following

$$[A]_S = [(\vec{n}\cdot\vec{\nabla})A]_S = 0, \tag{30}$$

where $\vec{n}$ is the unit normal to the boundary, and $[f]_S$ the change in f across the surface S.

Using the half-thickness of the layer H as the length scale and $\mu_0\sigma H^2$ and time scale we introduce a couple of key dimensionless parameters. Firstly a dimensionless ac frequency

$$\bar{\omega} = \mu_0\sigma\omega H^2, \tag{31}$$

where ω is the frequency of alternation of the applied magnetic field. The dimensionless frequency is typically of order 0 for example $\bar{\omega} \sim 1$ for a flow of liquid sodium with

$\sigma = 8.3 \times 10^6\,\mathrm{S/m}$ in a layer of half width $H \sim 0.1\,\mathrm{m}$ with an ac frequency $\frac{\omega}{2\pi} \sim 60\,\mathrm{Hz}$.

Secondly the magnetic Reynolds number, which represents a dimensionless velocity and gives an estimate of the effects of the motion induced induction compared with the magnetic diffusion,

$$Rm = \mu_0 \sigma V H \tag{32}$$

Again we note that in this work a significant feature of the Magnetic Reynolds number is that it depends not only on the velocity by also on the conductivity of the medium.

Using these dimensionless parameters equation (29) can be presented in a dimensionless form

$$\partial_t A + Rm \partial_x A = \nabla^2 A.$$

4.1.1 Solution for Standing Magnetic Wave

This derivation will be used for two definitions of the magnetic field, firstly we will consider a field produced by a standing wave, which alternates harmonically. Following this a field generated by a couple straight wires is presented. Schematic plots which show both of these two field definitions are given in figure 4.

We define the applied field for the first case, the harmonic standing wave, with vector potential amplitude

$$\vec{e}_z A_0(\vec{r}, t) = \vec{e}_z \hat{A}_0(y) \cos(kx) \cos(\omega t),$$

where k is the wavenumber, or spatial frequency, in the x direction. Outside of the conductive layer, where $\sigma = 0$, equation (29) for the vector potential reduces to

$$\frac{d^2 \hat{A}_0}{dy^2} - k^2 \hat{A}_0 = 0, \tag{33}$$

which has the solution

$$\hat{A}_0(y; k) = C_0 e^{|k|(y-1)},$$

which will tend to infinity as y tends to infinity. This is will occur outside of our domain of interest and is a consequence of the defininition of the standing harmonic field with no defined source. where the constant C_0 is given by

$$C_0 = \hat{A}_0(1; k),$$

which specifies the amplitude of the Fourier mode with wavenumber k of the external magnetic field at the upper interface between the conductive medium and free space. The external magnetic field refers to the field in the absense of the conductinve layer, and can be generated by setting $\sigma = 0$ within the layer.

The external magnetic field in the form of a standing wave, can be represented by a superposition of two oppositely travelling waves

$$A_0(\vec{r},t) = \frac{1}{2}\left(A_0^+(\vec{r},t) + A_0^-(\vec{r},t)\right),$$

where $A_0^{\pm}(\vec{r},t) = \hat{A}_0(y)\cos(\omega t \pm kx)$. We can now look for a solution in the matching form

$$A(\vec{r},t) = \frac{1}{2}\left(A^+(\vec{r},t) + A^-(\vec{r},t)\right),$$

where $A^{\pm}(\vec{r},t) = \Re\left(\hat{A}(y;\pm k)e^{i(\omega t \pm kx)}\right)$ are oppositely travelling waves.

We shall now use equation (28) to generate an equation for the field within the conductive medium. The equation will now by applied in spectral space allowing the derivatives to be more simply expressed. Recognising that $(\vec{v}\cdot\nabla)\hat{A} = V\partial_x\hat{A}$ as $\vec{v}$ has only an x component yields

$$\mu_0\sigma\partial_t A + \mu_0\sigma V\partial_x A = \partial_x^2 A + \partial_y^2 A.$$

Evaluating the derivatives in spectral space gives

$$\mu_0\sigma i\omega\hat{A} + \mu_0\sigma Vik\hat{A} = -k^2\hat{A} + \frac{d^2}{dy^2}\hat{A}$$

and substituting in the definitions for $\bar{\omega}$ and Rm yields

$$\frac{d^2}{dy^2}\hat{A} - (k^2 + i\bar{\omega} + kRm)\hat{A} = 0$$

Within the conductive medium, the equation for a travelling field can now be given as

$$d^2\hat{A}/dy^2 - \kappa^2\hat{A} = 0, \tag{34}$$

where

$$\kappa(k) = \sqrt{k^2 + i(\bar{\omega} + kRm)}. \tag{35}$$

The general solution to equation (34) which is present in the layer can be written as

$$\hat{A}(y;k) = C_2\sinh(\kappa y) + D_2\cosh(\kappa y). \tag{36}$$

Above the layer the solution is given by

$$\hat{A}(y;k) = \hat{A}_0(y;k) + \hat{A}_1(y;k), \tag{37}$$

where $\hat{A}_0(y;k) = C_0e^{|k|(y-1)}$ and $\hat{A}_1(y;k) = C_1e^{-|k|(y-1)}$represent the applied and induced fields, respectively.

Below the layer the solution decaying as $y \to -\infty$ is given by

$$\hat{A}(y;k) = C_3 e^{|k|(y-1)} \tag{38}$$

At this point we have and four unknown constants C_1, C_2, C_3, D_2 which require four equations to be determined. The boundary conditions for the continuity of A and its derivative normal to the boundary across the two interfaces between the layer and free space provide the information to solve the system. At the interface above the layer, $y = 1$, the continuity of $\hat{A}$ is given by

$$C_2 \sinh(\kappa) + D_2 \cosh(\kappa) = C_0 + C_1 \tag{39}$$

and below the layer , at $y = 1$ the condition is

$$D_2 \cosh(\kappa) - C_2 \sinh(\kappa) = C_3 \tag{40}$$

The continuity of the derivative normal to the boundary below the layer, $y = -1$, gives

$$\kappa C_2 \cosh(\kappa y) - \kappa D \sinh(\kappa y) = |k| C_3 \tag{41}$$

substituting in the solution for C_3 below the layer (40) gives

$$C_2(|k| \sinh(\kappa) + \kappa \cosh(\kappa y)) = D_2(|k| \cosh(\kappa) + \kappa \sinh(\kappa y))$$

and with the solution taken from above the layer (39) at $y = 1$,

$$\kappa C_2 \cosh(\kappa) + \kappa D_2 \sinh(\kappa) = |k| C_0 - |k| C_1$$

substituting in the solution for C_1 taken from (39) gives

$$C_2(|k| \sinh(\kappa) + \kappa \cosh(\kappa y)) + D_2(|k| \cosh(\kappa) + \kappa \sinh(\kappa y)) = 2|k| C_0$$

and as we already have $C_2(|k| \sinh(\kappa) + \kappa \cosh(\kappa y)) = D_2(|k| \cosh(\kappa) + \kappa \sinh(\kappa y))$ from above we can state

$$C_2(|k| \sinh(\kappa) + \kappa \cosh(\kappa y)) = D_2(|k| \cosh(\kappa) + \kappa \sinh(\kappa y)) = |k| C_0.$$

The four unknown constants are found as

$$C_2 = C_0|k|/(|k|\sinh(\kappa) + \kappa\cosh(\kappa)) \quad (42)$$

$$D_2 = C_0|k|/(|k|\cosh(\kappa) + \kappa\sinh(\kappa)) \quad (43)$$

$$C_1 = D_2\cosh(\kappa) + C_2\sinh(\kappa) - C_0 \quad (44)$$

$$C_3 = D_2\cosh(\kappa) - C_2\sinh(\kappa). \quad (45)$$

4.1.2 Solution for The Pair of Straight Wires

The derivation above will now be used for a field generated by a couple of straight wires with oppositely flowing currents, as shown in figure 4(b). The physical interpretation of these wires could be that they represent two sides of a single coil or that they are sections of two separate wide coils, where the coils are wide enough for the returning loop to be negligible to the system in the proximity of the original wires. These two straight wires carry ac currents of amplitude I_0 in opposite directions. These wires are orientated along the z-axis and are located at a height of h above the centre line of the layer and at distances $\pm s$ from the y-axis.

The free-space distribution of the vector potential amplitude which as before will consist only of the z-component, is governed by

$$\nabla^2 A_0 = -\delta(\vec{r} - h\vec{e_y} - s\vec{e_x}) + \delta(\vec{r} - h\vec{e_y} + s\vec{e_x}) \quad (46)$$

which is scaled by $\mu_0 I_0$, $\delta(r)$ is the Dirac delta function and $\vec{r}$ is the radius vector. . The Dirac delta function is used to model the point currents which represent the two wires. The equation for the free space distribution is reduced by the Fourier transform $\hat{A}(y;k) = \int_{-\infty}^{\infty} A(x,y)e^{ikx}dx$, which converts equation (46) into

$$\frac{d^2\hat{A}_0}{dy^2} - k^2\hat{A}_0 = \delta(y-h)\int_{-\infty}^{\infty}[\delta(x+s)]e^{ikx}dx - \delta(y-h)\int_{-\infty}^{\infty}[\delta(x-s)]e^{ikx}dx$$

Collecting the integrals into the coefficient $f(k) = \int_{-\infty}^{\infty}[\delta(x-s) - \delta(x+s)]e^{ikx}dx$ yields

$$\frac{d^2\hat{A}_0}{dy^2} - k^2\hat{A}_0 = -f(k)\delta(y-h), \quad (47)$$

$$f(k) = e^{iks} - e^{-iks} = 2isin(ks). \quad (48)$$

The solution of equation (47) decaying at $y \to \pm\infty$ can be written as

$$\hat{A}_0(y;k) = c(k)e^{-|k(y-h)|}. \quad (49)$$

Integrating equation (47) over the singularity at $y = h$,

$$\lim_{\epsilon \to 0} \int_{h-\epsilon}^{h+\epsilon} [\frac{d^2 \hat{A}_0}{dy^2} - k^2 \hat{A}_0] \delta y = \lim_{\epsilon \to 0} \int_{h-\epsilon}^{h+\epsilon} [-f(k)\delta(y-h)] \delta y$$

which evaluates to

$$\left[\frac{d}{dy}\hat{A}_0\right]_{y=h} - \left[k^2 y \hat{A}_0\right]_{y=h} = -f(k),$$

we obtain the boundary condition

$$\left[\frac{d}{dy}\hat{A}(y;k)\right]_{y=h} = -f(k).$$

Applying the boundary condition shows the remaining coefficient can be expressed as

$$c(k) = \frac{f(k)}{2|k|} = \frac{i \sin(ks)}{|k|}. \tag{50}$$

Solutions for the kth Fourier mode of the magnetic vector potential in the three regions located inside, above and below the layer have been derived above and are given by equations (36, 37, 38) respectively. The coefficients for these three equations follow from the derivation above are given by equations (42-45). The constant C_0 is again given by $\hat{A}_0(1;k)$ and is calculated by equation (49) with $c(k)$ given by equation (50):

$$C_0 = \frac{i \sin(ks)}{|k|} e^{-(1-h)}.$$

Finally, the complex vector potential $\vec{A}$ is recovered by the inverse Fourier transform of $\hat{A}$ given by

$$\vec{A}(x,y) = \frac{1}{2\pi} \int_{-\infty}^{\infty} \hat{A}(y;k) e^{-ikx} dk, \tag{51}$$

which can be efficiently calculated with the fast Fourier transform.

4.2 Results

This section presents the main results obtained using model introduced above for a single harmonic of the applied field and then for a field generated by a couple of straight wires. It is important to note that in this model, where the vector potential has only one component, the difference in the vector potential between two points defines the linear flux density of the magnetic field between two lines parallel to the vector potential at these two points. This can be shown by Stoke's theorem (11), which in this context means, the circulation of the vector potential around a thin coil gives the magnetic flux through that surface the coil bounds. This also holds true for the derivative of the

vector potential and linear flux density. This leads to the difference in amplitude of the vector potential between two points being proportional to the emf amplitude measured by simple coil, which would be represented by two straight wires oriented along the z-axis. Assuming the second wire to be sufficiently far from the magnetic field the vector potential amplitude of a single point would represent the emf measured by a wide coil which is only partially in the region of interest.

4.2.1 Results for A Single Harmonic

Before introducing the modifications to the measurement scheme for the phase shift flowmeter, we will introduce the models behaviours as a basic for further development. In this section a single harmonic of the magnetic field will be considered. This corresponds to a field generated by a standing wave with wave number k. The phase distribution and the flux lines, both in phase with the applied field and shifted by $\pi/2$, are shown in figure 6. An important observation is that, although the field decays exponentially, the phase distribution below the layer is invariant in the $y-$direction. Although this is only generally true for a field generated by a standing harmonic wave it leads to one of the major advantages of the phase shift flowmeter, that the measurements of phase are robust to variation of the vertical position of the measurement coils. The phase is defined as the angle of the complex field, when presented in polar form. It is calulated as the arctangent of the ratio between the field in phase and out of phase with the applied field, $\varphi = \arctan(\frac{\Re(A)}{\Im(A)})$.

An example of the measurement scheme, presented in [31], prior to introducing any rescaling is given in figure 7. It can be seen that for a given dimensionless frequency, which depends on conductivity, the phase difference can be used as a measure of magnetic Reynolds number, which when knowing the conductivity can equate to measuring the velocity.

The phase distribution between two nodes of the applied magnetic measured below the conducting medium is shown in figure 7(b). While at rest this phase distribution is piecewise constant varying only by jumps in the phase of π. These jumps in phase occur at the wave nodes, which are located at $x = \pm 0.5\pi$. Figure 7(b) shows that the discontinuities in the phase are smoothed out when the conducting medium is in motion. The smoothed discontinuities are shifted further downstream with increasing values of Rm. Another significant feature of this phase variation, which can also be seen in figure 7(b), is that the strongest phase variation occurs downstream of a node, whereas the variation upstream of a node is relatively weak, this disparity is more pronounced at lower values of Rm. This shows the importance of placing the downstream measurement coil close to the node if low velocities are to be measured, as the sensitivity of to the velocity is higher in these locations. This is also relevant to the rescalings which are discussed

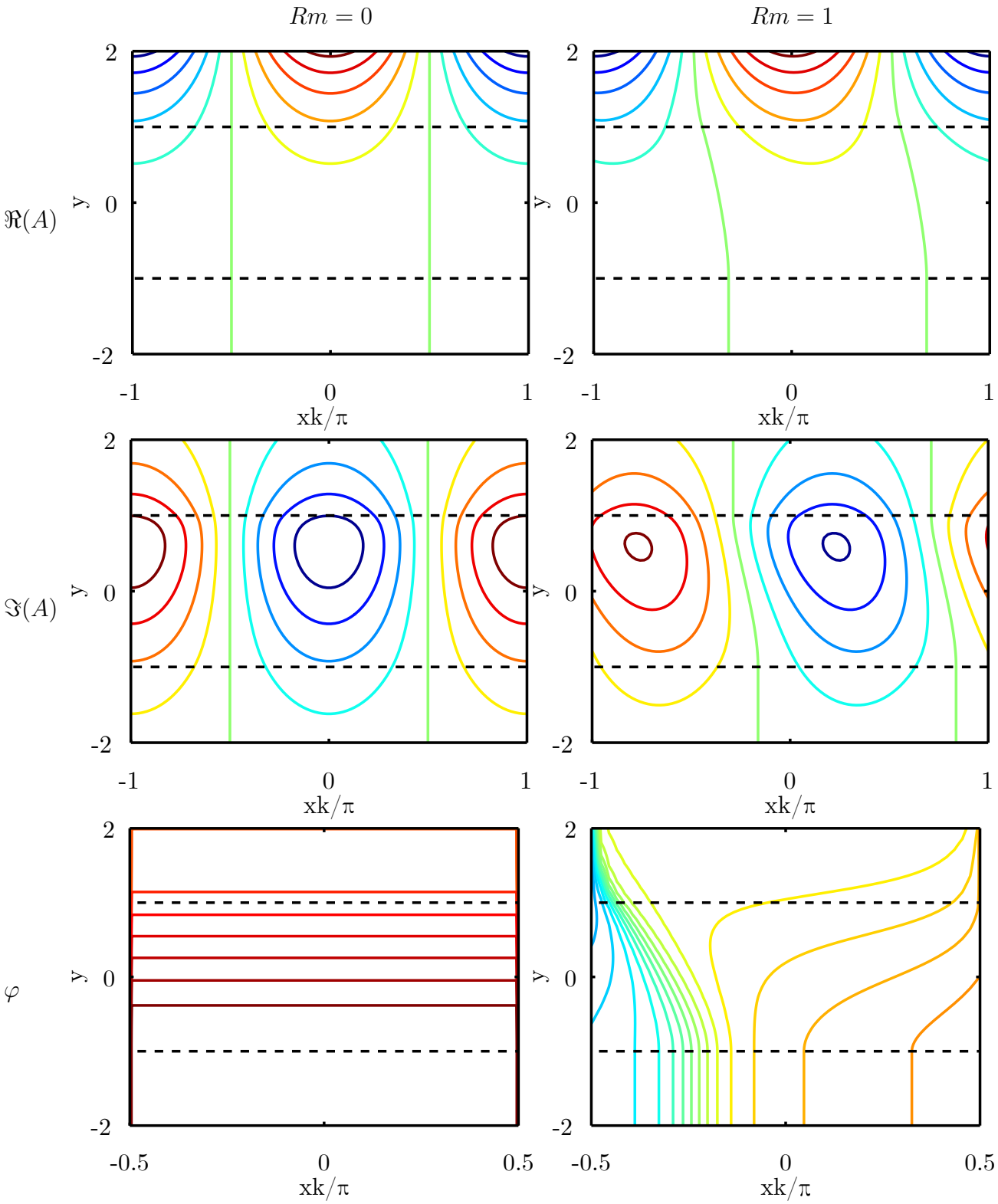

Figure 6: Magnetic flux lines generated by a standing harmonic wave, in phase (top) and out of phase (middle) with the applied field, and the phase distribution (bottom) at rest (left) with $Rm = 1$(right), with $\bar{\omega} = 1$ and $k = 1$

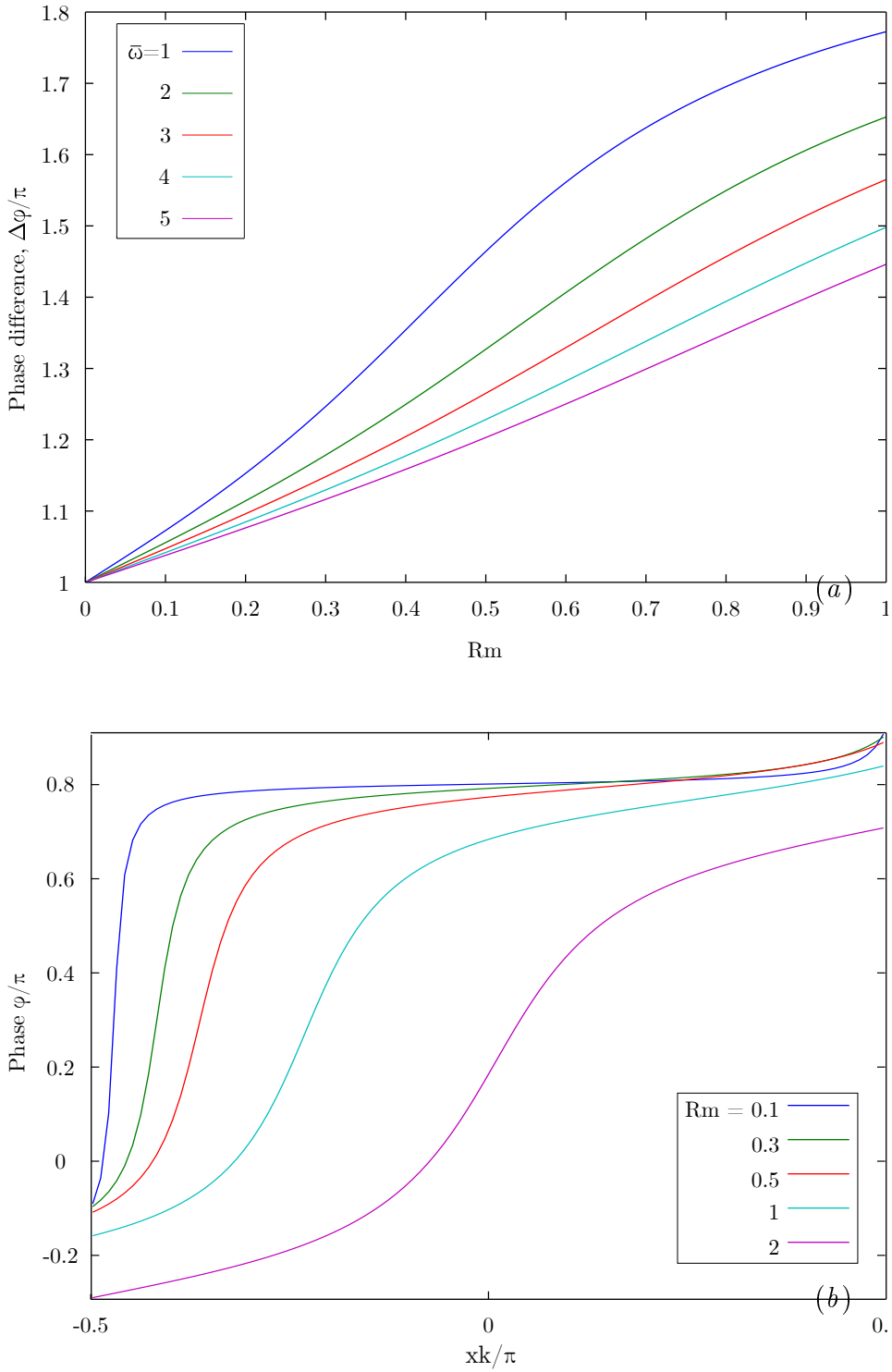

Figure 7: Phase difference versus magnetic Reynolds number taken between symmetric measurement points located at $x = \pm 0.5$ for various dimensionless frequencies (a). Phase distribution over a half-wavelength of the applied magnetic field(b) at various dimensionless velocities defined by Rm.

later. The significance of the measurements upstream of a node being significantly less affected by the motion of the flow will become apparent when introducing the rescalings.

The variation of phase φ with Rm at low velocities is characterized by the phase sensitivity.

$$K = \frac{1}{\pi} \left. \frac{\partial \varphi}{\partial Rm} \right|_{Rm=0}. \tag{52}$$

The dependence of this quantity on the dimensionless frequency $\bar{\omega}$ is plotted in figure 8 for several observation points and wave numbers.

By observing that φ varies nearly linearly with $\bar{\omega}$, as given in equation (35), we can see the variation of K with $\bar{\omega}$ can be reduced. As $\bar{\omega}$ has a similar effect to Rm the reduction can be achieved by scaling the phase variation with the phase itself, which leads to the relative phase sensitivity.

$$K_r = \pi \frac{K}{\varphi} = \left. \frac{\partial \ln \varphi}{\partial Rm} \right|_{Rm=0}. \tag{53}$$

As seen in figure 8(c,d), the relative phase sensitivity tends to constant for given observation point. Although the relative phase sensitivity is not completely independent of $\bar{\omega}$ it can be seen that at higher values of $\bar{\omega}$ it varies much less than the unscaled phase sensitivity shown in 8(a,b) especially at lower wave numbers. Following this idea the effect of conductivity can be reduced by scaling the phase shift with a reference phase. The reference phase φ_ω is taken as the phase shift between the sending and the upstream receiving coils, as the phase shift upstream of a node is less affected by the motion of the layer. At low $\bar{\omega}$ the reference phase varies directly with $\bar{\omega}$ which, similar to Rm, is proportional to conductivity.The following scaling by the square of the reference phase, φ_ω, will reduce variation with conductivity

$$\Delta_2 \varphi = \frac{\Delta_0 \varphi}{\varphi_\omega^2}, \tag{54}$$

where $\Delta_0 \varphi = \varphi_+ - \varphi_-$is the difference between the downstream and upstream phases which are denoted by φ_+ and φ_- respectively.

For the rescaled phase shift to be insensitive to σ it can not be dependent directly on $\bar{\omega}$ or Rm, but must be a function of these control parameters such that σ is eliminated. Instead we choose $\frac{Rm}{\bar{\omega}} = \frac{V}{\omega H}$ to measure against, which represents a dimensionless velocity, this ratio shall be referred to as the relative velocity.

Figure 9 shows the rescaled phase shift given by equation (54) has a weak dependence on $\bar{\omega}$ as long as $\bar{\omega}$ is low. For sufficiently low relative velocities the variation of the rescaled phase shift with $\bar{\omega}$ is weak up to $\bar{\omega} \sim 1$. This range of low relative velocities depends on the locations of the observation points. With points closer to the nodes, located $x = \pm 0.5\pi$, the range of relative velocities, where the rescaled phase difference

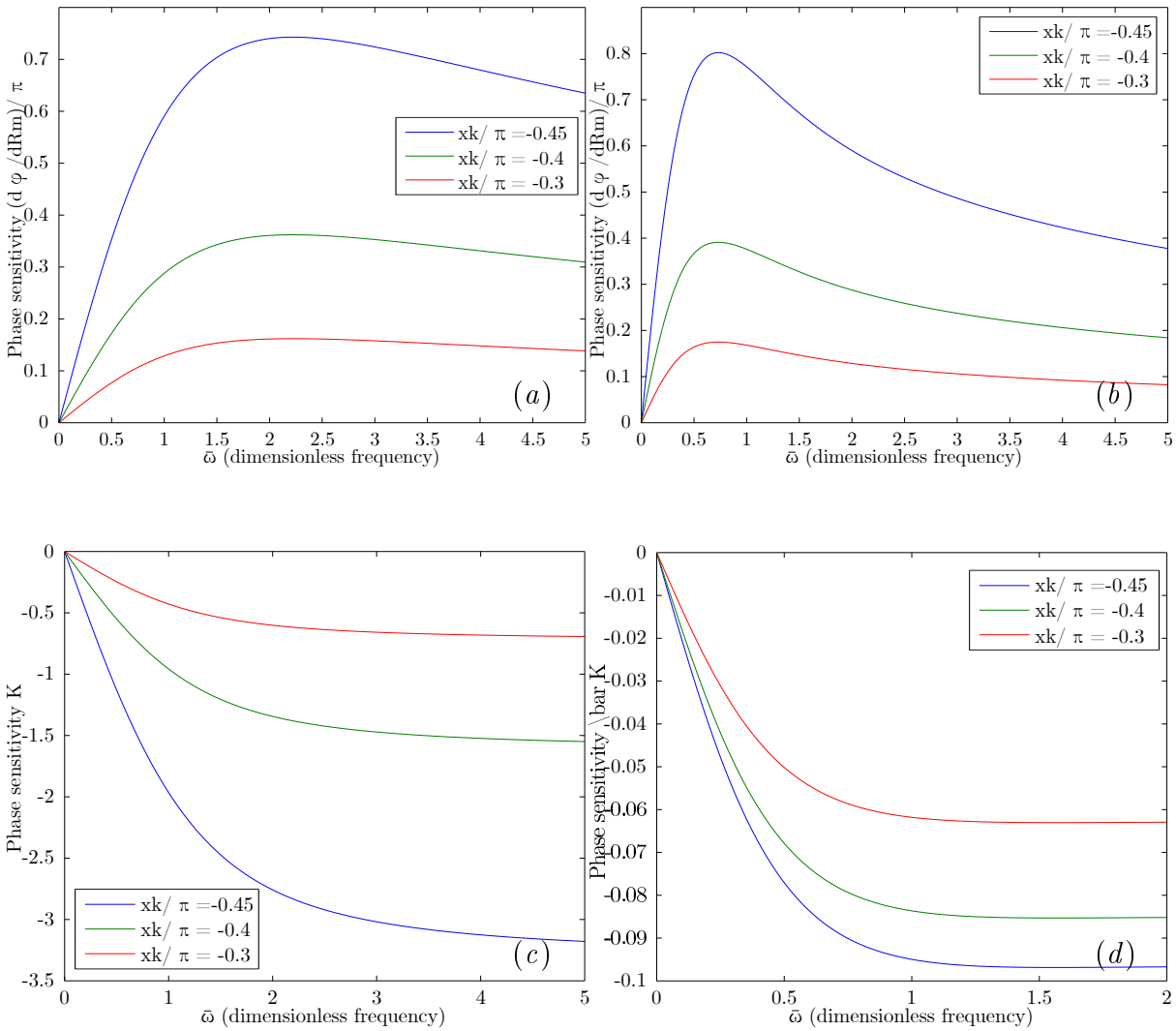

Figure 8: The phase sensitivity (*a*,b) and the relative phase sensitivity (c,d) versus the dimensionless frequency $\bar{\omega}$ at various horizontal observation positions below the layer for $k = 1$ (a,c) and $k = 0.5$ (b,d)

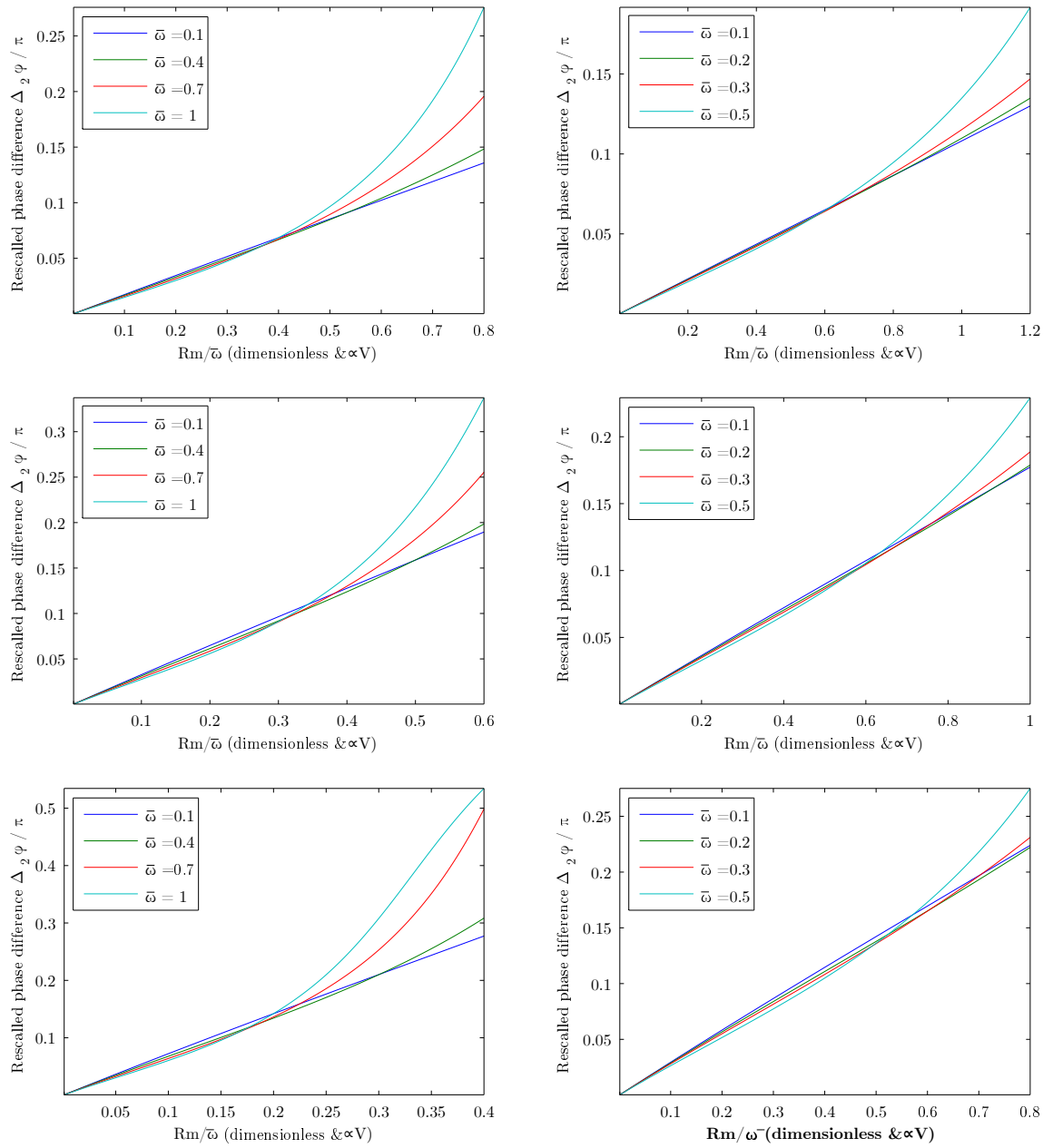

Figure 9: Rescaled phase shift $\Delta_2\varphi$ between two observation points placed below the layer at $\pm x = 0.2\pi$ (top), 0.3π (middle) and 0.4π (bottom) versus the relative velocity $Rm/\bar{\omega}$ for various dimensionless frequencies with $k = 1$ (left) and $k = 0.75$ (right)

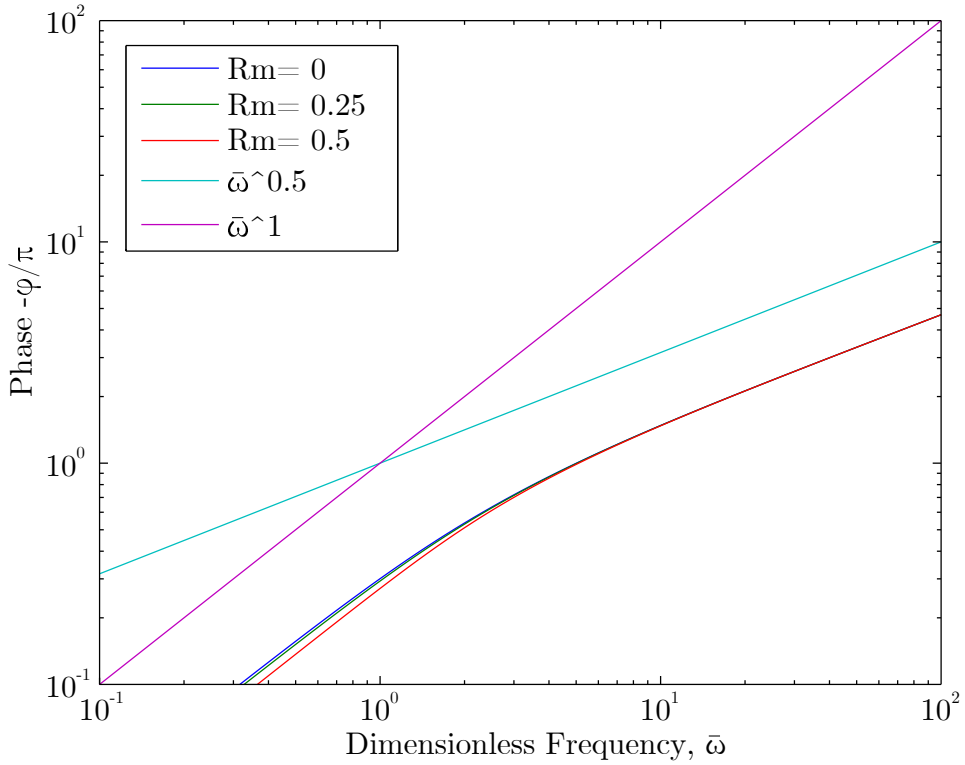

Figure 10: Phase versus the dimensionless frequency, $\bar{\omega}$ at the bottom of the layer for various wavenumbers and $Rm = 0.1$

remains invariant with $\bar{\omega}$ is reduced. Figure 9 shows that far enough from the nodes the relationship between rescaled phase difference and relative velocity is invariant for a range of dimensionless frequency from 0.1 to 1, which corresponds to a change of an order of magnitude to the conductivity. This range is supported by looking at the nature of the change of phase with dimensionless frequency, as shown in figure 10, where there is a linear relationship for low dimensionless frequencies which continues until $\bar{\omega} \approx 1$.

The scaling given by equation (54) fails at higher values of $\bar{\omega}$ where the shielding effect causes the reference phase to vary non-linearly. In this case, the phase shift is $O(1)$ over the skin layer with the characteristic thickness $\sim \bar{\omega}^{-1/2}$. It means that the total phase shift due to the diffusion of magnetic field through the whole conducting layer with thickness $O(1)$ varies as $\varphi \sim \bar{\omega}^{1/2} \sim \sigma^{1/2}$. Since the external magnetic field in the form of a standing wave consists of two oppositely travelling waves, the motion of the layer is equivalent to the variation of the dimensionless frequency by $\sim Rm \ll 1$. The respective phase shift between two receiving coils can be estimated as

$$\Delta_0 \varphi \sim \frac{\partial \varphi}{\partial \bar{\omega}} Rm \sim \bar{\omega}^{-1/2} Rm \sim \sigma^{1/2}.$$

This implies that for higher frequencies $\bar{\omega} \gtrsim 1$, rescaling directly with the reference phase shift should lead to the conductivity being eliminated from the measurement scheme. The rescaled phase shift which is rescaled directly with the reference phase shall be denoted

as $\Delta_1\varphi$ and is defined as

$$\Delta_1\varphi = \frac{\Delta_0\varphi}{\varphi_-}. \tag{55}$$

The rescaled phase shift $\Delta_1\varphi$ is plotted in figure 11 against the relative velocity for two different wavenumbers $k = 1$ and and $k = 0.5$ and various dimensionless frequencies. For $k = 1$ the dependence of the rescaled phase shift on $\bar{\omega}$ appears to be greatly reduced for $\bar{\omega} > 1$. For $k = 0.5$, which corresponds a wavelength of the applied magnetic field significantly larger than the thickness of the layer, the variation of $\Delta_1\varphi$ with $\bar{\omega}$ is practically insignificant starting from $\bar{\omega} = 1$. This implies that the measurement scheme is no longer strongly dependant on the conductivity of the flow.

4.2.2 External Magnetic Field Generated By A Couple Of Wires

In this section we consider the case of an external magnetic field generated by a couple of straight wires as shown in figure 4(b). For the layer at rest, the magnetic field distribution is mirror-symmetric with respect to the $x = 0$ plane. This is analogous to a node in the mono-harmonic standing wave considered in the previous section. Correspondingly, when the layer is at rest, there is a phase jump of π at $x = 0$. In contrast to the previous case, the phase is no longer constant on both sides of the discontinuity and varies horizontally as well as vertically.

The relationship between the phase and frequency for the two wire model is plotted in figure 13 as with the field generated by a standing wave the variation is linear for low frequencies and for higher frequencies, where shielding disrupts this linearity and the phase varies with the root of the dimensionless frequency, $\varphi \propto \bar{\omega}^{\frac{1}{2}}$. The approximate dimensionless frequency for which the linear behaviour fails is similar between the two exciting fields, and in both cases the variation of the phase with the root of the frequency is well established by $\bar{\omega} = 1$.

The phase sensitivity is plotted against dimensionless frequency for various measurement points below the layer in figure 14. It shows that the phase sensitivity attains a maximum at an optimal frequency, $\bar{\omega} \approx 0.14$. The low optimal frequency can also be shown from equation 50 which shows the applied magnetic field is dominated by low wavenumber modes. Another important feature of the phase sensitivity is that its reduction above the optimal frequency is gradual compared with to its steep increase at sub-optimal frequencies. The loss of the sensitivity from working with a much larger simplified value of $\bar{\omega} = 1$ is relatively small. This loss becomes smaller still with observation points further from the origin.

Figures 14(a,b) and 13 all show that the range of $\bar{\omega}$ where the phase sensitivity varies linearly is rather short. Therefore there is a limited range for which in the two wire model rescaling (54) may be applicable. Figure 15(a-c) show the rescaling with the square of the reference phase applied to the two-wire model. It can be seen that the rescaling fails

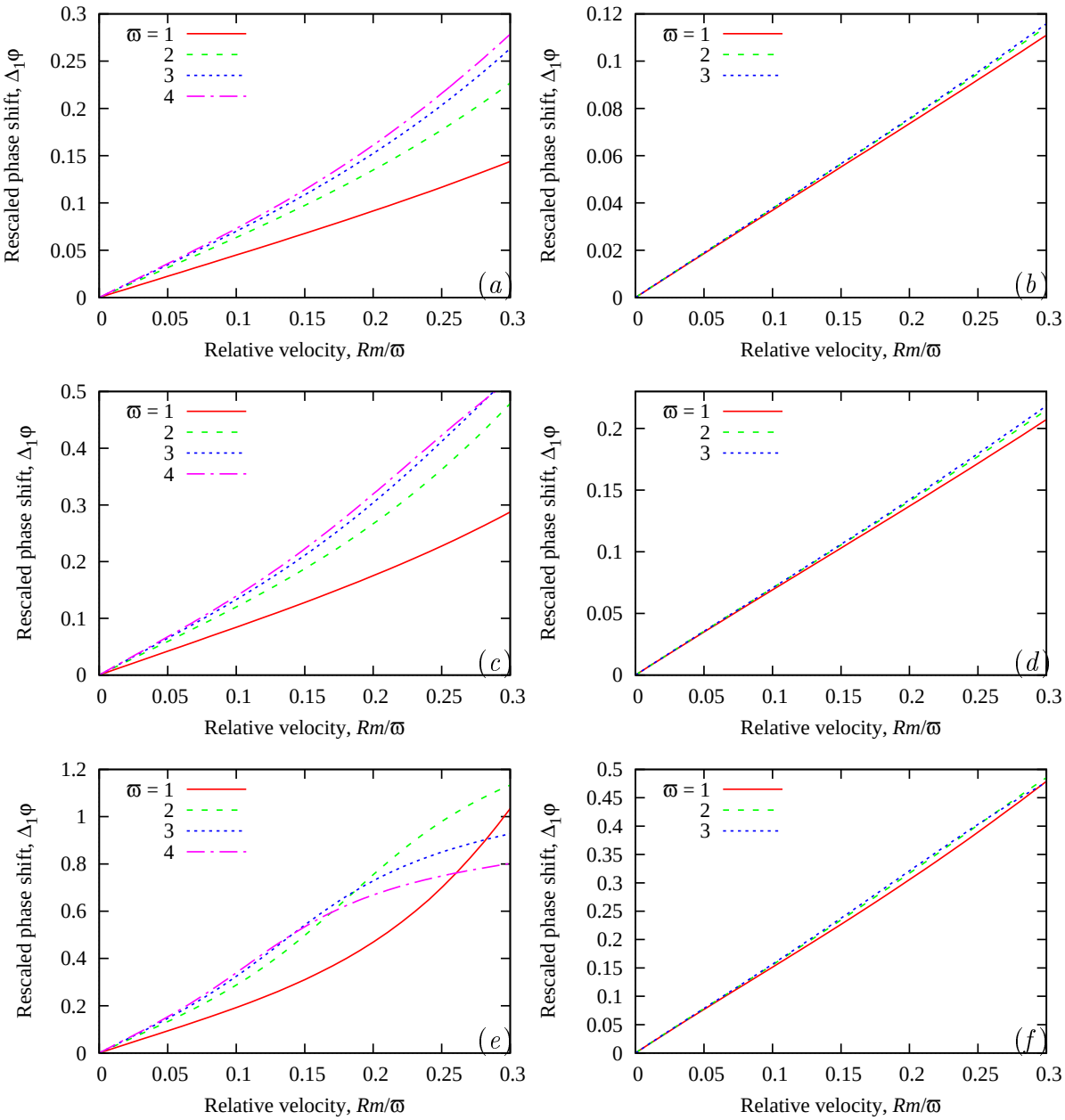

Figure 11: Rescaled phase shift $\Delta_1\varphi$ between two observation points placed below the layer at $\pm xk/\pi = 0.2$ (a,b), 0.3 (c,d) and 0.4 (e,f) versus the relative velocity $Rm/\bar{\omega}$ for $k = 1$ (a,c,e) and $k = 0.5$ (b,d,f) at various dimensionless frequencies $\bar{\omega} \gtrsim 1$.

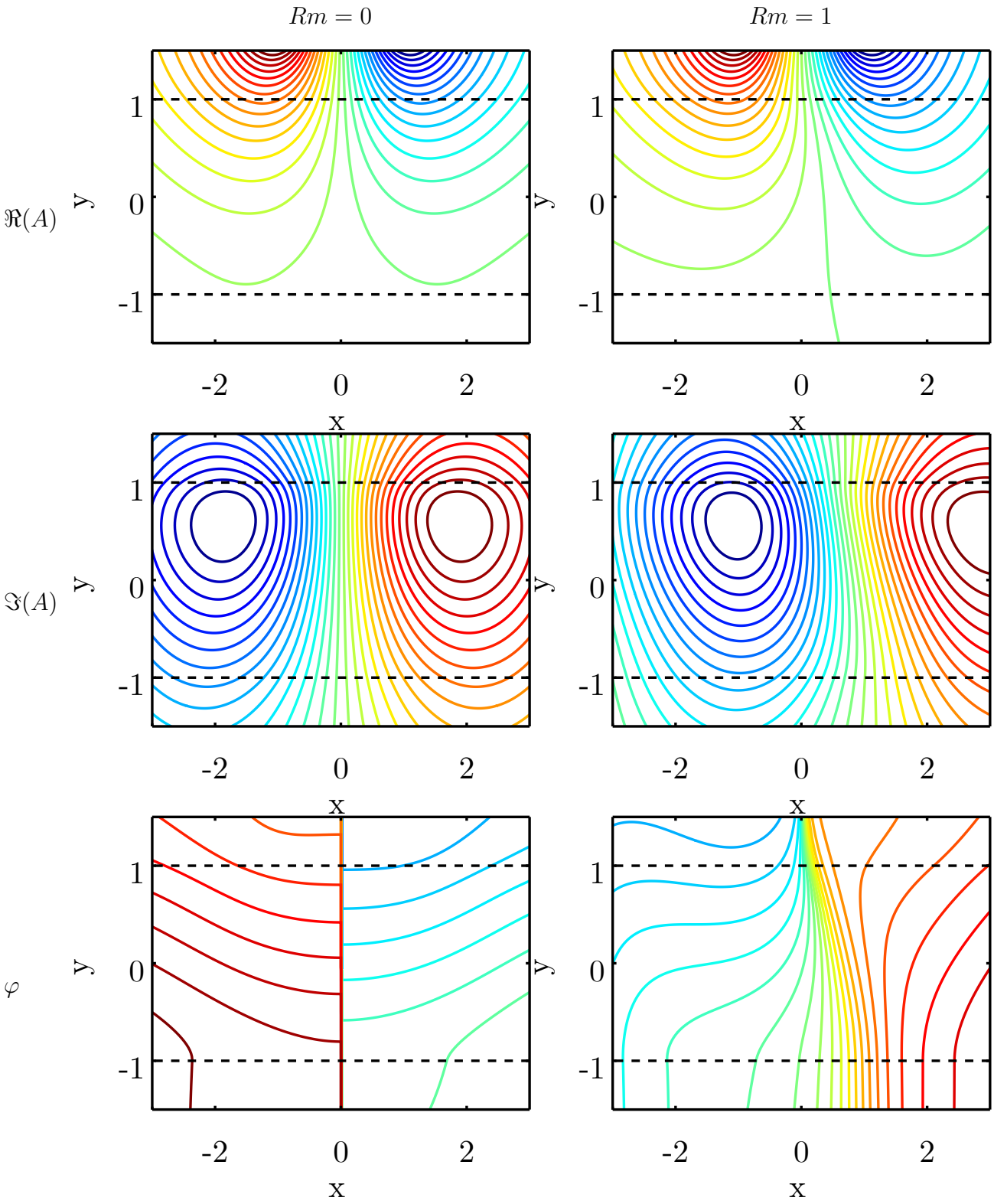

Figure 12: Magnetic flux lines generated by a couple of wires, in phase (top) and out of phase (middle) with the applied field, and the phase distribution (bottom) at rest (left) with $Rm = 1$(right), with $\bar{\omega} = 1$,$h = 1$and $s = 1$

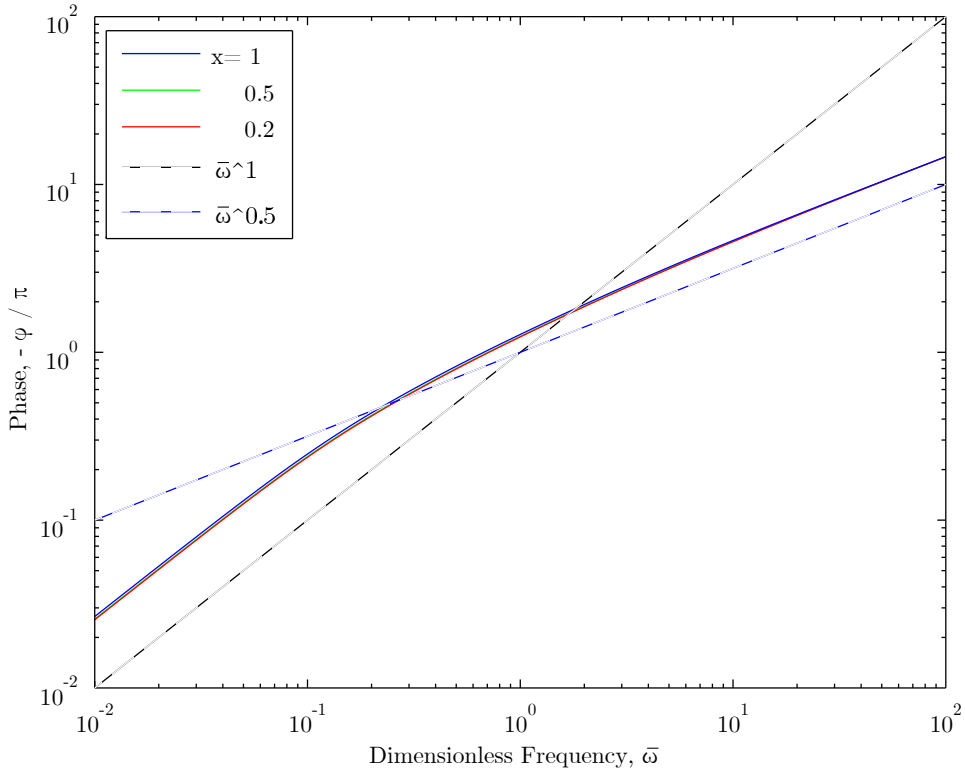

Figure 13: Phase verses frequency, $\bar{\omega}$ at the bottom of the layer for various Rm values

for the range of frequencies for which it is designed. It is likely that this rescaling fails at this range of frequencies because the transition between the linear and square root relationships of phase and frequency, shown in figure 13, occurs at a lower frequency in this model compared with the simple model for a harmonic standing wave. Figure 15(d) shows that this rescaling does indeed theoretically function very well with little change to the measurement for a change of two orders of magnitude of the frequency. This rescaling only works for a low enough range of frequencies and these frequencies are impractically low.

At dimensionless frequencies near unity $\bar{\omega} \sim 1$, which presents the main interest from a practical point of view, the rescaling presented to handle the the non-linear variation of the phase-shift, given by equation (55), is expected to be suitable. This rescaled phase shift is plotted in figure 16 against the relative velocity for several locations of the observation points and various dimensionless frequencies. It can be seen that the rescaled phase shift $\Delta_1\varphi$ depends predominantly on the relative velocity while its variation with $\bar{\omega}$ is relatively weak. In figure 16(d) the exception to this is shown which occurs for the large separations of the observation points, in this case $x = \pm 2.5$, where the lines for the different dimensionless conductivities do not collapse well. This deterioration of the rescaling at larger separations of observation points may be due to the horizontal variation of the reference phase mentioned above, which was not present in the model with the simple harmonic applied field.

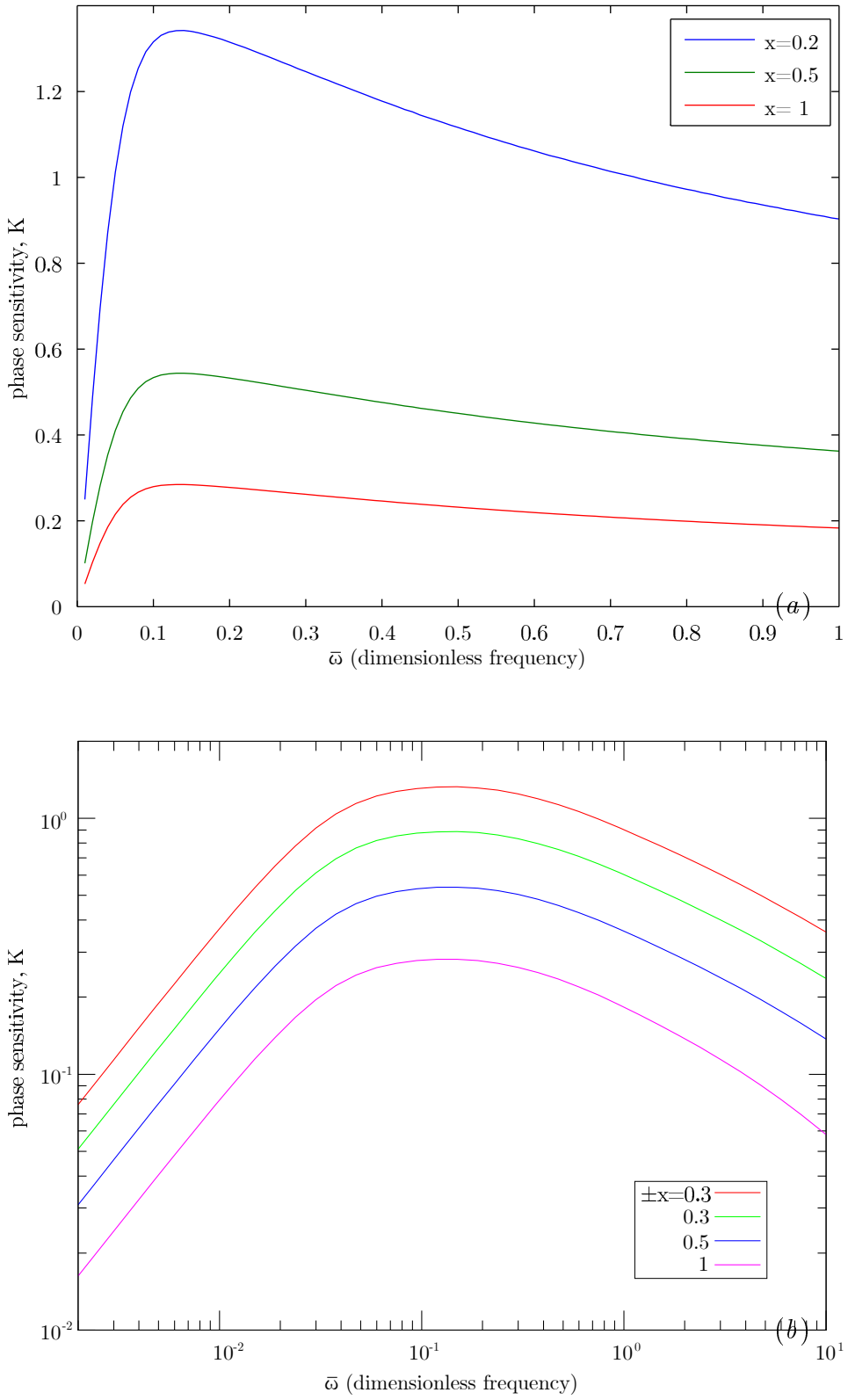

Figure 14: Phase sensitivity K given by equation (52) versus the dimensionless frequency $\bar{\omega}$ at various observation points at the bottom of the layer (a) and the same plotted on log-log axis (b) .

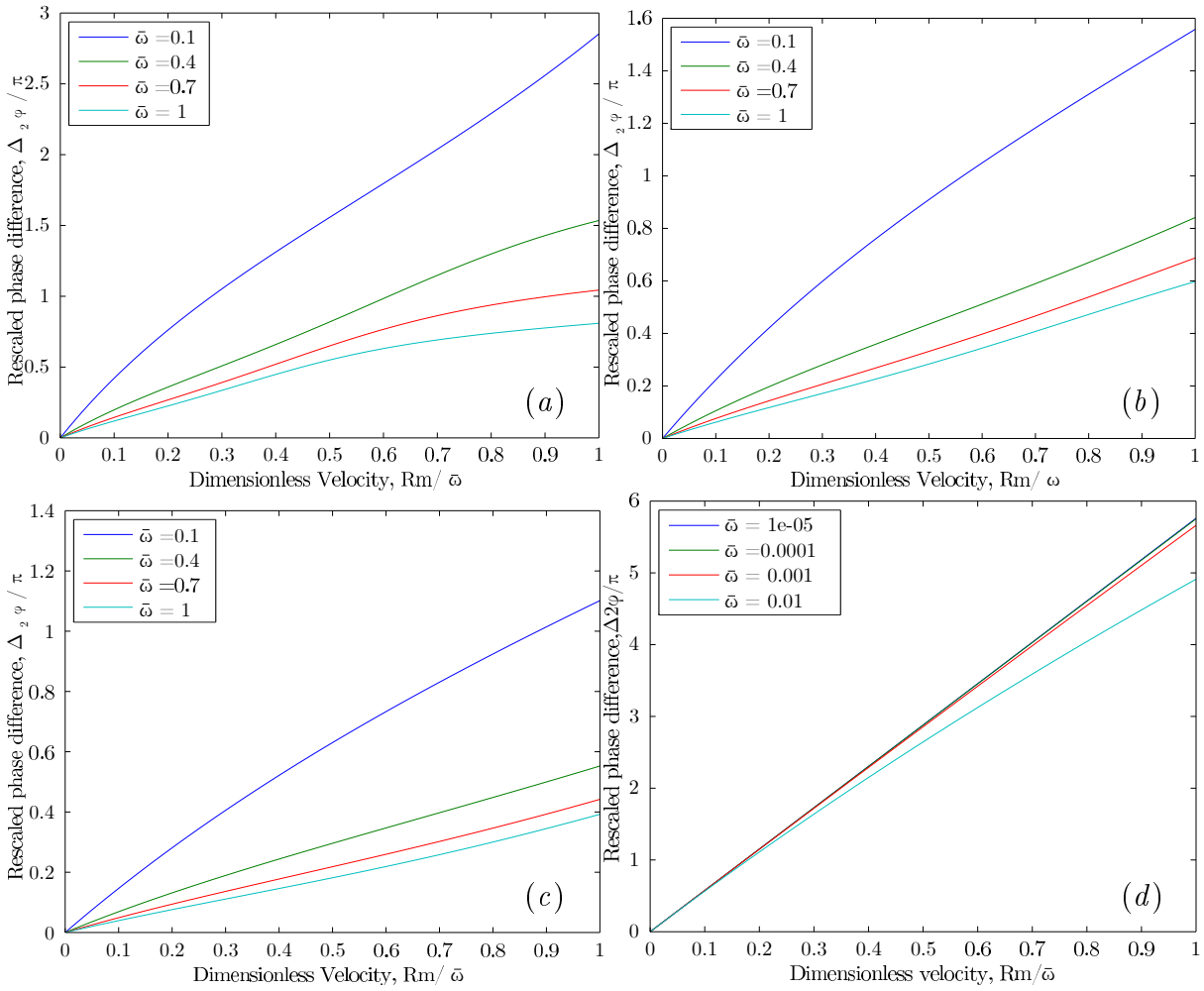

Figure 15: The rescaled phase shift $\Delta_2\varphi$ between two observation points placed below the layer at $\pm x = 0.5$ (a,d), 1 (b), 1.5 (c), versus the relative velocity $Rm/\bar{\omega}$ at various dimensionless frequencies $\bar{\omega}$. Note that in (d) the range of frequencies presented are significantly lower.

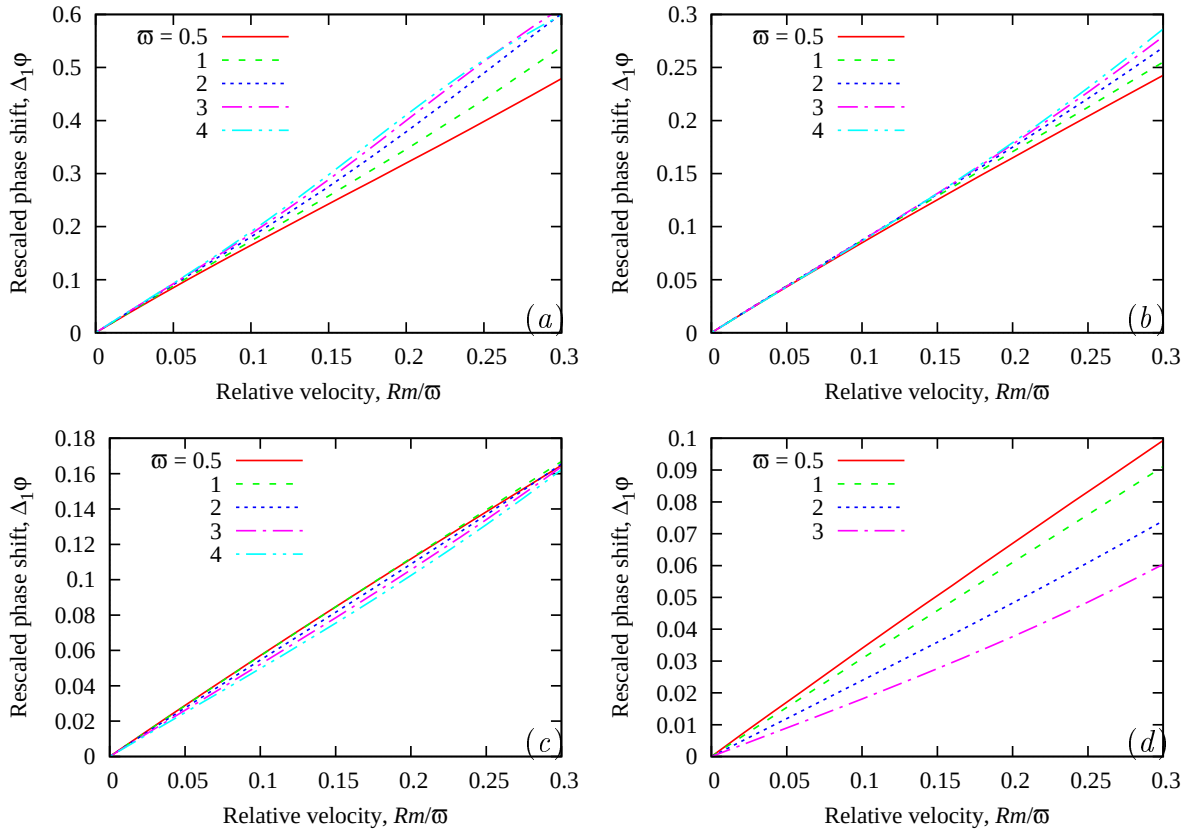

Figure 16: The rescaled phase shift $\Delta_1\varphi$ between two observation points placed below the layer at $\pm x = 0.5$ (a), 1 (b), 1.5 (c), and 2.5 (d) versus the relative velocity $Rm/\bar{\omega}$ at various dimensionless frequencies $\bar{\omega}$.

4.2.3 Optimising Layout

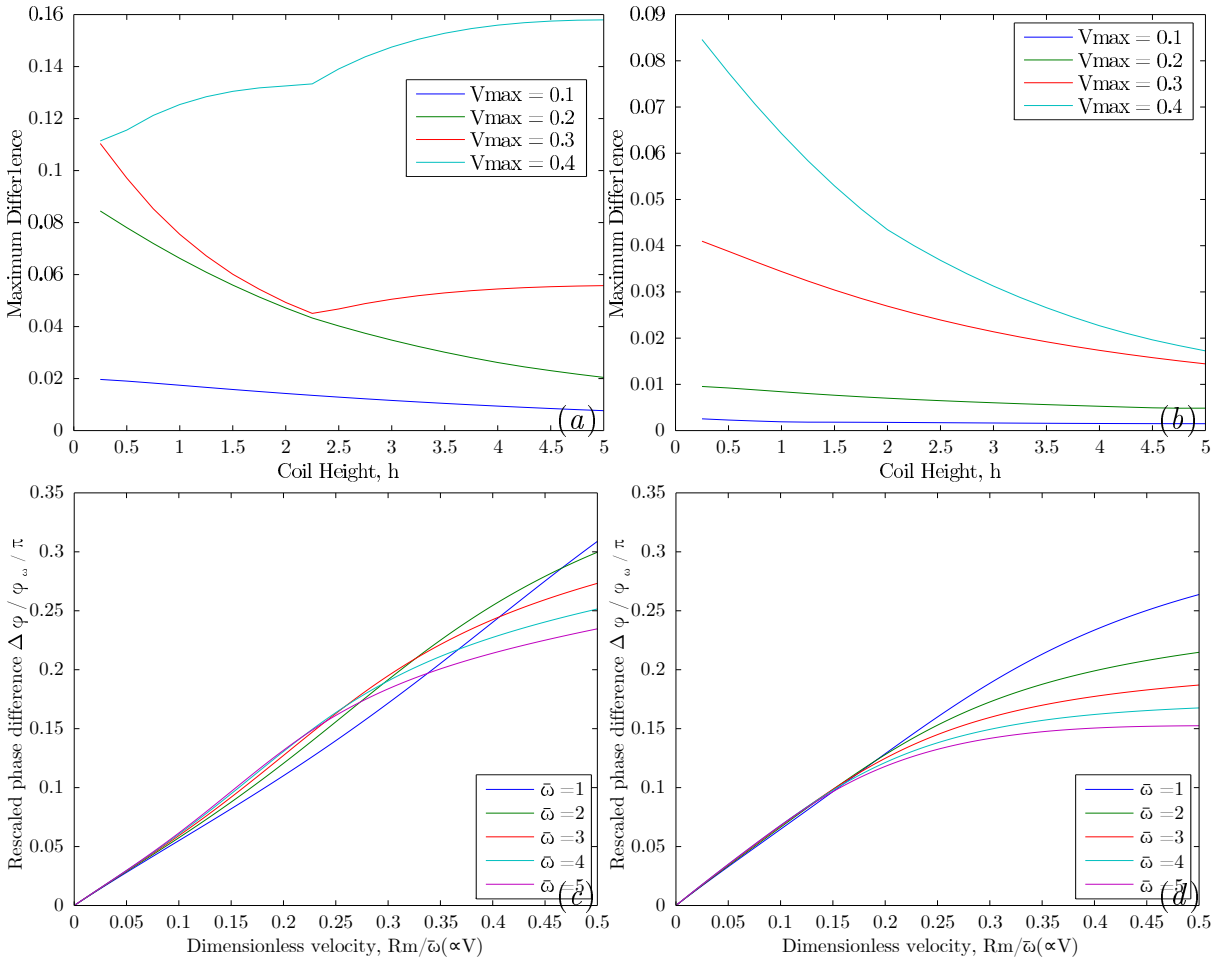

Figure 17: Maximum difference in rescaled phase shift measurement for dimensionless velocities up to $Vmax$ with measurement coils located at $x = \pm 0.5$ (a) and $x = \pm 1$(b) against sending coil height. Rescale phase shift with first order rescaling against dimensionless velocity with exciting coils located at $x = \pm 0.5$ (c) and $x = \pm 5$ (d) for various dimensionless frequencies.

As previously shown the lateral positions of the receiving coils have an effect on how well the rescaling works. The horizontal position of the sending coils is now considered. A suitable measurement of this is the maximum difference between any two lines, which relates physically to the maximum error in the rescaled phase shift measurement caused by removing conductivity from the measurement scheme. Figure 17(a) and (b) show the maximum difference in rescaled phase measurement for dimensionless frequencies 1, 2, 3, 4 and 5. It can be seen that having the sending coil further out leads to lower variation between different dimensionless frequencies. It is also shown that in most cases having the sending coil further from the flow leads to lower differences. It is shown that the measurement scheme is more robust when looking only at lower velocities. figure 17(d) shows that when the wires representing the sending coil are taken the extreme and likely impractical locations of $x = \pm 5$ that the lines collapse better for a greater range. This

can be seen to agree with the last point in the previous section that further separated observation points yield worse results, as here the opposite is shown, that having the observation points closer together relative to the sending coil yields better results.

4.3 Summary

In this chapter, a theoretical design for an improved phase shift flowmeter has been introduced. This design is shown to be able to reduce the conductivity dependence of the measurement scheme. This is done by employing the reference phase shift which is induced on the field by the presence of the conducting layer to the measurement scheme. A measure of the reference phase taken from the upstream receiving coil. There are two rescalings introduced where a reference phase shift is used to rescale the measurement scheme. Firstly, for low frequencies $\bar{\omega} \lesssim 1$, where there is a direct relationship between phase shift and the frequency, rescaling the flow-induced phase shift with the square of the reference phase can help remove conductivity from the measurement scheme. At higher ac frequencies $\bar{\omega} \gtrsim 1$, where the shielding effect causes the variation of phase with the frequency the be non-linear, conductivity can be removed from the measurement scheme by rescaling the flow-induced phase shift directly with the reference phase.

5 Pulsed Field Flowmeter

In this section we will consider an axisymmetric cylindrical model. We shall again first consider a field represented by a standing wave and then The field generated by a number of coils. In this model the effect of a pulsed field will be considered for both of these field definitions.

5.1 Mathematical Model

Consider a cylinder of infinite length, oriented along the z-axis, radius R and conductivity σ moving at a velocity of $\vec{v} = \vec{e_z}v$. The derivation for the cylindrical model starts identically to the 2D Cartesian model. starting with the Maxwell Faraday equation, Ohms law and its expansion and Amperes Law given by equations (21-23) and (25). In this model, we shall again assume that the frequency is low enough that we can neglect the displacement current and use Amperes Law:

$$\vec{j} = \frac{1}{\mu_0}\vec{\nabla} \times \vec{B}. \tag{56}$$

We consider now that the magnetic field is axisymmetric and in our cylindrical coordinate system (with axis labelled r, ϕ and z) will have only r and z components. As with the Cartesian model, presented in the previous chapter, the magnetic field can be represented by a single component of the vector potential. However, in this model the component which will be used is the azimuthal component. This means we have a purely azimuthal vector potential, $\vec{A} = \vec{e}_\phi A$. By evaluating the curl it can be shown that

$$\vec{B} = -r^{-1}\vec{e}_\phi \times \vec{\nabla}(rA).$$

A useful feature of this model is that the streamlines of $\vec{B}$ run along the isolines of rA. This can be shown by appling the cross product with the unit vector in the azimuthal direction. The triple product produced on the right hand can be simplifed using idenities leading to, $\vec{e}_\phi \times \vec{B} = r^{-1}\vec{\nabla}(rA)$. Taking the dot product of this with $\vec{B}$ leads to $\vec{B}\cdot\vec{\nabla}(rA) = 0$ which shows that the streamlines of $\vec{B}$ run along isolines of rA.

The advection diffusion equation for this model takes the form

$$\mu_0\sigma(\partial_t A + v\partial_z A) = \vec{\nabla}^2 A, \tag{57}$$

which is derived by applying Ampere's Law (56) to Ohm's Law (23) as is done to derive equation (28) in the previous chapter. In free space, equation (57) takes the form

$$(r^{-1}(rA)')' + \partial_z^2 A = 0. \tag{58}$$

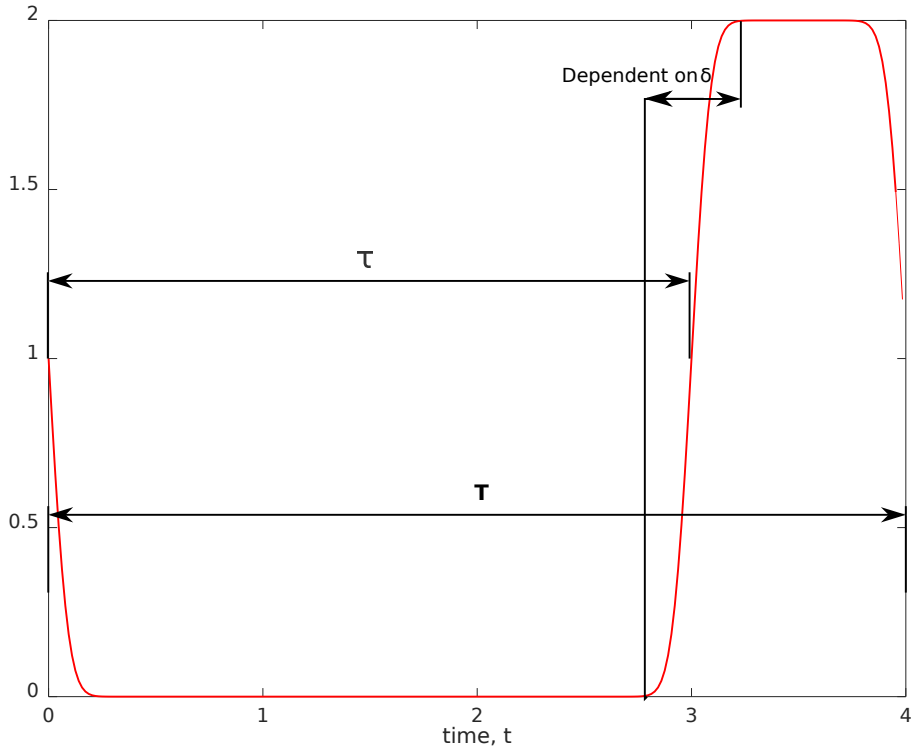

Figure 18: Pulse profile labeled wih key variables, T the length of one period of the periodic signal, τ the time between pulses and δ which sets the transition time while the field turns on and off.

where $'$ denotes the derivative with respect to r. To solve this equation we now consider the eddy currents induced by the external magnetic field in the form of a single Fourier harmonic which varies as

$$A_0(r, z, t) = \hat{A}_0(r) \sin(kz) f(t)$$

where, as before, k is the wave number in the z direction and $f(t)$ defines the time variation of the applied field. The time variation due to the pulsed nature of the magnetic field is defined by

$$f(t) = \begin{cases} \eta(t) + \eta(\tau - t) - \eta(T - t), & 0 \leq t < T \\ f(t - T), & t > T \end{cases} = \sum_{n=-N/2}^{N/2} f_n e^{i\omega_n t}$$

This, firstly, describes the periodic nature of the pulsing of the field. Secondly, the function is defined using the complementary error function $\eta(t)$=erfc$(t/\delta) = \frac{2}{\sqrt{\pi}} \int_{t/\delta}^{\infty} e^{-t^2} dt$. This introduces a transition time δ whilst turning the field on or off. This transition time is necessary to suppress the Gibbs phenomenon in the Fourier series representation of $f(t)$.

The Fourier coefficients f_n for the modes are computed using the FFT. These modes are generated for dimensionless frequencies $\omega_n = 2\pi n/T$. The solution for the vector

potential can be represented in complex form as

$$A(r,z,t) = \sum_{n=-N/2}^{N/2} \Im\left[\hat{A}_n(r) f_n e^{i(\omega_n t + kz)}\right] \tag{59}$$

where $\hat{A}_n$ is the solution to (60) given in general form by (61).

We can now write equation (58) in the following form

$$(r^{-1}(rA)')' - r^{-2}\hat{A}_0 - k^2\hat{A}_0 = 0 \tag{60}$$

For which the general solution is

$$\hat{A}_n(r) = CI_1(kr) + D_n^o K_1(kr), \tag{61}$$

where $I_\nu(x)$ and $K_\nu(x)$ are the modified Bessel functions of the first and second kind respectively, with order ν; C is an unknown constant defined by the applied magnetic field and D_n^o is an unknown constant associated with the n-th time harmonic of the induced magnetic field.

5.1.1 Solution for Mono Harmonic Standing Wave

For the case of the applied field taking the form of a standing wave, there are two regions which the system can be resolved in: inside the layer and outside of the layer. The standing wave shall, as in the previous model, be represented by two oppositely travelling waves.

We now set the radius of the conducting R as the length scale and the time scale as $\mu_0\sigma H^2$. We can now introduce two key dimensionless parameters. A dimensionless velocity, the magnetic Reynolds number $Rm = \mu_0\sigma VH$ and the dimensionless frequency, $\bar{\omega}_n = \mu_0\sigma\omega_n R^2$. Outside the conducting cylinder, the solution is governed by equation (61). Inside the conducting layer the solution is governed by equation (57), which takes the form

$$(r^{-1}(r\hat{A}_n)')' - (k_n^2 + i(\bar{\omega}_n + k_n Rm))\hat{A}_n = 0.$$

With the substitution $\kappa = (k_n^2 + i(\bar{\omega}_n + k_n Rm))^{1/2}$ the solution to this equation for the field inside the conducting layer is given by

$$\hat{A}_n(r) = D_n^i I_1(\kappa r). \tag{62}$$

This solution is chosen such that the term concerning the modified Bessel function of the second kind, $K_\nu(x)$, is omitted as it is not regular at $r = 0$. The continuity of the vector potential and its normal derivative at the interface between the conducting region and

free space, $r = R = 1$, gives boundary conditions which will lead to the solutions for the unknown constants D_n^o and D_n^i.

Firstly $[\hat{A}]_{r=1} = 0$ gives

$$D_n^i I_1(\kappa) = C I_1(k_n) + D_n^o K_1(k_n) \tag{63}$$

and $[\partial_r \hat{A}]_{r=1} = 0$ gives

$$D_n^i (I_0(\kappa) - \frac{1}{\kappa} I_1(\kappa)) = C(I_0(k_n) - \frac{1}{k_n} I_1(k_n)) + D_n^o(-K_0(k_n) - \frac{1}{k_n} K_1(k_n)).$$

For the derivatives of the modified Bessel functions the recurrence relationship $\partial_z L_\nu(z) = L_{\nu-1}(z) - \frac{1}{z} L_\nu(z)$ found in [1], where L substitutes either I_ν or $e^{i\pi\nu} K_\nu$, has been used. Simple manipulation and substitution of these equations at the boundary yields solutions for the two unknowns

$$D_n^o = C \frac{k_n I_0(k_n) I_1(\kappa) - \kappa I_0(\kappa) I_1(k_n)}{k_n K_0(k_n) I_1(\kappa) + \kappa I_0(\kappa) K_1(k_n)}$$

$$D_n^i = C \frac{k_n (K_0(k_n) I_1(k_n) + I_0(k_n) K_1(k_n))}{k_n K_0(k_n) I_1(\kappa) + \kappa I_0(\kappa) K_1(k_n)}.$$

For this solution the current amplitude of the applied field is defined by C. as the amplitude is irrelevant in our study we can set $C = 1$.

5.1.2 Solution for A Circular Current Loop

The solution above, for a mono-harmonic applied field can be extended to the case of a coil, made of circular loops. Considering a single thin loop placed azimutally with radius r_c located axially at z_c carrying a dimensionless current of j_c. The free-space distribution of the vector potential amplitude will consist only of the ϕ-component and can be described using the Dirac delta function„

$$\vec{\nabla}^2 A_0 = -j_c \delta(\vec{r} - r_c \vec{e}_r - z_c \vec{e}_z), \tag{64}$$

where $\delta(\vec{r})$ is the Dirac delta function. Note that as the model is azimuthally symmetric the loop is oriented along the ϕ direction with constant r and z values. An axial Fourier transform $\hat{A}(r) = \int_{-\infty}^{\infty} A(r,z) e^{ik_n z}\, dz$ converts equation (64) to

$$(r^{-1}(r\hat{A}_0)')' - k_n^2 \hat{A}_0 = -j_c e^{-ik_n z_c} \delta(r - r_c). \tag{65}$$

The solution to this equation must be continuous across the coil, $r = r_c$, regular at $r = 0$ and decay as $r \to \infty$. The last two conditions are met by our choice of which part of the

solution to utilise,

$$\hat{A}_0(r) = D_I I_1(k_n r) + D_K K_1(k_n r)),$$

which is based on the general solution given by equation (61).

In the regions $0 < r < R$ and $R < r < r_c$, inside the cylinder and from the cylinder to the coil, the solution can be taken as $\hat{A}_0(r) = D_I I_1(k_n r)$ and from the coil to infinity the solution is given by $\hat{A}_0(r) = D_K K_1(k_n r)$.

The constants D_I and D_K are solved by the boundary conditions on A at the coil. The values at the coil must match and the change in derivative is obtained by integrating equation (65) over the singularity caused by the presence of the coil at $r = r_c$. Giving the boundary conditions, firstly based on the value $\left[\hat{A}_0\right]_{r=r_c} = 0$, as

$$D_I I_1(k_n r_c) = D_K K_1(k_n r_c)$$

and for the derivative $\left[\partial_r \hat{A}_0\right]_{r=r_c} = -j_c e^{-ik_n z_c}$,

$$D_I \left(I_0(k_n r_c) - \frac{1}{k_n r_c} I_1(k_n r_c) \right) + D_K (K_0(k_n r_c) + \frac{1}{k_n r_c} K_1(k_n r_c)) = -j_c e^{-ik_n z_c},$$

which can be reduced to, by subtracting the other boundary condition, the following form:

$$D_1 k_n I_0(k_n r_c) + D_K k_n K_0(k_n r_c) = -j_c e^{-ik_n z_c}$$

$$D_I \left(I_0(k_n r_c) - \frac{1}{k_n r_c} I_1(k_n r_c) \right) + \frac{I_1(k_n r_c)}{K_1(k_n r_c)} \left(K_0(k_n r_c) + \frac{1}{k_n r_c} K_1(k_n r_c) \right) = -2 j_c e^{-ik_n z_c}$$

In the region $0 < r < r_c$ the solution can be taken as

$$\hat{A}_o(r) = -j_c e^{-ik_n z_c} \frac{\frac{I_1(k_n r)}{I_1(k_n r_c)}}{k_n \left(\frac{I_0(k_n r_c)}{I_1(k_n r_c)} + \frac{K_0(k_n r_c)}{K_1(k_n r_c)} \right)},$$

for the region $r_c < r < \infty$, from the coil outwards, as

$$\hat{A}_o(r) = -j_c e^{-ik_n z_c} \frac{\frac{K_1(k_n r)}{K_1(k_n r_c)}}{k_n \left(\frac{I_0(k_n r_c)}{I_1(k_n r_c)} + \frac{K_0(k_n r_c)}{K_1(k_n r_c)} \right)}.$$

The vector potential in physical space is given by the inverse Fourier transform, computed using the FFT.

This method can be applied to multiple current loops each loop will have an additive effect on the field with current for each coil being introduced by substituting

$C = \sum_c D_c / I_1(k_n r_c)$ into equation (61) where

$$D_c = \frac{-j_c e^{-ik_n z_c}}{k_n \left(\frac{I_0(k_n r_c)}{I_1(k_n r_c)} + \frac{K_0(k_n r_c)}{K_1(k_n r_c)} \right)}$$

and the summation is taken over the current loops.

5.2 Eigenmode Evolution

To describe the basics of the pulsed field approach introduced above, the evolution of separate eigenmodes shall be investigated. The separate eigenmodes will be sought in the following complex form,

$$A(r, z, t) = \hat{A}(r) e^{ik_n z - \gamma t}, \tag{66}$$

where k_n is a given real wave-number introduced in the derivation above and γ is an unknown complex decay rate. This complex decay rate will be determined together with the amplitude distribution $\hat{A}(r)$ by solving the eigenvalue problem posed by equation (57). If we remove the external magnetic field, the solution for the region where measurements would be taken, outside the cylinder, given be equation (63) can be expressed as

$$\hat{A}(r) = D^o K_1(k_n r), \tag{67}$$

where D^o is an unknown constant. Inside the cylinder, the general solution of equation (57) is given by

$$\hat{A}(r) = D^i J_1(\alpha r),$$

where D^i is another unknown constant, $J_\nu(x)$ is the Bessel function of the first kind with order ν, and $\alpha = (\gamma - k_n^2 - ik_n Rm)^{1/2}$. The boundary conditions based on the continuity of A and its derivative across the surface of the layer $r = R = 1$ can solve for the two unknowns, D^0 and D^i. Firstly the continuity condition $\left[\hat{A}\right]_{r=1} = 0$ gives

$$D^o K_1(k_n) = D^i J_1(\alpha)$$

And the derivative across the boundary $\left[\partial_r \hat{A}\right]_{r=1} = 0$ gives

$$D^o (K_0(k_n) + \frac{2}{k_n} K_1(k_n)) = D^i (J_0(\alpha) - \frac{2}{\alpha} J_1(\alpha)).$$

These boundary conditions lead to the following characteristic equation

$$\alpha J_0(\alpha)/K_0(k_n) + k_n J_1(\alpha)/K_1(k_n) = 0. \tag{68}$$

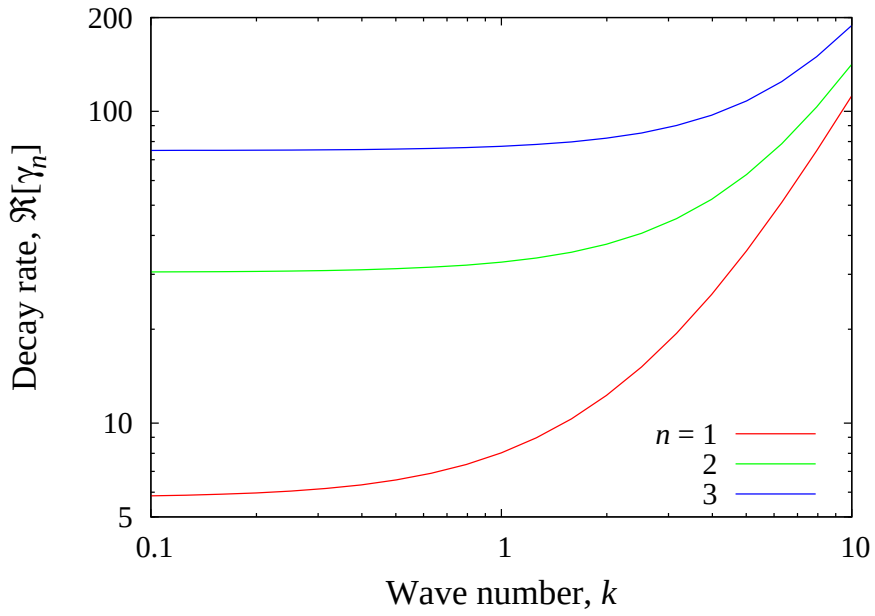

Figure 19: Three lowest eddy current decay rates versus the wave number. Note that modes for $n \geq 4$ will have significantly higher decay rates, and thus significantly shorter decay times.

This equation has real roots given by α which define the associated complex decay rates introduced in equation (66) as

$$\gamma = \alpha^2 + k_n^2 + ik_n Rm. \tag{69}$$

The most important result that follows from this expression is the phase speed is constant, shown by $\Im[\gamma]/k_n = Rm$. This is the speed at which all eddy current patterns travel regardless of their wave number. The corresponding physical velocity for the eddy current patterns is given by $Rmv_m = v$ and is equal to that of the medium. Here $v_m = (\mu_0 \sigma R)^{-1}$ is the velocity scale for the model. This leads to the conclusion that the velocity of the medium can be determined by measuring the phase velocity at which an eddy current pattern is advected. This is the main concept underpinning how transient eddy-current flowmetering operates.

The second important result which can be taken from equations (68&69) concerns the decay rate given by the real part of the complex associated decay rate $\Re[\gamma]$. Figure 19 shows $\Re[\gamma]$ versus wavenumber k_n for the first three dominant eigenmodes. It can bee seen that the lowest decay rates occur in the limit $k_n \to 0$ which is associated with long wave patterns. In this limit, the characteristic equation, given by equation (68), can be reduced to $J_0(\kappa) = 0$ which yields $\Re[\gamma_1] \approx 5.78$. This means that the eddy current amplitude drops by almost three orders of magnitude over the characteristic magnetic diffusion time $t_m = \mu_0 \sigma R^2$. The decay times of subsequent eigenmodes are significantly shorter, as shown by the significantly higher rates in figure 19. The figure is limted to

the domnant three modes as higher modes will have higher decay rates and will become insignificant due to their short decay times. This means that the period of time during which a tracking a transient eddy current pattern is feasible is limited by a few magnetic diffusion time scales t_m. This result also implies that the respective dimensionless distance over which the pattern is advected is limited by a few Rm.

The measurement of the phase velocity of the field induced by the eddy currents is not as simple as measurement would be for a simpler wave with constant amplitude. The phase velocity measures the rate at which the phase propagates spatially. For a simple wave with constant amplitude, this is equivalent to the motion of a point of fixed amplitude. In the case of the decaying field, the only points with fixed amplitude are the nodes, or points at which the oscillating amplitude passes through zero.

Along with the nodes of the oscillating amplitude some other features are present, which behave similarly to that of a point of fixed amplitude, whos motion is equivilent to the phase velocity. Firstly the spatial derivative can be used as local spatial extrema which will be also fixed in the decaying wave. And secondly instead ofusing the field amplitude to find a fixed point a temporal extrema of the field can be traced, where zero crossings in the time derivative will also give fixed points in the decaying wave. This time derivative of the magnetic flux is associated with the emf induced by the decaying eddy currents, $\mathcal{E} = -\partial_t \Phi$, which gives rise to voltage in the pick-up coils. Finally the extrema of the emf may also be used to measure the phase velocity of the eddy currents. Both spatial extrema, $\partial_z \mathcal{E} = 0$, and temporal extrema, $\partial_t \mathcal{E} = 0$, of the emf will have zero crossing points which could be used for measurement.

5.3 Mono-Harmonic Eddy Current Distribution

In this section, we consider a pulsed external magnetic field which is switched off and on periodically at the dimensionless time intervals $\tau = 3$ and $T - \tau = 1$. The field takes the form of a standing wave which represents a single harmonic for the field generated by simple coils in the next section. The eigenvalue analysis in the previous section suggests that these time intervals are long enough for the eddy currents to develop. The development of the eddy currents is confirmed by the time variation of the magnetic flux, $\Phi = rA$, which is caused by the presence of the eddy currents. This temporal variation of the magnetic flux is shown in figure 20(a) with wavenumber $k_n = 1$ at $z = 0.5$ with measurements taken at three different radii with the conducting media at rest ($Rm = 0$). The corresponding variation of the emf magnitude is plotted in figure 20(b) for both the layer at rest and in motion. When the cylinder is at rest ($Rm = 0$), the emf can be seen to decrease exponentially with time as predicted by the previous eigenvalue analysis. When the cylinder moves with velocity $Rm = 1$, the decrease of emf is accompanied by a zero crossing, which occurs at the time instant $t \approx 0.5$, for the measurement location $z = 0.5$.

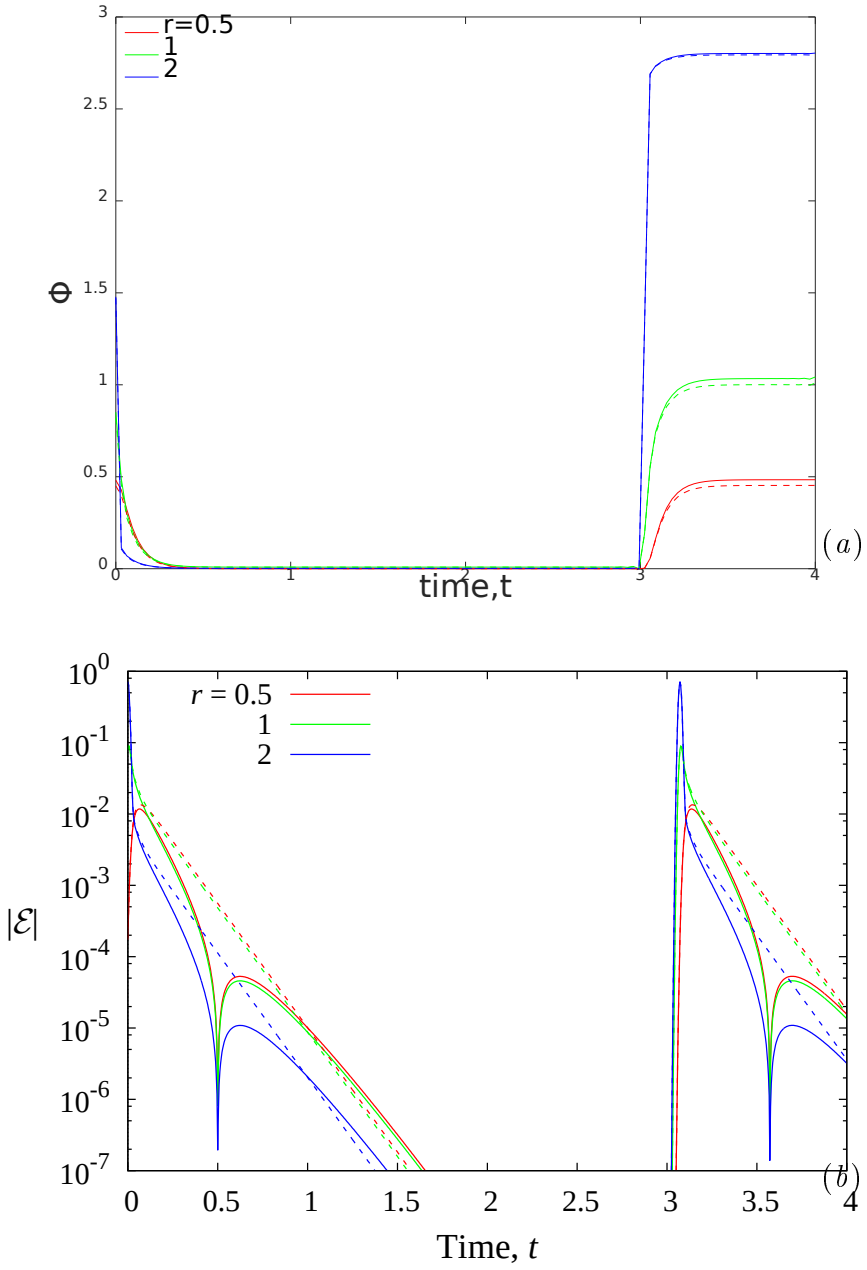

Figure 20: Variation of the magnetic flux $\Phi = rA$ over one time period at $z = 0.5$ and $r = 0.5$, 1, 2 for the Fourier harmonic with the wave number $k_n = 1$ for $Rm = 0$ (dashed) and $Rm = 1$ (solid) (a); variation of the emf magnitude $|\partial_t \Phi|$ with time at the same points for $Rm = 0$ (dashed) and $Rm = 1$ (solid) (b).

This zero crossing point is seen as a cusp on the semi-logarithmic plot of $|\mathcal{E}|$ in figure 20(b). Shortly after passing through zero, emf is seen to attain a local extremum, which is defined mathematically by a zero crossing of $\partial_t \mathcal{E}$.

Figure 21 shows the evolution of the magnetic field pattern and the associated emf for wave number $k_n = 1$ after the external magnetic field is switched off with the conducting cylinder moving at a velocity given by $Rm = 1$. In the middle row the increased density of isolines show the locations of the zero crossings of the emf these zero crossings follow closely to the motion of the medium as seen by there locations at $z = tRm$. This movement of the zero crossing with the velocity of medium means that the velocity can be determined directly from measurements as $Rm = z/t$, where z is the axial distance of the observation point from the wave node and t is the time at which the emf passes through zero at that point after switching the field off. The magnetic flux lines, which are shown at the top row of figure 21, can be seen to run slightly in front of the flux lines of the emf. This is due to the effect of advection which tilts the magnetic flux lines in the direction of motion. This can be seen in the upper left plot, where at $t = 0$, the flux lines are pulled along in the direction of the flow. In contrast to this, the time derivative, which is mathematically equivalent to multiplying the dominating eigenmode, in equation (66), by $-\gamma$ this has a phase shift of $\arg(-\gamma)$ in the associated field pattern. This will cause the pattern of $\partial_t \mathcal{E}$, which is shown in the bottom row of figure 21, to lag slightly behind the pattern of $\mathcal{E}$. Note that the zero crossings of $\partial_t \mathcal{E}$, similar to those of $\mathcal{E}$ are marked by the increased density of the isolines. The spatial extrema of $\mathcal{E}$ are defined by the zero crossings of $\partial_z \mathcal{E}$. With this simplified mono-harmonic applied field the distribution is given by $\partial_z \mathcal{E} = ik_n \mathcal{E}$ which is shifted by a quarter wave length relative to that of $\mathcal{E}$. Therefore the spatial extrema of the emf in a mono-harmonic wave will move in exactly the same way as the zero crossings.

Figure 22(a) shows that the emf for the distributions for both wave numbers $k_n = 1, 0.5$ can be seen to decay in a good agreement with the analytically determined damping rates, shown as dashed lines in the figure.

Zero crossings outside the cylinder are shown in Fig. 21 to occur synchronously along a radius. For this reason here we choose to focus on the emf distribution along the surface $r = 1$. Figure 22(b) shows the zero crossing positions of both $\mathcal{E}$, $\partial_t \mathcal{E}$, $\partial_z \mathcal{E}$ and $\partial_z \Phi$ against time for wave number $k_n = 1$ at three different velocities $Rm = 0.1, 0.5, 1$. The zero crossing points of $\mathcal{E}$ and $\partial_z \mathcal{E}$ move in exactly the same way with a velocity of Rm starting from the node at $z = 0$. The temporal extrema points, which correspond to zero crossings of $\partial_t \mathcal{E}$, also move at the same velocity as the medium but with a time delay which depends both on the wave number k_n and the velocity Rm. This means that at least two measurement points are required to eliminate this offset and, thus, to determine the velocity of the medium using temporal extrema of emf.

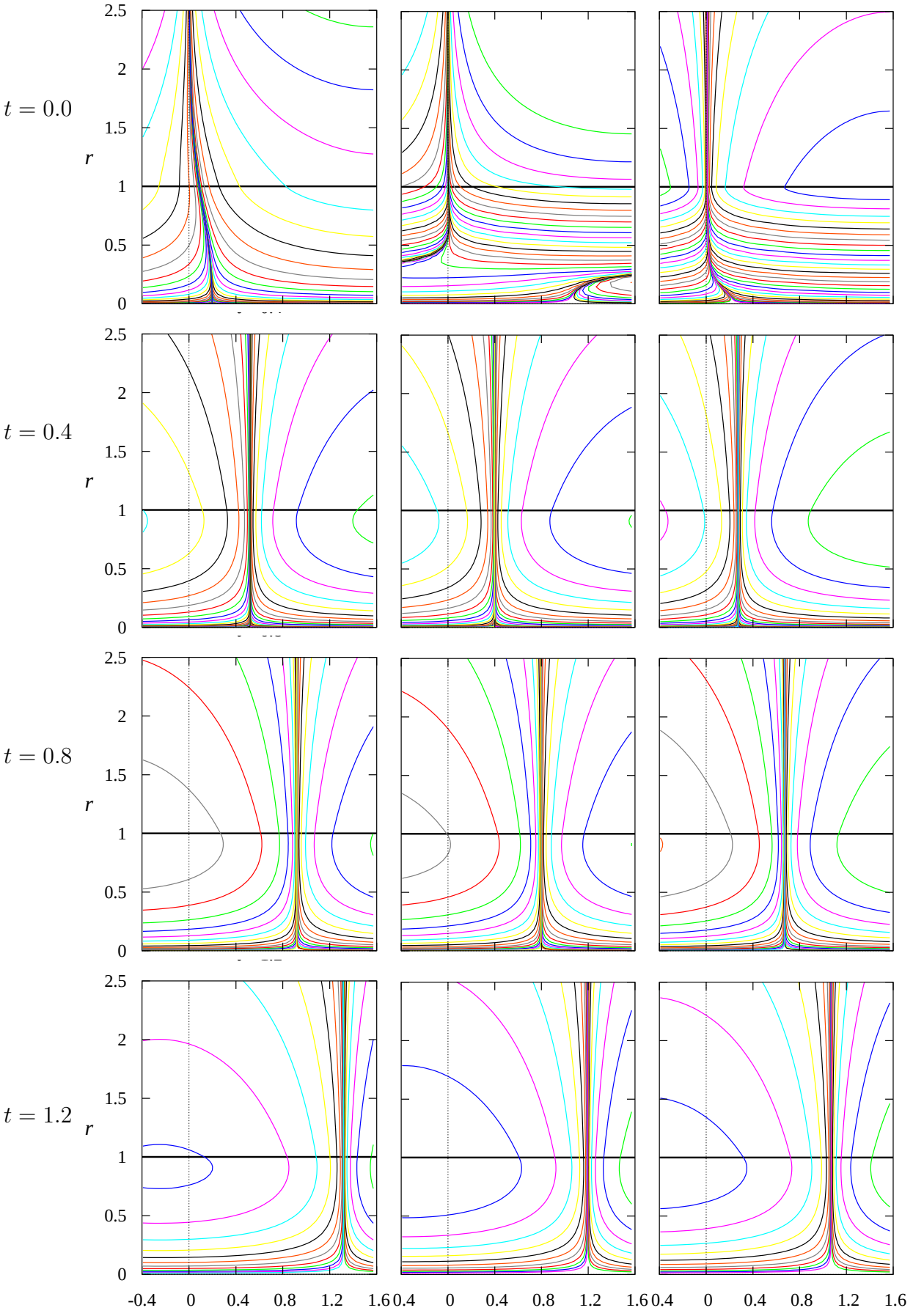

Figure 21: The magnetic flux lines (Φ = const) (left), the isolines of emf $\mathcal{E} = -\partial_t \Phi$ (middle), and of $\partial_t \mathcal{E} = -\partial_{tt}^2 \Phi$ (right) for $Rm = 1$ at the time instants $t = 0$, 0.4, 0.8, 1.2 after a mono-harmonic external magnetic field with the wave number $k_n = 1$ has been switched off. Subsequent isolevels differ by a factor of two and cluster around zero value.

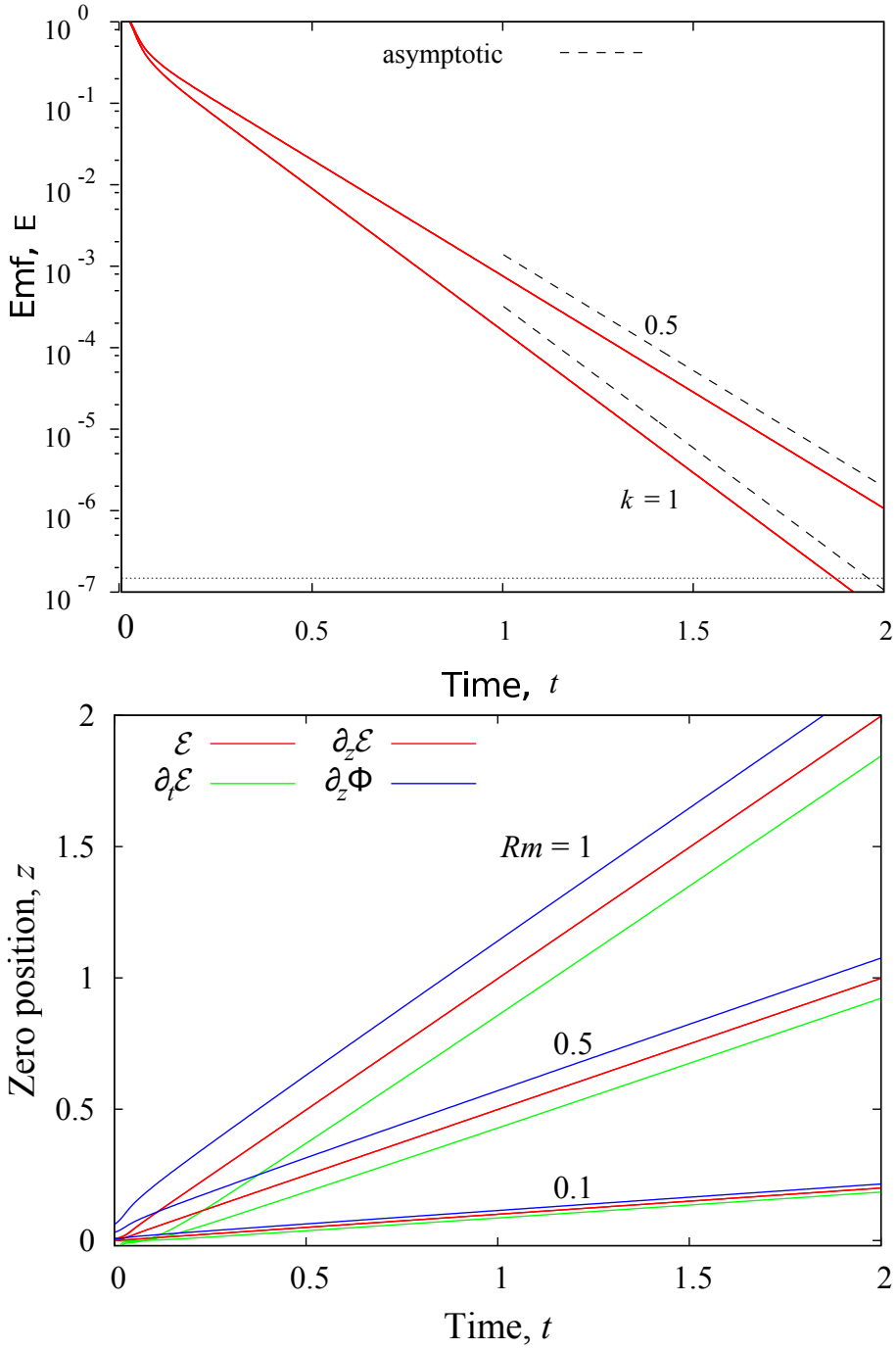

Figure 22: (b) Relative magnitude of $\mathcal{E}$ against time for mono-harmonic eddy current distributions with $k_n = 0.5, 1$.(c) Axial zero crossing positions of $\mathcal{E}$, $\partial_t\mathcal{E}$, $\partial_z\mathcal{E}$ and $\partial_z\Phi$ for the eddy current distributions generated with $Rm = 0.1, 0.5, 1$ for $k_n = 1$.

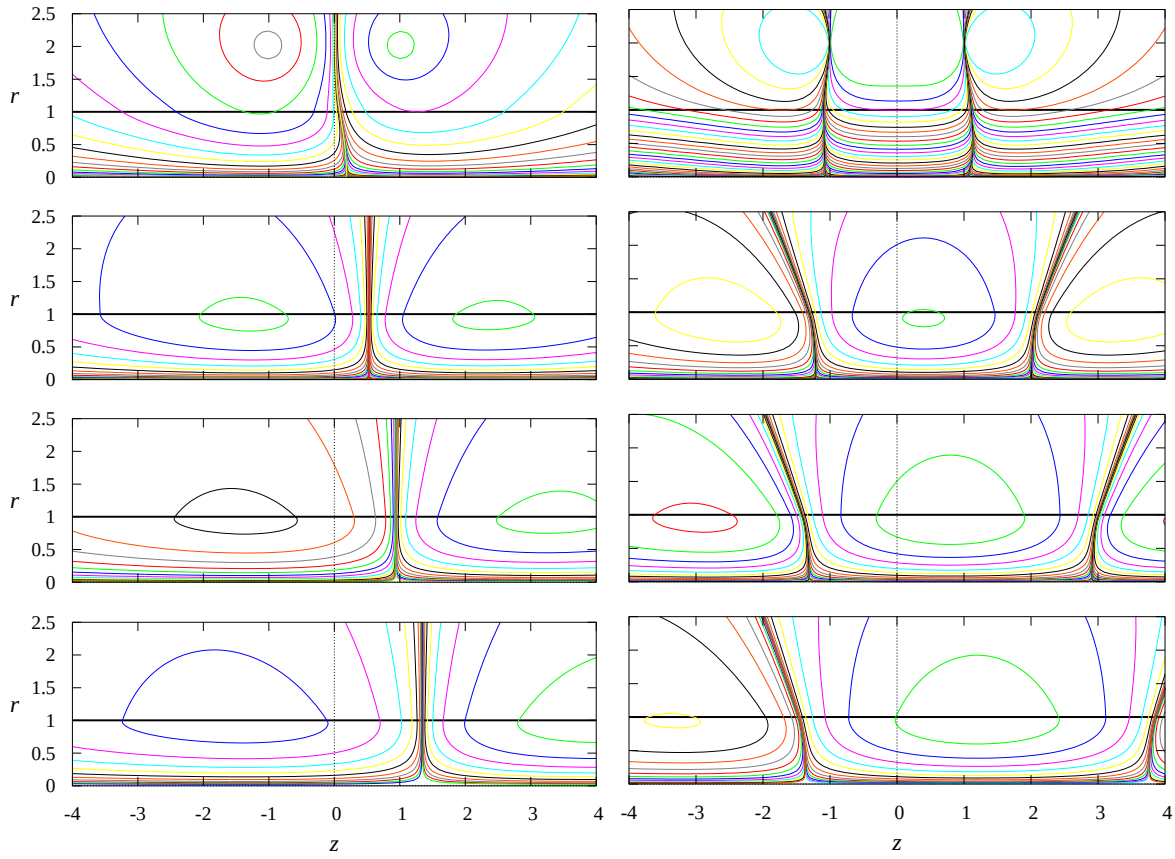

Figure 23: The magnetic flux lines (Φ = const) (left) and the isolines of $\partial_z \mathcal{E} = -\partial^2_{tz}\Phi$ (right) at the time instants $t = 0,\ 0.4,\ 0.8,\ 1.2$ after the external magnetic field generated by a pair of anti-symmetric current loops with radius $r_c = 2$ located at $z_c = \pm 1$ has been switched off.

5.4 Eddy Currents Induced By Circular Loops

The eddy currents generated by more realistic coils are investigated in this section. These coils are represented by simple circular current loops. The first coil layout which will be considered is that of a pair of loops located at $z_c = \pm 1$ and $r_c = 2$ carrying equal but opposite currents. This configuration is designed to give similarities to a node in the mono-harmonic distribution discussed previously, the symmetry plane at $r = 0$ is analogous to such a node.

As a result, the nature of the advection of the field pattern by the moving medium, which is shown for $Rm = 1$ in figure 23(left), is noticeably similar to the field pattern for the mono-harmonic eddy current distribution in figure 21(left). In a similar manner, the zero crossing points of both $\mathcal{E}$ and $\partial_t \mathcal{E}$ move in the same way as they did in the mono-harmonic wave. There is one substantial difference between the mono-harmonic and anti-symmetric eddy-current distributions which concerns the motion of spatial extrema of emf. In this model, there are two such extrema which can be seen in figure 23(right). These extrema are located initially at the current loops where the increased

density of isolines show the location of the zero crossings of $\partial_z \mathcal{E}$. It is obvious that these extrema do not move at the same velocity. The right (downstream) extremum moves noticeably faster than the medium whereas the left (upstream) one moves not only much slower but also in the opposite direction. In the example here the movement is slight but it is perceivable that the upstream zero crossings do travel upstream, against the flow over time. The gap in between the zero crossings appears to grow fairly uniformly however physical measurements of this would be impractical. The main difference between the spatial extrema in the previous mono-harmonic and the present two-loop eddy current distributions is the absence of symmetry in the latter. It will be shown later that symmetry is crucial to the transient eddy current flowmetering.

A single loop can generate an eddy current distribution with a spatially symmetric emf extremum. However it will not have zero crossings in the emf amplitude. Figure 24 shows the evolution of the field generated by a current carrying coil at $z_c = 0$ with radius $r_c = 2$ with the conducting cylinder in motion with a velocity $Rm = 1$. For a single coil, the zero crossing are absent from the temporal evolution of the emf amplitude however the spatial extrema of both the emf and magnetic flux are present. These extrema are detected as the zero crossings of the spatial derivative of either the magnetic flux $\partial_z \Phi = 0$ or the emf $\partial_z \mathcal{E} = 0$. These zero crossings move with the medium, as with the previous model, however the nature of the relationship between the two movements are different.

The axial extremum of emf, shown in the bottom row of figure 24, is seen to move without any time lag, as the zero crossings of the emf did in the anti-symmetric set-up. The spatial extremum of the magnetic flux experiences a time lag similar to that of the temporal emf maximum in the anti-symmetric set-up. Note that the axial extremum of the magnetic flux can be detected as a zero crossing of the radial flux component B_r using, for example, a Hall sensor. At least two sensor coils are required to detect an axial maximum of emf, whereas one coil can be used to detect zero crossing or temporal extremum of emf in the anti-symmetric set-up however this requires two excitation coils.

Finally, we examine the effect of a possible asymmetry in the initial eddy current distribution generated by a two-coil set-up with opposite but slightly different currents. To characterize this kind of asymmetry we use the parameter

$$S = (j_+ - j_-)/(j_+ + j_-),$$

where j_+ and j_- are the currents in the coils placed with negative and positive z values respectively. The temporal evolution of eddy current distribution with an initial asymmetry of $S = 5\%$ generated by a pair of coils of radius $r_c = 2$ placed $z_c = \pm 1$ is shown in figure 25 with the medium at rest ($Rm = 0$). With a value of $S > 0$ the current in the left hand coil is greater than that of the right hand coil, which leads to a initial emf pattern which is asymmetrical and tilts to the right. In the anti-symmetric distribution

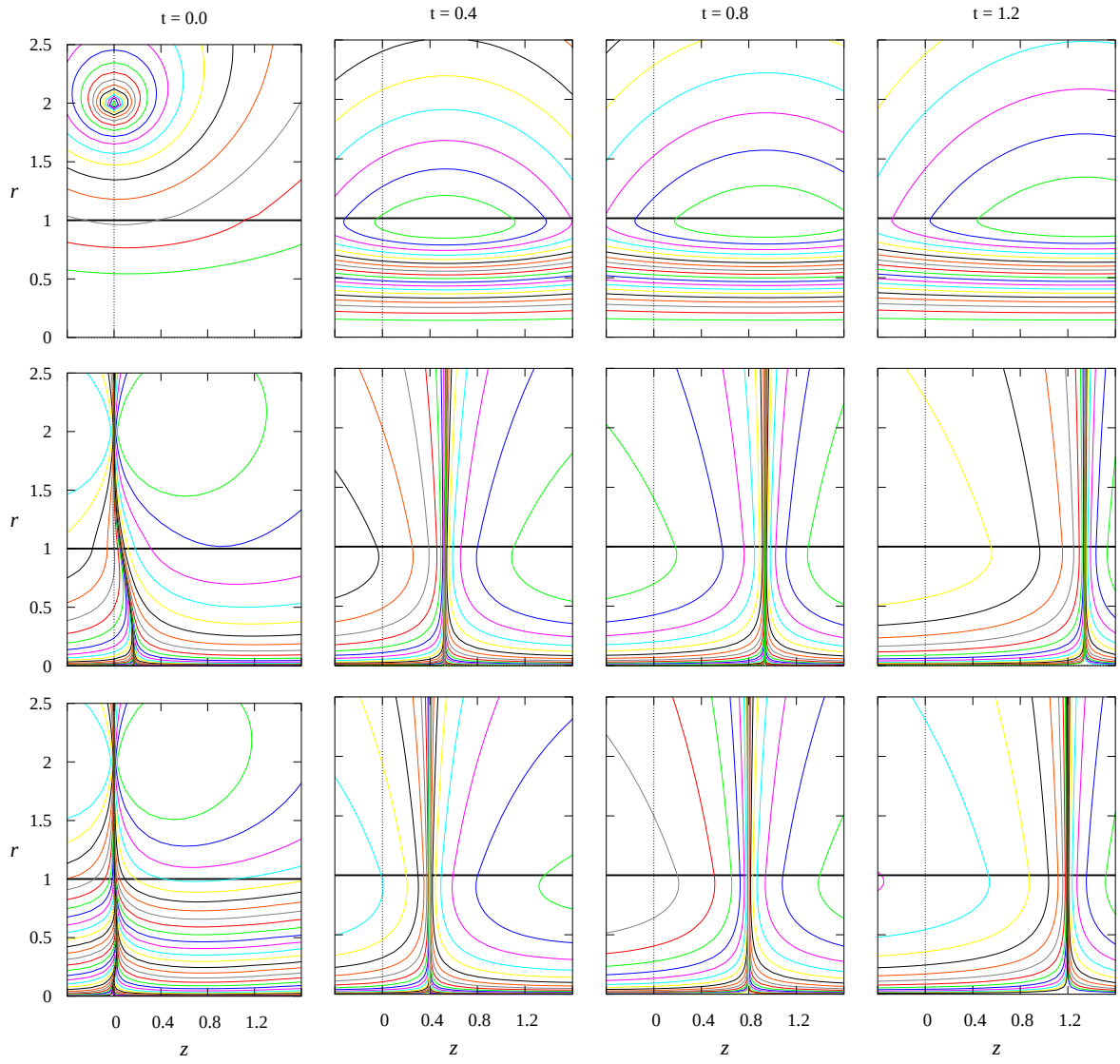

Figure 24: The magnetic flux lines ($\Phi = \text{const}$) (top), the isolines of $\partial_z \Phi$ (middle) and $\partial_z \mathcal{E} = -\partial^2_{zt} \Phi$ (bottom) for $Rm = 1$ at the time instants $t = 0, 0.4, 0.8, 1.2$ after the external magnetic field generated by a single current loop located $r_c = 2$ and $z_c = 0$ has been switched off. Levels of subsequent isolines differ by a factor of two and the increased density of isolines indicates zero value.

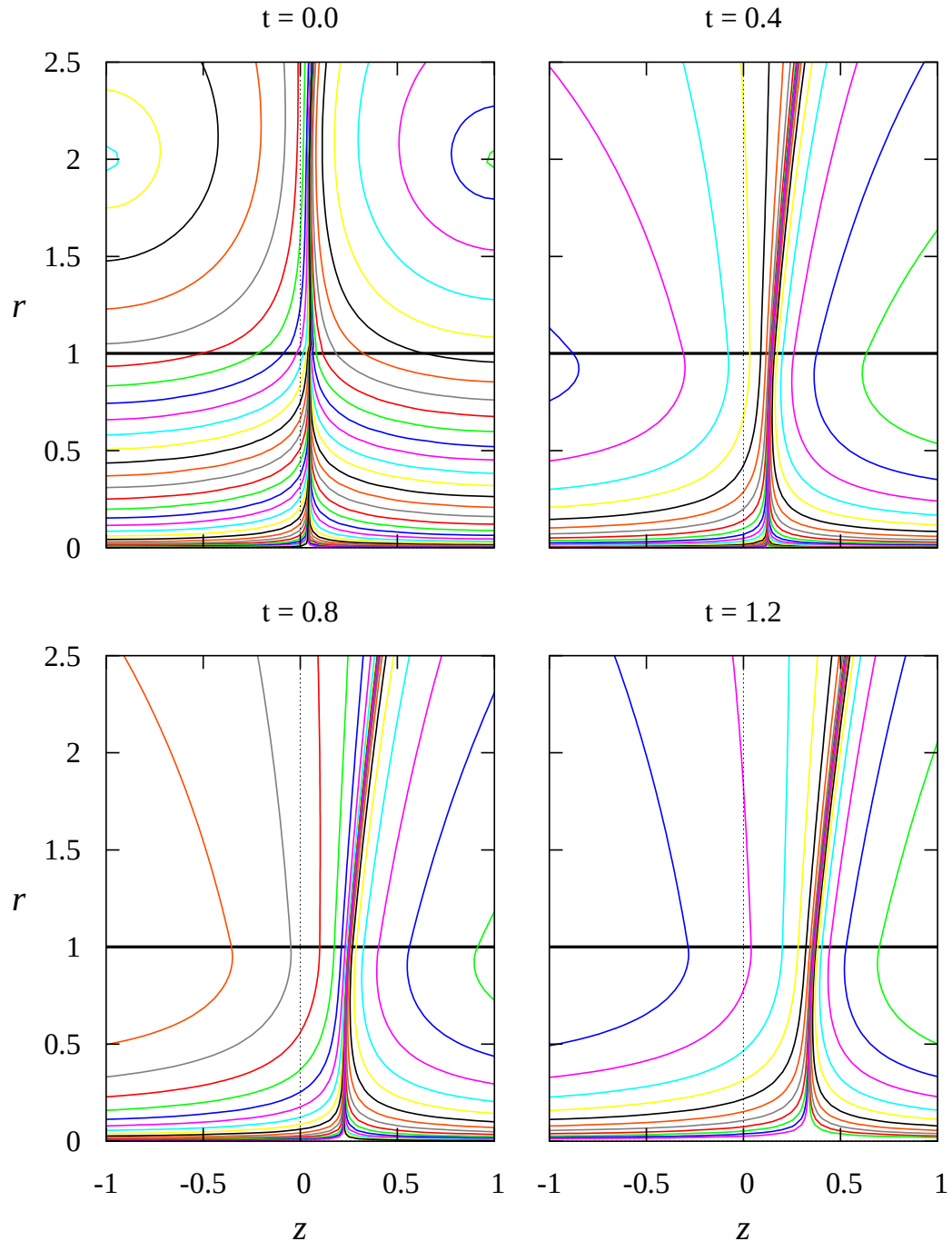

Figure 25: The emf isolines for $Rm = 0$ at the time instants $t = 0$, 0.4, 0.8, 1.2 after the external magnetic field generated by a pair of opposite current loops located at $r_c = 2$ and $z_c = \pm 1$ with the current asymmetry of $S = 5\%$ has been switched off.

with $S = 0$ the Fourier mode for each harmonic of the emf independently crosses zero at the symmetry plane, $z_c = 0$. In the asymmetric case, $S \neq 0$, this symmetry is absent and the zero crossing is a result of superposition of different Fourier modes. The decay rate which depends on the wavenumber k_n varies between the different harmonics. The variation of decay rate between Fourier modes leads to the zero crossing line in the asymmetric distribution drifting. For $S > 0$ this drift is to the right as shown in figure 25. Conversely, for $S < 0$ the drift would be to the left.

As seen in figure 26(a), after a relatively short initial transience, the drift velocity slightly increases and appears to tend to a constant value. This value rises with the asymmetry S and is nearly the same for both zero crossings and temporal extrema of the emf. The drift velocity averaged over the time interval from $t = 0$ to $t = 2.5$ is seen in figure 26(a) to increase nearly linearly with S. At the same time, the drift velocity reduces with the increase of axial separation between the coils whereas their radius has a relatively weak effect as shown in figure 26(b).

5.5 Summary

A cylindrical model was considered as a basis for the investigation into a pulsed field, or transient, eddy current flowmeter. This model initially considered a mono-harmonic field and was extended to the case of fields generated by simple current carrying loops. A numerical analysis was carried out considering several measurement schemes based on different characteristics of the magnetic field induced by the eddy current. The approaches considered either traced temporal or spatial maxima of the magnetic flux or the emf of the induced field. Temporal extrema can be measured with a single measurement loop whilst spatial extrema require a pair of loops to detect their passage.

We considered eddy current distributions generated by either two anti-symmetric circular current loops or a single loop. In a single-loop set-up, which generates a spatially symmetric eddy current distribution, the spatial extremum of emf was found to travel synchronously with the medium. In the anti-symmetric set-up, the zero crossing point of emf as well as the subsequent temporal extremum was found to travel synchronously with the medium. But this was not the case for the two spatial extrema which appear at both current loops in this set-up. These two extrema were found to move at substantially different velocities from that of the medium. This result highlights the crucial importance of symmetry to the measurement scheme.

The importance of symmetry was investigated further and it was shown that a difference of a few percentage in the currents between the exciting coils can lead to a drift of $Rm \sim 0.1$ with the typical parameters using in this chapter. This implies that transient eddy current flowmetering is heavily dependent on symmetry, and with this reasonable level of asymmetry can only be reliable for $Rm > 1$.

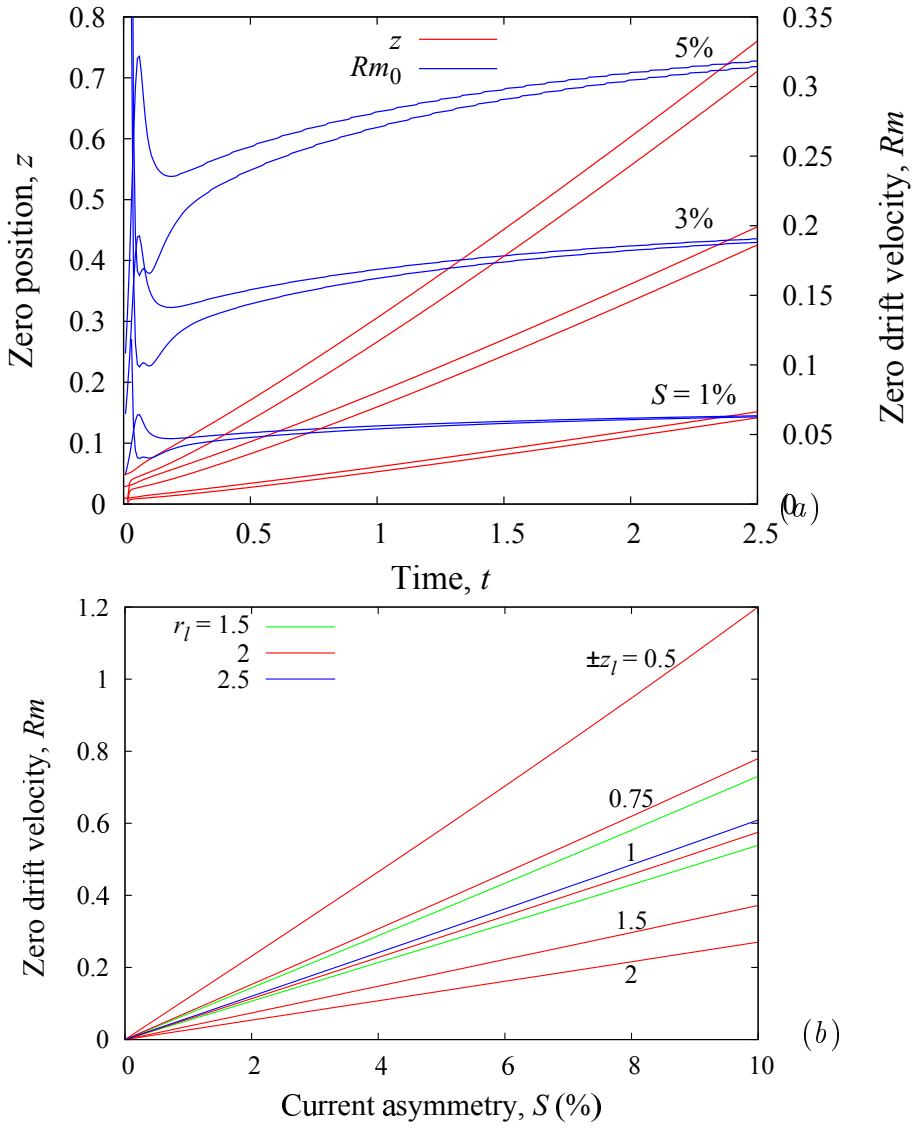

Figure 26: (a) Axial position of zero crossing and its drift velocity along the surface of cylinder at rest ($Rm = 0$) against the time after the external magnetic field generated by a pair of opposite current loops located at $r_c = 2$ and $z_c = \pm 1$ with the current asymmetry S has been switched off . The upper and lower curves correspond to the zero crossing of emf ($\mathcal{E} = -\partial_t \Phi$) and its temporal derivative ($\partial_t \mathcal{E}$), respectively. (b) Zero drift velocity depending on the current asymmetry s in two circular loops with radii $r_c = 1.5$, 2, 2.5 placed at the axial positions $\pm z_c = 0.5$, 0.75, 1, 1.5, 2.

6 3D model

In this chapter a 3D model is presented. This 3D model is designed to include more varied designs of coils for both generating the magnetic field and for taking measurements.

Firstly the derivation for the model is given along with the boundary conditions required to solve the system. In this section the process of generating an applied field based on the definition of the generating coils is also presented. Following this some proof of concept results for the model are included.

6.1 Mathematical Basis

Consider a solid infinitely long cylinder of radius R and electrical conductivity σ translating at a constant velocity $\vec{v} = \vec{e}_z v$ parallel to its axis in an external magnetic field $\vec{B}^e(\vec{r}, t)$. The external field is in general time-dependant and spatially three dimensional. The associated electric field is governed by the Maxwell-Faraday equation $\vec{E} = -\vec{\nabla}\varphi - \partial_t \vec{A}$, where φ is the electric potential and $\vec{A}$ is the vector potential, which defines the magnetic field as $\vec{B} = \vec{\nabla} \times \vec{A}$. The eddy current density induced in a moving medium is given by Ohm's law

$$\vec{j} = \sigma(\vec{E} + \vec{v} \times \vec{B}) = \sigma(-\vec{\nabla}\varphi - \partial_t \vec{A} + \vec{v} \times \vec{\nabla} \times \vec{A}). \tag{70}$$

Applying Ampere's law to equation (70) with the gauge (72) yields the following advection-diffusion equation for $\vec{A}$

$$\mu_0 \sigma(\partial_t \vec{A} + (\vec{v} \cdot \vec{\nabla})\vec{A}) = \vec{\nabla}^2 \vec{A}, \tag{71}$$

where μ_0 is the vacuum permeability.

In the case of a more complex flow profile where the velocity is non unifom this step would differ significantly. One cause of this is the term $(\vec{A} \cdot \nabla)\vec{v}$, which appears in the identity for $\vec{v} \times \vec{\nabla} \times \vec{A}$ is nonzero for nonuniform velocity. If this case was considered an analytic solution is unlikely be suitable and the flow inside the conductive layer would need to be solved numerically.

An equation analogous to equation (71) results also for $\vec{B}$ when curl is applied to equation (71). This will hold for all the equations derived in the following unless stated otherwise. For the derivation of equation (71) we have introduced the gauge

$$\vec{\nabla} \cdot \vec{A} + \mu_0 \sigma(\Phi - \vec{v} \cdot \vec{A}) = 0, \tag{72}$$

which defines the scalar potential in the conductor. In free space ($\sigma = 0$) the gauge reduces to Coulomb gauge $\vec{\nabla} \cdot \vec{A} = 0$.

In the following, external magnetic field is assumed to vary in time harmonically as $\vec{A}^e(\vec{r}, t) = \hat{\vec{A}}^e(\vec{r}) \cos(\omega t)$, and the solution is sought in the complex form $\vec{A}(\vec{r}, t) =$

$\Re\left[\vec{A}(\vec{r})e^{i\omega t}\right]$. Let us first consider a spatial amplitude distribution of the external magnetic field in the form of a single Fourier mode

$$\vec{A}(\vec{r}) = \vec{\hat{A}}(r)e^{i(kz+m\phi)}, \tag{73}$$

where (r, ϕ, z) are the cylindrical coordinates associated with geometry of the problem, and k and m are the axial and azimuthal wave numbers, respectively. The associated radial distribution of the magnetic field amplitude is

$$\vec{\hat{B}}(r) = \vec{e}_r i(mr^{-1}\hat{A}_z - k\hat{A}_\phi) + \vec{e}_\phi(ik\hat{A}_r - \hat{A}'_z) + \vec{e}_z\left(r^{-1}(r\hat{A}_\phi)' - imr^{-1}\hat{A}_r\right), \tag{74}$$

where the prime denotes a derivative with respect r.

Using R, $t_m = \mu_0\sigma R^2$ and $v_m = (\mu_0\sigma R)^{-1}$ as the length, time and velocity scales, equation (71) can be written in the following dimensionless form

$$\left[D_m - \kappa^2\right]\vec{\hat{A}} - r^{-2}\left[\vec{e}_r\hat{A}_r - \vec{e}_\phi\hat{A}_\phi + i2m(\vec{e}_r\hat{A}_\phi - \vec{e}_\phi\hat{A}_r)\right] = 0, \tag{75}$$

where $D_m \equiv \frac{d^2}{dr^2} + \frac{1}{r}\frac{d}{dr} - \left(\frac{m}{r}\right)^2$ and $\kappa^2 = k^2 + i(\bar{\omega} + kRm)$; $\bar{\omega} = \mu_0\sigma\omega R^2$ and $Rm = \mu_0\sigma vR$ are respectively the dimensionless frequency and velocity. The latter is also known as the magnetic Reynolds number. For the free-space region outside the cylinder, where $\sigma = 0$, we have equation (75) with $\kappa^2 = k^2$.

6.2 Boundary Conditions

Boundary conditions at the interface S between conducting and insulating regions follow from the continuity of the magnetic field and its vector potential

$$\left[\vec{\hat{B}}\right]_S = \left[\vec{\hat{A}}\right]_S = 0, \tag{76}$$

where $[]_S$ denotes the jump of the enclosed quantity across S. In addition, continuity of the magnetic field (74) requires

$$\left[\hat{A}'_\phi\right]_S = \left[\hat{A}'_z\right]_S = 0. \tag{77}$$

Thus the vector potential has two more boundary conditions than the magnetic field though both are governed by the same equation (74). This due to the different additional constraints imposed on each quantity which will be discussed later.

6.2.1 Boundary Conditions for Magnetic Vector Potential

The solution of equation (75) for non-axisymmetric modes ($m \neq 0$) is complicated by the coupling of radial and azimuthal components. This coupling is removed by the substitution

$$\hat{A}_{\pm} = \frac{1}{\sqrt{2}}(\hat{A}_r \pm i\hat{A}_\phi). \tag{78}$$

The radial and azimuthal components can be recovered from the decoupling variables $\hat{A}_{\pm}$ by

$$\hat{A}_r = \frac{1}{\sqrt{2}}(\hat{A}_- + \hat{A}_+), \tag{79}$$

$$\hat{A}_\phi = \frac{i}{\sqrt{2}}(\hat{A}_- - \hat{A}_+). \tag{80}$$

The substitution reduces equation (75) to

$$\left[D_{m\pm1} - \kappa^2\right]\hat{A}_{\pm} = 0, \tag{81}$$

$$\left[D_m - \kappa^2\right]\hat{A} = 0, \tag{82}$$

where $\hat{A} \equiv \hat{A}_z$ is used to simplify the notation. Then the general solution of equations (81,82) inside the cylinder ($r < 1$) can be written as

$$\hat{A}^i_{\pm}(r) = C^i_{\pm} I_{m\pm1}(\kappa r), \tag{83}$$

$$\hat{A}^i(r) = C^i I_m(\kappa r), \tag{84}$$

whereas in the free space between the cylinder and the coil generating the field ($1 \leq r < r_c$) we have

$$\hat{A}^o_{\pm}(r) = C^o_{\pm} K_{m\pm1}(kr) + C^e_{\pm} I_{m\pm1}(kr), \tag{85}$$

$$\hat{A}^o(r) = C^o K_m(kr) + C^e I_m(kr), \tag{86}$$

where $I_\nu(x)$ and $K_\nu(x)$ are the modified Bessel functions of the first and second kind with order ν [1], $C^e_{\pm}$ and C^e are supposed to be given constants defining the external magnetic, whilst $C^{i,o}_{\pm}$ and $C^{i,o}$ are unknown constants. A similar general solution can be written also for the magnetic field. Note that the solution obtained above is not applicable to $k = 0$ which needs to be considered separately.

It is also important to note that there are six unknown constants but only five boundary conditions (76, 77) for the vector potential. To determine the unknown constants we need to take into account that the vector potential in the free space has to satisfy not

only equation (81) but also Coulomb gauge $\vec{\nabla}\cdot\vec{A}=0$, which can be written as

$$\left(r(\hat{A}^o_+ + \hat{A}^o_-)\right)' + im(\hat{A}^o_+ - \hat{A}^o_-) + i2kr\hat{A}^o = 0. \tag{87}$$

First of all, this constraint has to be satisfied by the external magnetic field itself, which results in

$$C^e_+ + C^e_- = -i2C^e. \tag{88}$$

Assuming this to be the case, we obtain from equation (87)

$$C^o_+ + C^o_- = \quad i2C^o, \tag{89}$$

which is the required additional constraint on the unknown coefficients.

The unknown coefficients $C^{i,o}$, which define the z-component of vector potential, can be determined independently from the rest. For this component, boundary conditions (76,77) take the form

$$\begin{aligned} C^i I_m(\kappa) - C^o K_m(k) &= C^e I_m(k), & (90)\\ C^i \kappa I'_m(\kappa) - C^o k K'_m(k) &= C^e k I'_m(k), & (91) \end{aligned}$$

and yield

$$\begin{aligned} C^i &= \tilde{C}^e(kI'_m(k)K_m(k) - kK'_m(k)I_m(k)), & (92)\\ C^o &= -\tilde{C}^e(\kappa I'(\kappa)I_m(k) - kI'_m(k)I_m(\kappa)), & (93) \end{aligned}$$

where $\tilde{C}^e = C^e/\left(\kappa I'_m(\kappa)K_m(k) - kK'_m(k)I_m(\kappa)\right)$; $I'_m(x) = \left(I_{m-1}(x) + I_{m+1}(x)\right)/2$ and $K'_m(x) = -\left(K_{m-1}(x) + K_{m+1}(x)\right)/2$ [1]. For the remaining four unknown constants $C^{i,o}_\pm$, we have a system of four linear equations. The first equation is the gauge condition (89). Two more equations, one for the plus and another for the minus sign in the index, follow from boundary condition (76)

$$C^i_\pm I_{m\pm1}(\kappa) - C^o_\pm K_{m\pm1}(k) = C^e_\pm I_{m\pm1}(k). \tag{94}$$

The boundary condition (77) for the azimuthal components yields the fourth equation

$$\begin{aligned} &\kappa\left(C^i_+ I'_{m+1}(\kappa) - C^i_- I'_{m-1}(\kappa)\right)\\ &-k\left(C^o_+ K'(k) + C^o_- K'_{m-1}(k)\right) = k\left(C^e_+ I'(k) - C^e_- I'(k)\right), \end{aligned} \tag{95}$$

which after some algebra can be written as

$$(C^i_+ - C^i_-)\kappa I_m(\kappa) + (C^o_+ - C^o_-)kK_m(k) = (C^e_+ - C^e_-)kI_m(k). \tag{96}$$

The solution of these four linear complex equations is straightforward but too lengthy to be written explicitly. Alternatively, equations (77, 94, 96) can easily be solved numerically using, for example, the complex LU factorisation routines from the LAPACK software package or their MATLAB implementation.

For the solution to be useful, we need to consider also the special case of $k = 0$, which appears in the Fourier series representation of the general field distribution derived later. For $k = 0$, the Bessel functions, which are particular solutions of equations (81,82), reduce as follows $I_m(kr) \to r^{|m|}$, $K_m(kr) \to r^{-|m|}$ for $m \neq 0$ and $K_0(kr) \to \ln r$, where the last case of $m = 0$ is practically irrelevant as discussed later. Firstly, as a result of these substitutions Coulomb gauge (87) reduces to

$$C_+^e = C_-^o = 0, \quad m > 0; \tag{97}$$

$$C_-^e = C_+^o = 0, \quad m < 0; \tag{98}$$

$$C_+^e + C_-^e = 0, \quad m = 0. \tag{99}$$

Note that equation (99) does not constrain coefficients $C_\pm^o$, which means that the induced vector potential outside the cylinder for mode $k = m = 0$ satisfies Coulomb gauge automatically. These coefficients describe radial and azimuthal components of vector potential which vary as $\sim r^{-1}$. It means that the respective vector potential is purely irrotational and, thus, not associated with any physical magnetic field. On the other hand, according to equations (79) and (99), external vector potential for this mode can have only the azimuthal component. It means that we may assume the induced vector potential to be purely azimuthal as well, which corresponds to

$$C_+^{i,o} + C_-^{i,o} = 0.$$

This condition can be interpreted also as a gauge which removes the irrotational radial component of the induced vector potential for mode $k = m = 0$. By the same argument one can set $C^e = 0$ for this mode, which removes irrotational axial component of the external vector potential, and owing to equations (92,93) the respective induced field as well. This condition as well as equations (97,98) cancel the terms of the induced vector potential varying as $\sim \ln r$. It means that we can ignore this special case and use the following substitutions $I_m(k) \to 1$, $K_m(k) \to 1$, $kI'_m(k) \to |m|$ and $kK'_m(k) \to -|m|$ in equations (92, 93,94,95) when $k = 0$. The same holds also for $\kappa = 0$ which occurs when $k = \bar{\omega} = 0$.

6.2.2 Boundary Conditions for The Magnetic Field $\vec{B}$

Now let us turn to the solution for the magnetic field $\vec{\hat{B}}$ which can be written in the same form as equations (83–86) for $\vec{\hat{A}}$. In this case, we use D instead of C to denote the

six unknown coefficients. We have the same number of unknown coefficients as for the vector potential, but only three boundary conditions (76) which require the continuity of the magnetic field across the interface and lead to the equations analogue to equations (90,94) for the vector potential. In contrast to the vector potential, the magnetic field has to be solenoidal not only outside the cylinder but in also inside it, which leads to two more equations

$$D^o_+ + D^o_- = i2D^o, \tag{100}$$

$$\kappa(D^i_+ + D^i_-) = -i2kD^i, \tag{101}$$

and a constraint on the external magnetic field analogous to equation (88). The the last required equation follows from the irrotationality of the magnetic field in the free space

$$D^o_+ = D^o_-. \tag{102}$$

The same constraint applies also to the external magnetic field.

Instead of solving for the magnetic field directly using the equations obtained above, one can solve for the vector potential and then use this solution to find find the magnetic field, if required. Therefore, we need to express the coefficients defining magnetic field in the terms of those defining the vector potential. This can be done using and expression (74), which yields

$$\hat{B}_\pm = i(mr^{-1}\hat{A} \mp \hat{A}' \pm ik\hat{A}_\pm), \tag{103}$$

$$\hat{B} = -i((\hat{A}_+ - \hat{A}_-)' + r^{-1}((m+1)\hat{A}_+ + (m-1)\hat{A}_-))/2 \tag{104}$$

Using the basic properties of of Bessel functions, after some algebra we obtain

$$D^i_\pm = \mp(kC^i_\pm + i\kappa C^i), \tag{105}$$

$$D^o_\pm = \mp k(C^o_\pm - iC^o), \tag{106}$$

$$D^i = -i\kappa(C^i_+ - C^i_-)/2, \tag{107}$$

$$D^o = ik(C^o_+ - C^o_-)/2, \tag{108}$$

which hold for $k \neq 0$ and and $\kappa \neq 0$. It can be easily verified that the relations above indeed satisfy the solenoidality and irrotationality constraints defined by equations (100–101). For $k = 0$, using the same approach as before, we find from equations

(103,104)

$$D^o = -i(m-1)C^o_-,\ D^o_+ = i2mC^o,\ D^o_- = 0, m \geq 0;$$
$$D^o = -i(m+1)C^o_+,\ D^o_- = i2mC^o,\ D^o_+ = 0, m < 0;$$
$$D^o = D^o_\pm = 0, m = 0.$$

For $\kappa \neq 0$, the coefficients $D^i_\pm$and D^i remain defined by equations (105,107), but for $\kappa = k = 0$ reduce to

$$D^i = -i(m+1)C^i_+,\ D^i_- = i2mC^i,\ D^i_+ = 0, m \geq 0;$$
$$D^i = -i(m-1)C^i_-,\ D^i_+ = i2mC^i,\ D^i_+ = 0, m < 0;$$
$$D^i = -i(C^i_+ - C^i_-),\ D^i_\pm = 0, m = 0.$$

6.2.3 A comment on the current at the boundary

We now consider the condition for the normal component of current j_n at the boundary. As the current cannot travel in free space, where $\sigma = 0$, the normal component of current must vanish at the boundary: $j_n = 0$. This is an implicit boundary condition which is satisfied automatically owing to the conditions obeyed by the magnetic vector potential. According to Ampere's law $\mu_0 \vec{j} = \vec{\nabla} \times \vec{B}$, the absence of electric current outside conducting medium, $\vec{\nabla} \times \vec{\nabla} \times \vec{A} = \vec{\nabla}\vec{\nabla} \cdot \vec{A} - \vec{\nabla}^2 \vec{A} = 0$, is ensured by the Coulomb gauge and the Laplace's equation, which are both satisfied by $\vec{A}$ in the free space. Consequently, the vanishing of j_n at the boundary depends on the continuity of $\vec{n} \cdot \vec{\nabla} \times \vec{B}$ across the boundary. This is ensured by the continuity of tangential components of $\vec{B}$ across the boundary, which, in turn, follows from the continuty of $\vec{A}$ and the normal derivatives of its tangental components. Note that only $\partial_n A_n$ can be discontinious accros the boundary but it affects only the continuity of B_r but not that of B_ϕ or B_z.

6.3 The Applied Field

Now let us consider a general external 3D magnetic field and represent its vector potential by a double Fourier series in axial and azimuthal directions

$$\vec{A}^e(\vec{r}) = \sum_{(m,n)=-(M,N)}^{(M,N)} \vec{\hat{A}}^e_{n,m}(r) e^{i(k_n z + m\phi)},$$

where $k_n = nk$ and k is the fundamental wave number. According to solution (85, 86), the amplitude distribution of each Fourier mode in a cylindrical region enclosing the

symmetry axis but not the coil generating the field can be written as

$$\vec{\hat{A}}^e_{n,m}(r) = \vec{e}_+ C^e_{+;m,n} I_{m+1}(k_n r) + \vec{e}_- C^e_{-;m,n} I_{m-1}(k_n r) + \vec{e}_z C^e_{m,n} I_m(k_n r),$$

where $\vec{e}_\pm = \frac{1}{\sqrt{2}}(\vec{e}_r \pm i\vec{e}_\phi)$ and $C^e_{\pm;m,n}$ and $C^e_{m,n}$ are the coefficients which need to be determined for a given $\vec{A}^e(\vec{r})$. This is done numerically by first computing $\vec{A}^e(\vec{r})$ at discrete points $\vec{r}_{m,n}$ formed by the nodes of a uniform rectangular grid $(\phi_m; z_n) = (m\pi/M, -M \leq m < M; nL/N, -N \leq n < N)$ covering the surface of cylinder $r = 1$ in the $-L \leq z < L$, where L is an axial cut-off length.

6.3.1 Field generated by an arbitrary coil

To generate the free space field produced by an arbitrary coil on the grid above the coil is represented by a series of straight wire sections. The wire sections must form a closed loop. The field generated by the coil can be approximated by the sum of fields generated by these discrete wire sections. The field generated by a finite current is given by

$$\vec{A}(\vec{r}) = \frac{\mu_0 I_0}{4\pi} \int_L \frac{d\vec{r}'}{|\vec{r} - \vec{r}'|}$$

Specifying a set of wire elements W with straight individual elements w with a finite lengths L_w. The current in each wire element is given by $\vec{j} = \vec{e}_w I_0$ where $\vec{e}_w$ is a unit vector in the direction of the wire element and I_0 is the current in the loop. The equation for the field generated by a single finite wire element is given by

$$A_w(r, z) = \frac{\mu_0 I_0}{4\pi} \int_{-L_w/2}^{L_w/2} \frac{1}{|r\vec{e_r} + z\vec{e_z} - \vec{e_z} z'|} dz'.$$

with the solution, in the frame of reference of the wire element, given as:

$$A_w(r_w, z_w) = \vec{e}_w \frac{\mu_0 I_0}{2\pi r_w} \ln \frac{\sqrt{r_w^2 + (\frac{L}{2} - z_w)^2} + (\frac{L}{2} - z_w)}{\sqrt{r_w^2 + (\frac{L}{2} + z_w)^2} - (\frac{L}{2} + z_w)}$$

where r_w and z_w are radial and axial positions from the wire element. After transforming to a single cartesian frame of reference by applying the following transforms of $r_w \to r$ and $z_w \to z$ to the above equation

$$z = \vec{e}_w \cdot \vec{D}$$

$$r = \sqrt{\vec{D} \cdot \vec{D} - z^2}$$

where $\vec{D} = \vec{r} - \vec{r_w}$. An approximation of the field generated by an arbitrary coil can be given as the sum of all its individual elements

$$\vec{A}^e(\vec{r}) = \sum_{w}^{W} \vec{A}_w(r, z).$$

This can be simply extended to multiple coils by incorporating all of their elements into W and their currents into I_0.

6.4 Results

The 3D model described in section has been developed as a tool to support further research, as such in this work its usage is presented as a proof of concept and will not contain novel results.

6.4.1 Comparison To Axisymmetric Model

For validation we will now compare the results of this 3D model with axisymmetric analytic model presented in chapter 5. For this comparison a single axisymmetric coil of radius $r_c = 2$ placed at $z_c = 0$ will be used. In the 3D model this coil is represented by 90 wire segments. In the comparison both models use 1024 points in z, 128 points in ϕ and 100 points in r. Figure 27 shows that the ϕ component of the vector potential for both models are equal for various magnetic Reynolds numbers and dimensionless frequencies. Note that the imaginary component gives the field out of phase with the applied field which gives the induced field. The imaginary components are omitted for dimensionless frequency $\bar{\omega} = 0$, corresponding to a conductivity of $\sigma = 0$, because they are identically zero in the absence of a conducting medium. The results are presented in a cartesian coordinate system (x, y, z) with the positive x-axis oriented along $\phi = 0$. The fields are transformed to cartesian $F(r, \phi, z) \rightarrow F(x, y, z)$ by the following transformations:

$$F(x, y, z) = \begin{bmatrix} \vec{e}_x \\ \vec{e}_y \\ \vec{e}_z \end{bmatrix} \cdot \begin{bmatrix} \vec{e_r} F(r, \phi, z)\cos(\phi) - \vec{e_\phi} F(r, \phi, z)\sin(\phi) \\ \vec{e_r} F(r, \phi, z)\sin(\phi) + \vec{e_{phi}} F(r, \phi, z)\cos(\phi) \\ \vec{e_z} F(r, \phi, z) \end{bmatrix}$$

Figure 28 shows the magnetic flux lines for the applied and induced field for the axisymmetric coil above. The figures were generated using ParaView software. Note the dual symmetry in the theta plane and the $z = 0$ plane.

The isolines of the y-component vector potential for the axisymmetric coil are shown in the $y = 0$ plane in figure 29. The vector potential is antisymmetric about $x = 0$ which corresponds to symmetry between $\phi = 0$ and $\phi = \pi$ as is required by the axisymmetric coil. With $Rm = 0$ the vector potential is symmetric across $z = 0$ which is expected

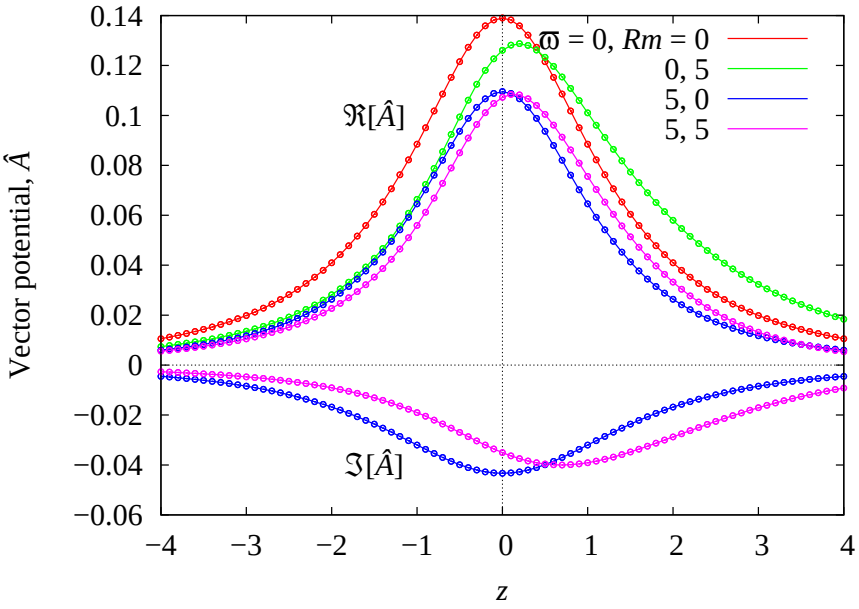

Figure 27: Axial distribution of the azimuthal component of vector potential induced at the cylinder surface ($r = 1$) by a co-axial circular current loop of radius $r_c = 2$ placed at $z_c = 0$ for various dimensionless frequencies $\bar{\omega}$ and magnetic Reynolds numbers Rm. The solid lines were computed using an axisymmetric analytical model and dots 3D model.

for this coil. This symmetry is broken when the cylinder is in motion $Rm \neq 0$. The continuity of the vector potential $\hat{A}_y$ and its derivatives $\partial_x \hat{A}_y$ and $\partial_z \hat{A}_y$ can be seen at the pipe wall ($x = \pm 1$), which is required by the boundary conditions (76,77).

The isolines of the x-component of the magnetic field ($\hat{B}_x$) in the $y = 0$ plane are shown in figure 30. Note that the single azimuthal component present in $\vec{A}$ leads to two components, r and z, in $\vec{B}$ as is expected from $\vec{B} = \vec{\nabla} \times \vec{A}$. The continuity of $\hat{B}_x$ and its derivative $\partial_x \hat{B}_x$ at the pipe wall can also be seen in figure 30. The x-component is shown to be antisymmetric about the x-axis, which again corresponds to symmetry in ϕ. Again with $Rm = 0$ the field is symmetric across $z = 0$, and this symmetry is broken by the motion of the cylinder.

Figure 31 shows the isolines of the z-component the magnetic field $\hat{B}_z$ in the $y = 0$ plane. The symmetry across $z = 0$ is also present in $\hat{B}_z$ for $Rm = 0$. The continuity $\hat{B}_z$ at the pipe walls is required for the value but not for the derivatives. With $Rm = 0$, the z-component of the applied field, shown by the real component in figure 31 appears smooth. However as $\omega \neq 0$ this is not the case as the induced field shown by the imaginary component is also present, but cannot be seen as it is dominated by the applied field.

6.4.2 A Non-Axisymmetric Example

To demonstrate the ability of this model to go beyond the the models presented in chapters 4 and 5, a coil which requires resolving in 3D is presented. The coil is of radius

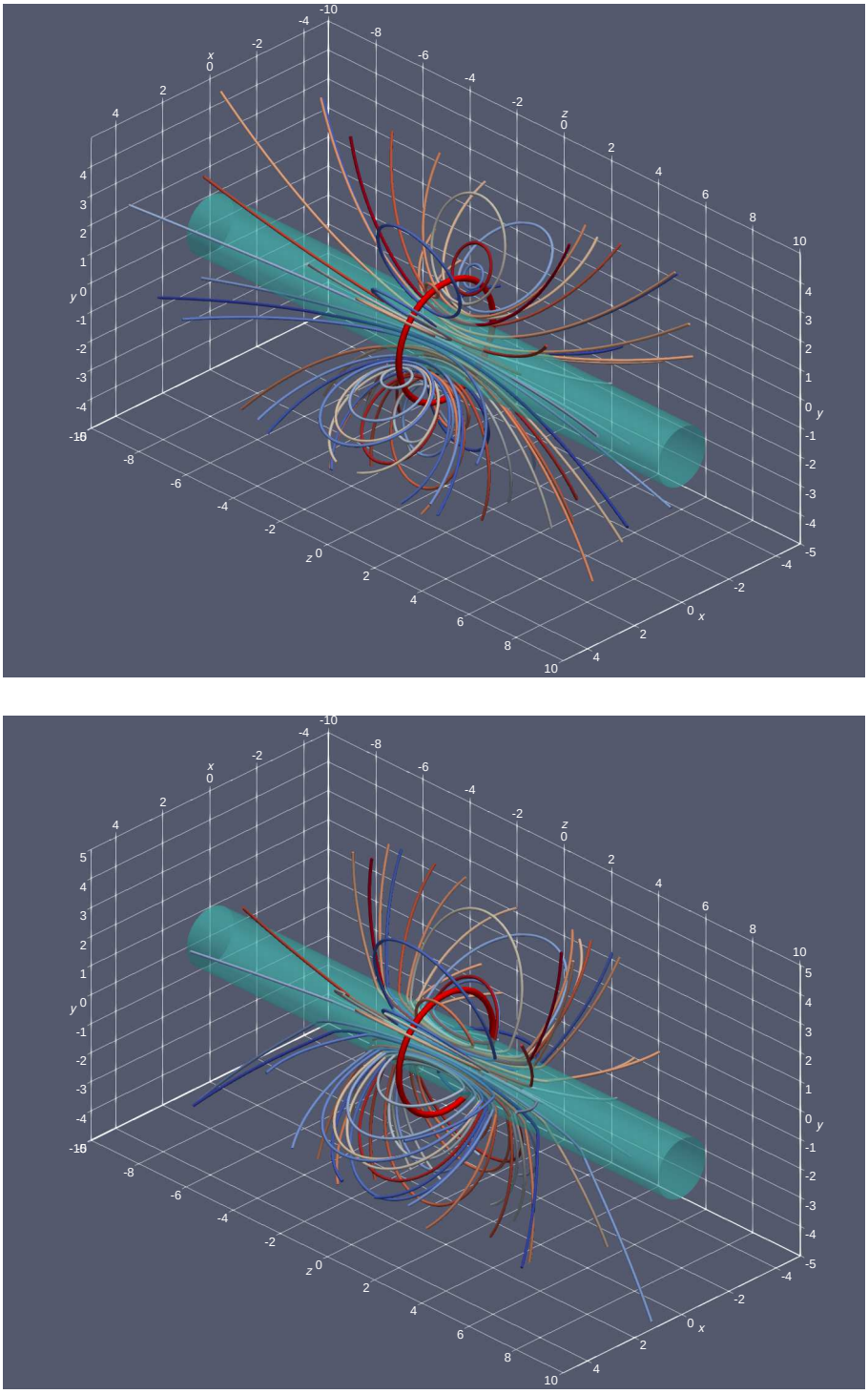

Figure 28: Real (left) and imaginary (right) parts of the magnetic flux lines for $\bar{\omega} = 1$ and $Rm = 1$ induced by a circular current loop of radius $r_c = 2$ placed coaxially at $z_c = 0$.

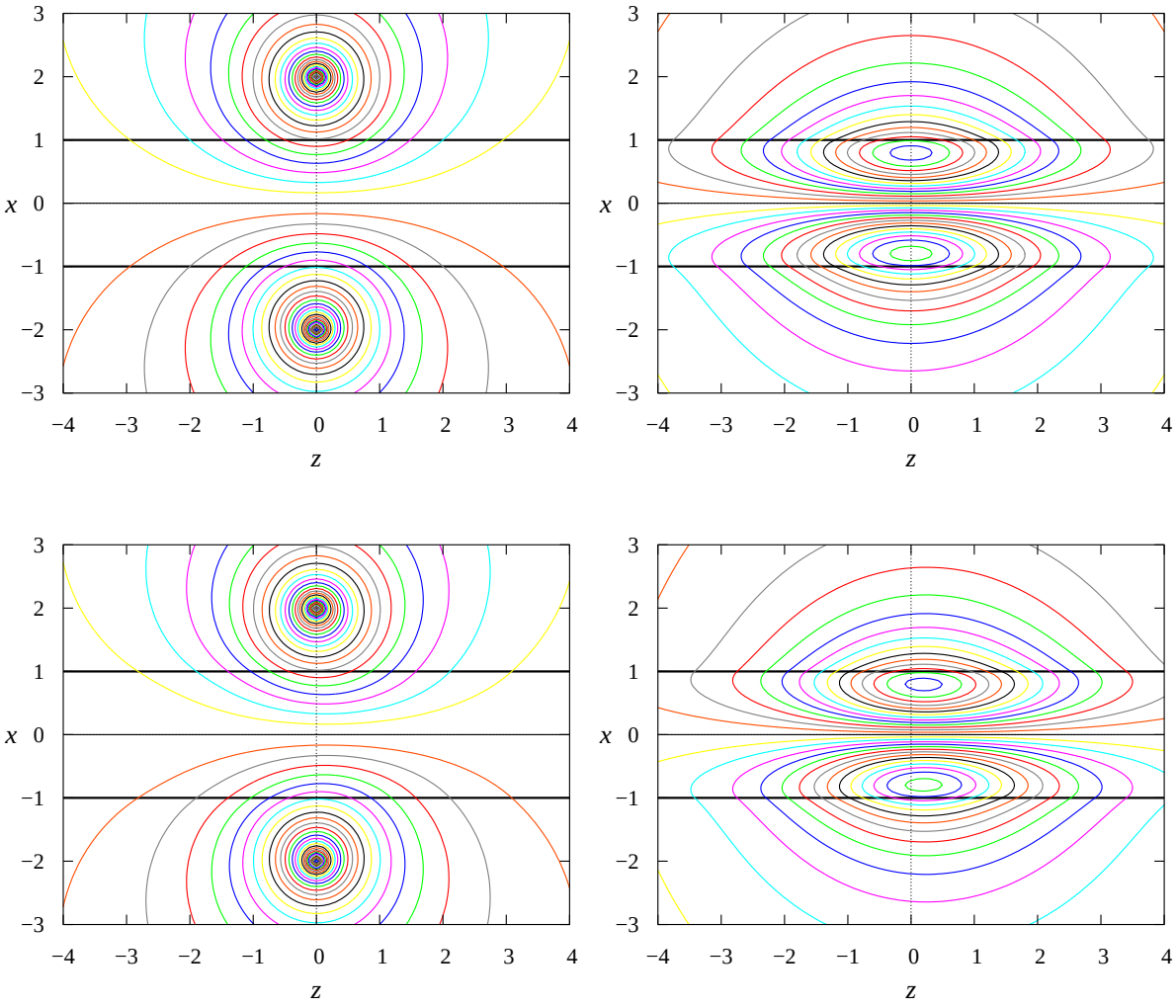

Figure 29: Isolines of the real (left) and imaginary (right) parts of $\hat{A}_y$ in the $y = 0$ plane for $\bar{\omega} = 1$, $Rm = 0$ (top) and $Rm = 1$ (bottom) induced by a circular current loop of radius $r_c = 2$ placed coaxially at $z_c = 0$.

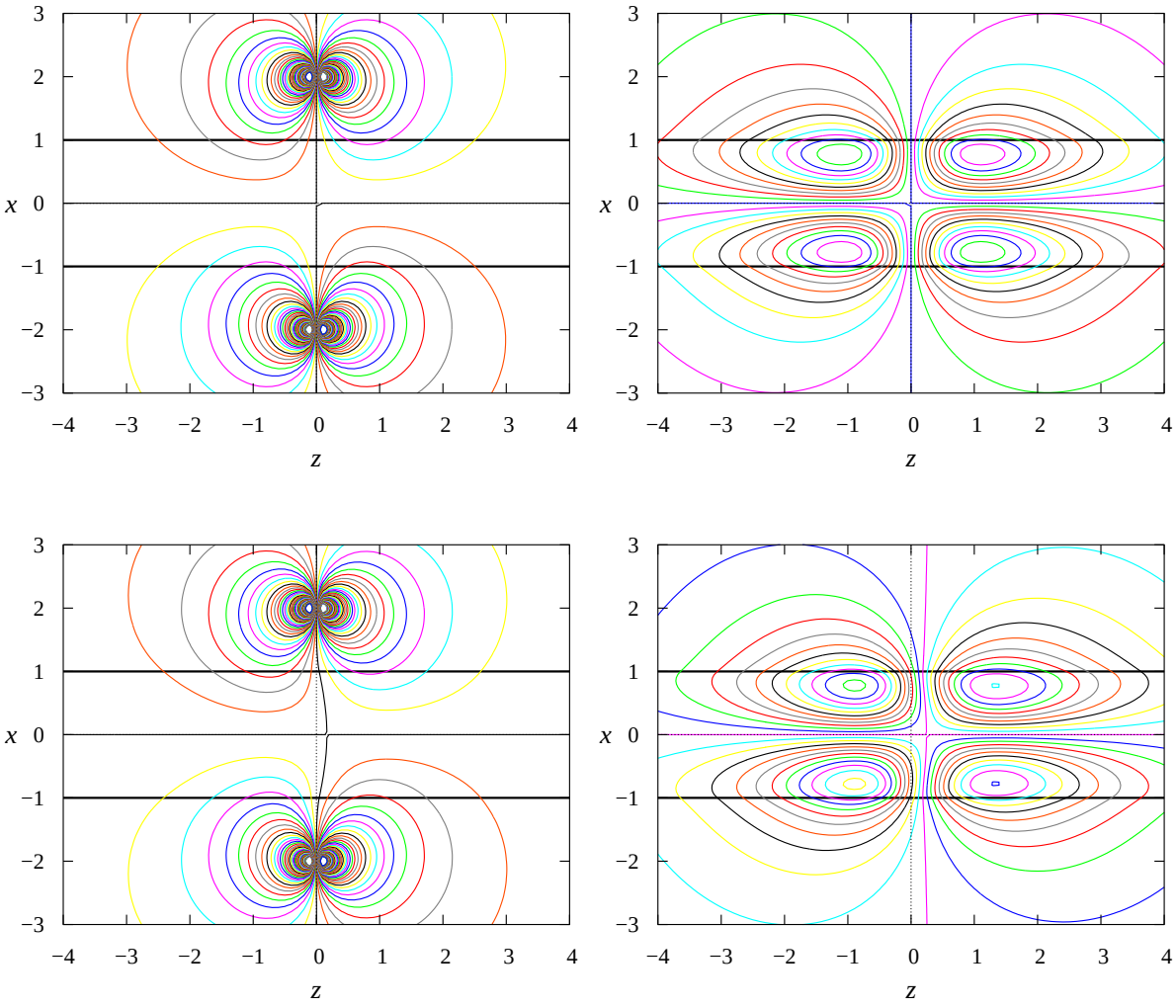

Figure 30: Isolines of the real (top) and imaginary (bottom) parts of $\hat{B}_x$ in the $y = 0$ plane for $\bar{\omega} = 1$, $Rm = 0$ (left) and $Rm = 1$ (right) induced by a circular current loop of radius $r_c = 2$ placed coaxially at $z_c = 0$.

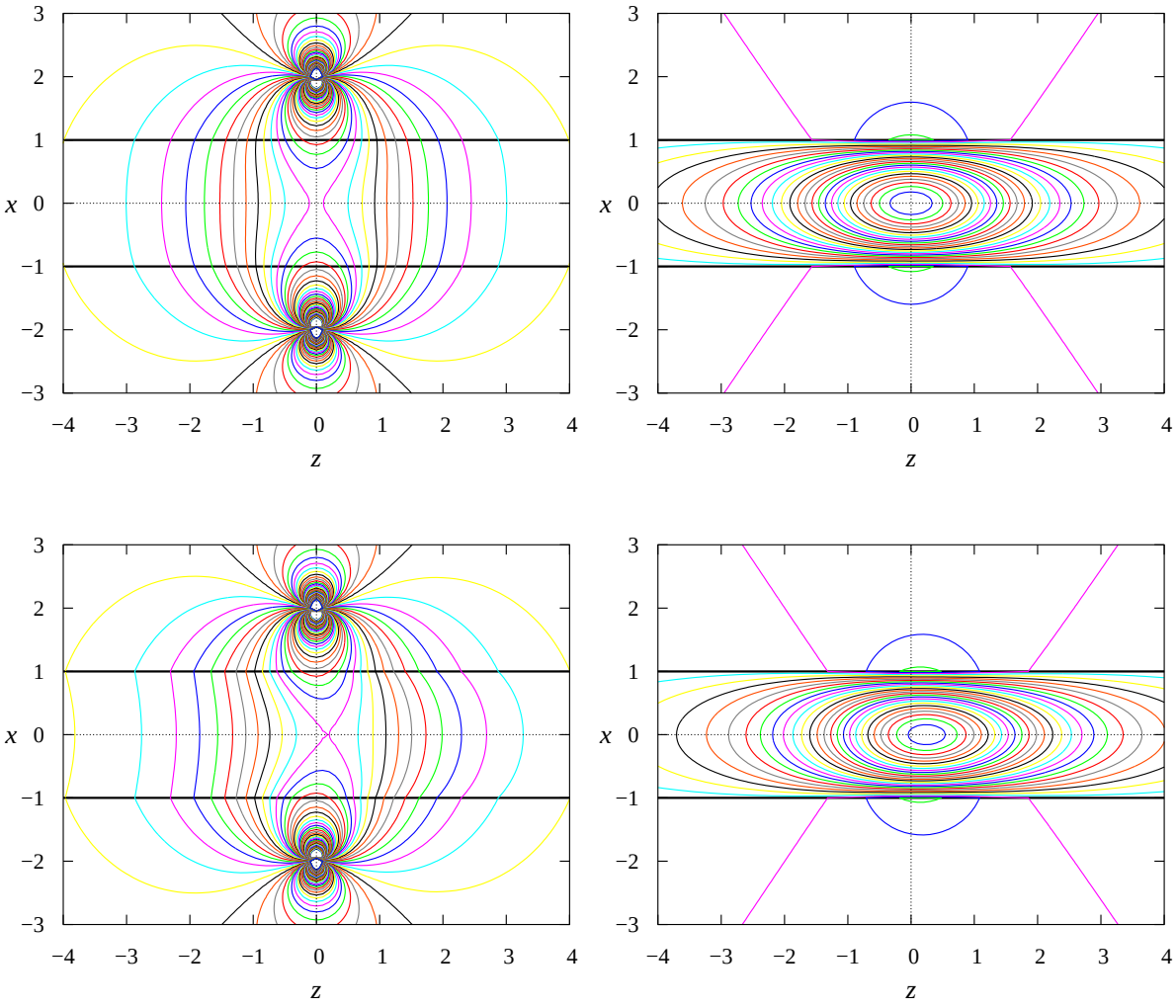

Figure 31: Isolines of the real (top) and imaginary (bottom) parts of $\hat{B}_z$ in the $y = 0$ plane for $\bar{\omega} = 1$, $Rm = 0$ (left) and $Rm = 1$ (right) induced by a circular current loop of radius $r_c = 2$ placed coaxially at $z_c = 0$.

$r_c = 2$ placed in the $x = 2$ plane centred at $(y_c = 0, z_c = 0)$. The magnetic flux lines for this coil are shown in figure 32 for the applied and induced magnetic fields.

The vector potential in the $y = 0$ plane is shown in figure 33. The antisymmetry in z in the coil in this plane leads to the antisymmetric vector potential for $Rm = 0$. This symmetry is seen to be broken when $Rm \neq 0$. The continuity of $\hat{A}_y$ and its derivative $\partial_x \hat{A}_y$ can be seen at the pipe wall ($x = \pm 1$), which as before is required by the boundary conditions (76,77).

Isolines of the components of the vector potential in the $x = 0$ plane for coil centred at $(y_c = 0, z_c = 0)$ in the $x = 2$ plane are given in figure 34 for $Rm = 0$ and in figure 35 with $Rm = 1$. Symmetry about $z = 0$ for $Rm = 0$ can be seen in $\hat{A}_z$ whereas $\hat{A}_x$ and $\hat{A}_y$ are antisymmetric about $z = 0$. These three symmetries cease to exist when the cylinder is in motion $Rm \neq 0$. Similarly about the y-axis the $\hat{A}_x$ and $\hat{A}_z$ components are antisymmetric and the $\hat{A}_y$ component is symmetric. These symmetries are unaffected by the flow which is also symmetric about this axis. These symmetries are equivalent to the symmetries in the coil with the anti symmetries caused by the opposite currents found at opposite sides of the coil.

The x-axis is normal to the figures plane and thus $\hat{A}_x$ is equivalent to $\hat{A}_\phi$ in this plane. The continuity of the values of $\hat{A}_x$, $\hat{A}_y$ and $\hat{A}_z$ which is required by the boundary conditions can be seen. The derivatives $\partial_y \hat{A}_x$ and $\partial_y \hat{A}_z$ are also smooth, as required. In contrast the derivatives of $\hat{A}_y$, which is equivalent to $\hat{A}_r$ in this plane, are not required to be smooth across the cylinder wall. These continuities hold for both the cylinder in motion and at rest.

We will now look at the magnetic field produced by the same coil. As before in the axisymmetric example in the $y = 0$ slice where there is a single non-zero component of $\vec{A}$ the definition of the vector potential $\vec{B} = \vec{\nabla} \times \vec{A}$ leads to the remaining components being non-zero in $\vec{B}$. The non-zero components of $\vec{B}$ in the $y = 0$ plane are shown in figure 36 with $Rm = 0$ and figure 37 with $Rm = 1$. The continuity of $\hat{B}_x$ and its normal (x) derivative at the boundary is maintained. Only the value of $\hat{B}_z$ is required to be continuous, as can be seen its derivatives are not smooth at the boundary.

The magnetic field components in the $x = 0$ plane generated by the coil above, in phase and out of phase with the applied field, for a stationary cylinder and cylinder in motion are shown in figures 38 and 39, respectively. We can see that the component normal to the plane, $\hat{B}_y$, is the only component for which the derivative across the boundary is smooth. This is because it is defined by the tangential derivatives of tangential components of $\vec{A}$, which are continuous across the interface The other components of $\vec{B}$ are dependent on the $\hat{A}_r$ component which has been shown to not be smooth in this plane. We can see the expected symmetries in the y axis with $\hat{B}_x$ being symmetric and $\hat{B}_y$ and $\hat{B}_z$ being antisymmetric. The symmetries in the z axis, symmetric for $\hat{B}_x$ and $\hat{B}_y$ but antisymmetric for $\hat{B}_z$, are again broken by $Rm \neq 0$.

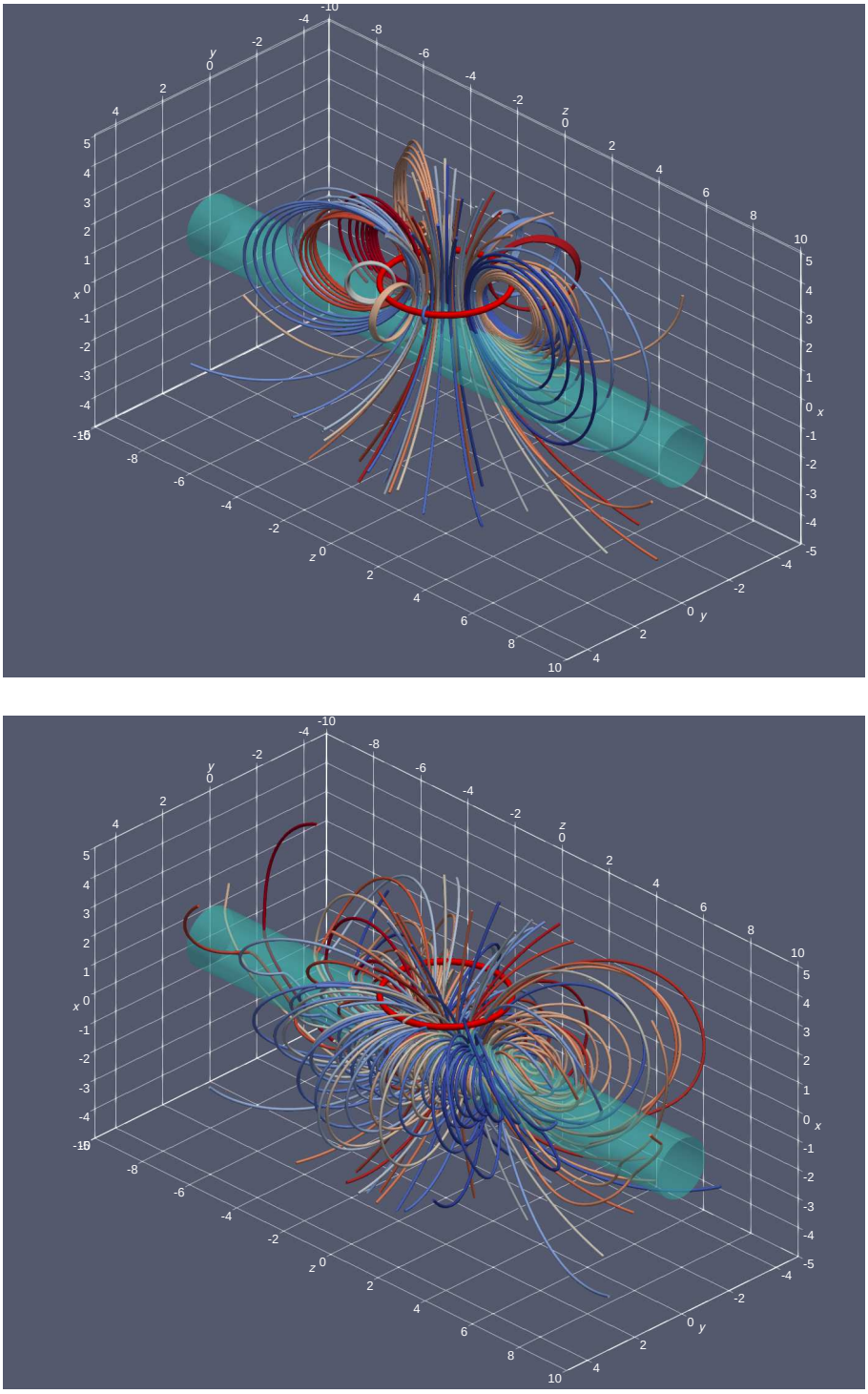

Figure 32: Real (left) and imaginary (right) parts of the magnetic flux lines for $\bar{\omega} = 1$ and $Rm = 1$ induced by a circular current loop of radius $r_c = 2$ placed parallel to the (y, z)-plane at $\vec{x}_c = (2, 0, 0)$.

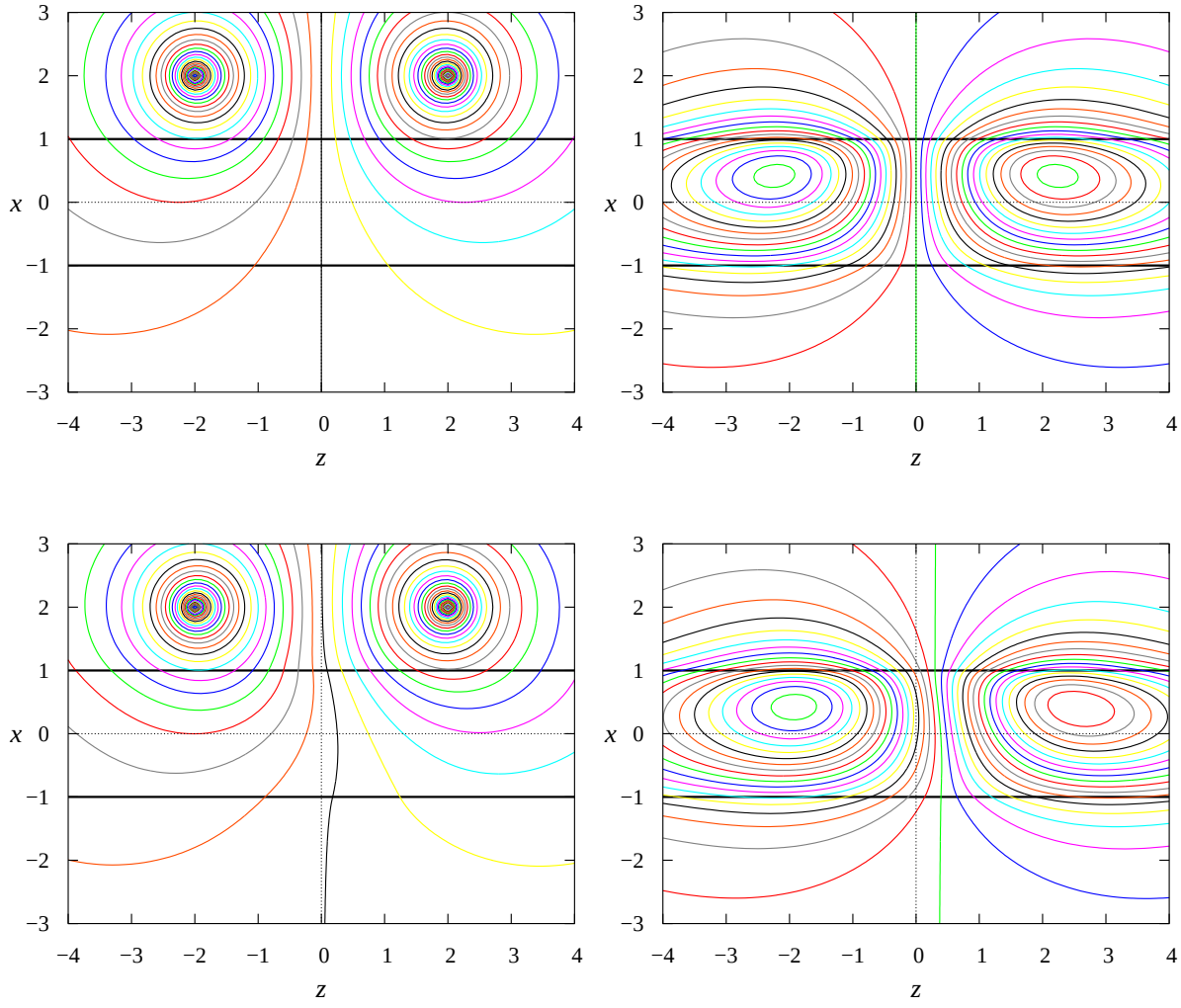

Figure 33: Isolines of the real (left) and imaginary (right) parts of $\hat{A}_y$ in the $y = 0$ plane for $\bar{\omega} = 1$ and $Rm = 0$ (top) and $Rm = 1$ (bottom) induced by a circular current loop of radius $r_c = 2$ placed parallel to the (y, z)-plane at $\vec{x}_c = (2, 0, 0)$.

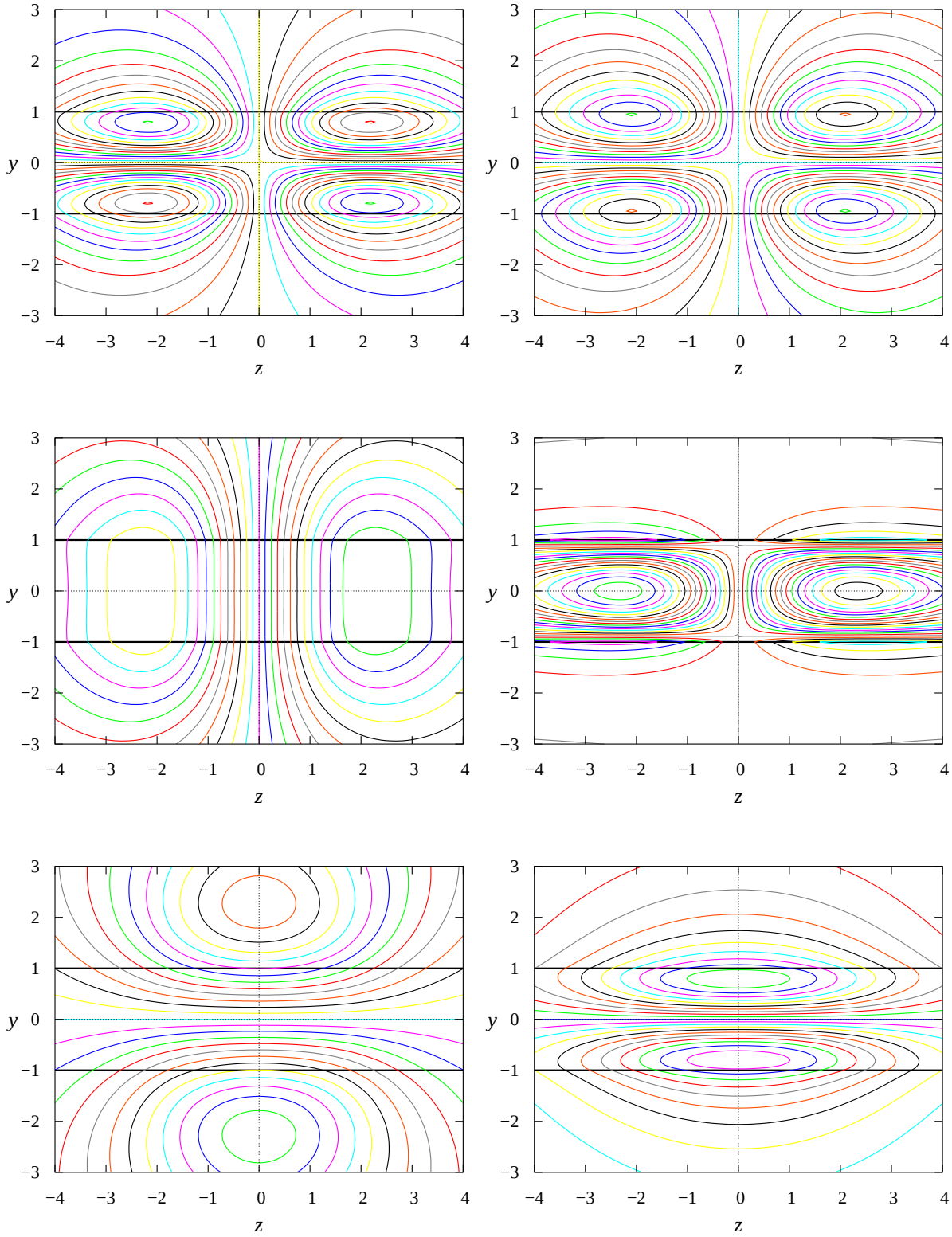

Figure 34: Isolines of the real (left) and imaginary (right) parts of $\hat{A}_x$ (top), $\hat{A}_y$ (middle) and $\hat{A}_z$ (bottom) in the $x = 0$ plane for $\bar{\omega} = 1$ and $Rm = 0$ induced by a circular current loop of radius $r_c = 2$ placed parallel to the (y, z)-plane at $\vec{x}_c = (2, 0, 0)$.

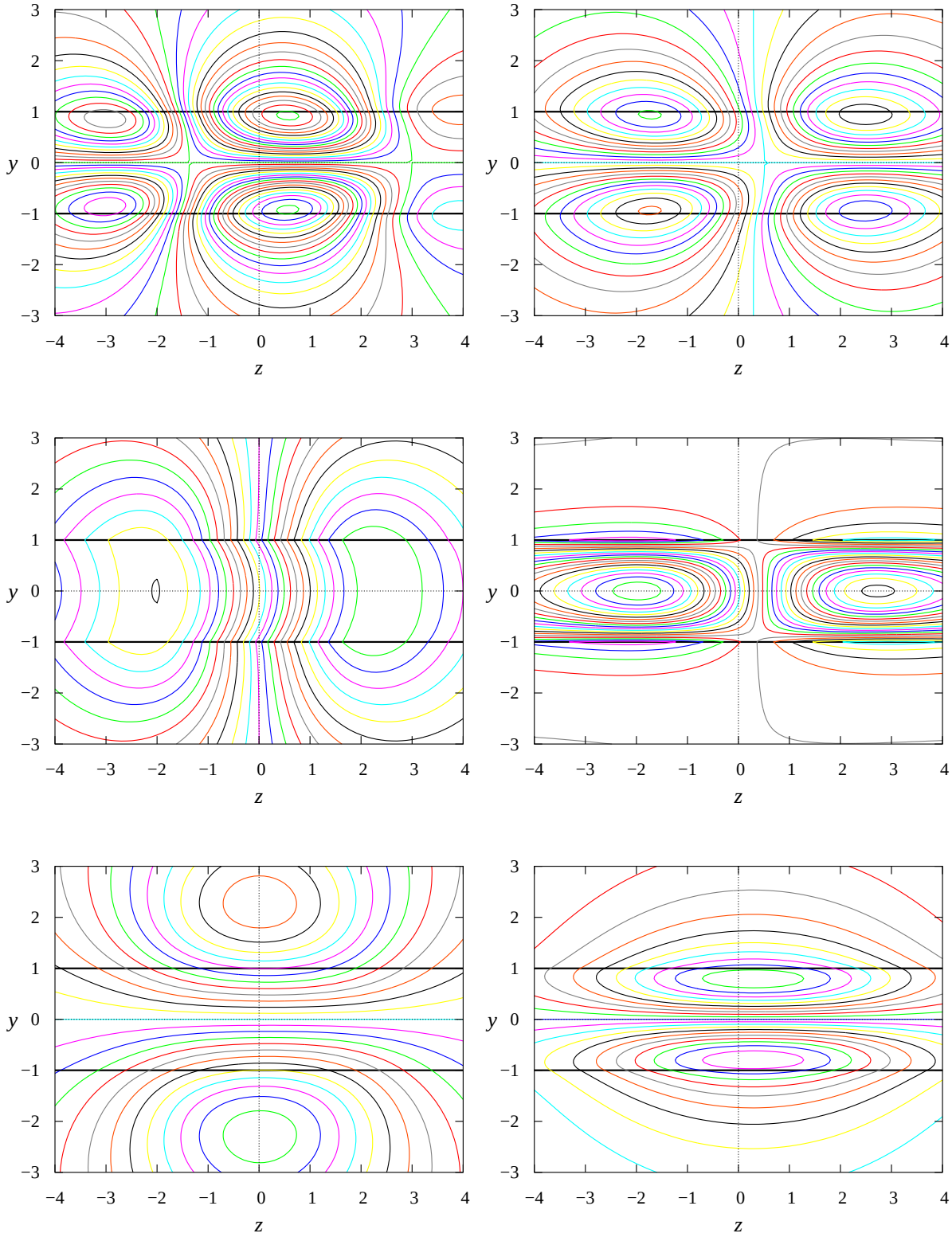

Figure 35: Isolines of the real (left) and imaginary (right) parts of $\hat{A}_x$ (top), $\hat{A}_y$ (middle) and $\hat{A}_z$ (bottom) in the $x = 0$ plane for $\bar{\omega} = 1$ and $Rm = 1$ induced by a circular current loop of radius $r_c = 2$ placed parallel to the (y, z)-plane at $\vec{x}_c = (2, 0, 0)$.

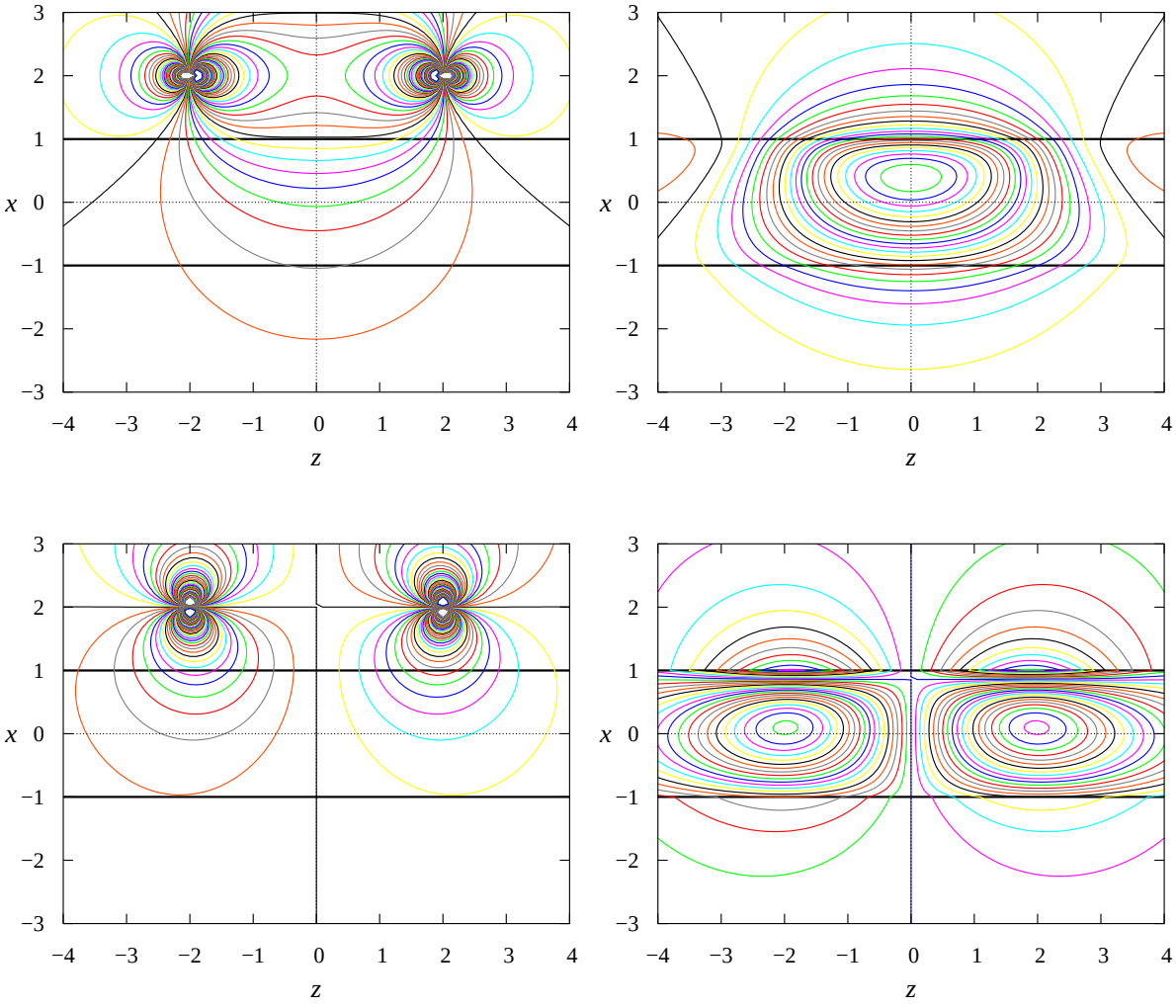

Figure 36: Isolines of the real (left) and imaginary (right) parts of $\hat{B}_x$ (top) and $\hat{B}_z$ (bottom) in the $y = 0$ plane for $\bar{\omega} = 1$ and $Rm = 0$ induced by a circular current loop of radius $r_c = 2$ placed parallel to the (y, z)-plane at $\vec{x}_c = (2, 0, 0)$.

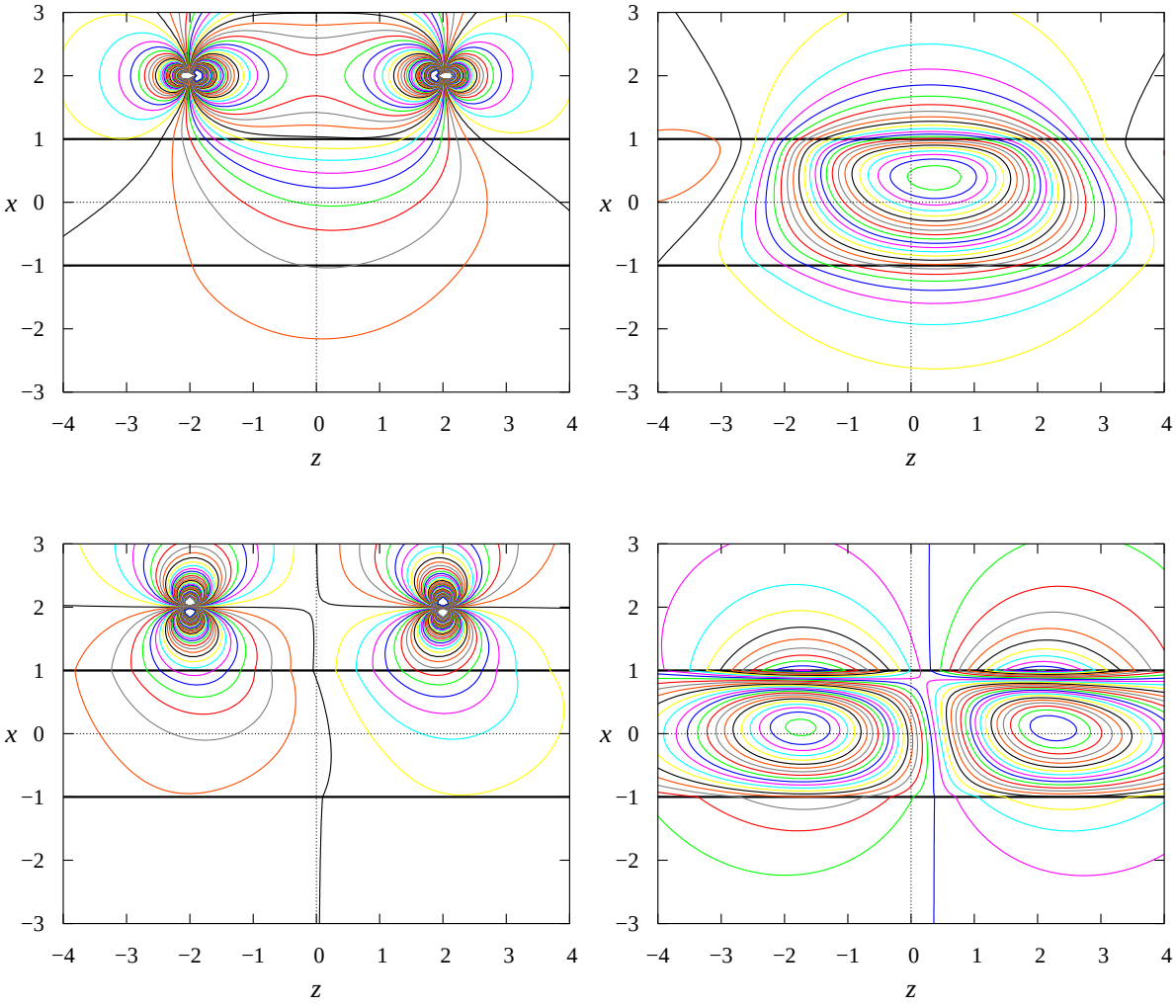

Figure 37: Isolines of the real (left) and imaginary (right) parts of $\hat{B}_x$ (top) and $\hat{B}_z$ (bottom) in the $y = 0$ plane for $\bar{\omega} = 1$ and $Rm = 1$ induced by a circular current loop of radius $r_c = 2$ placed parallel to the (y, z)-plane at $\vec{x}_c = (2, 0, 0)$.

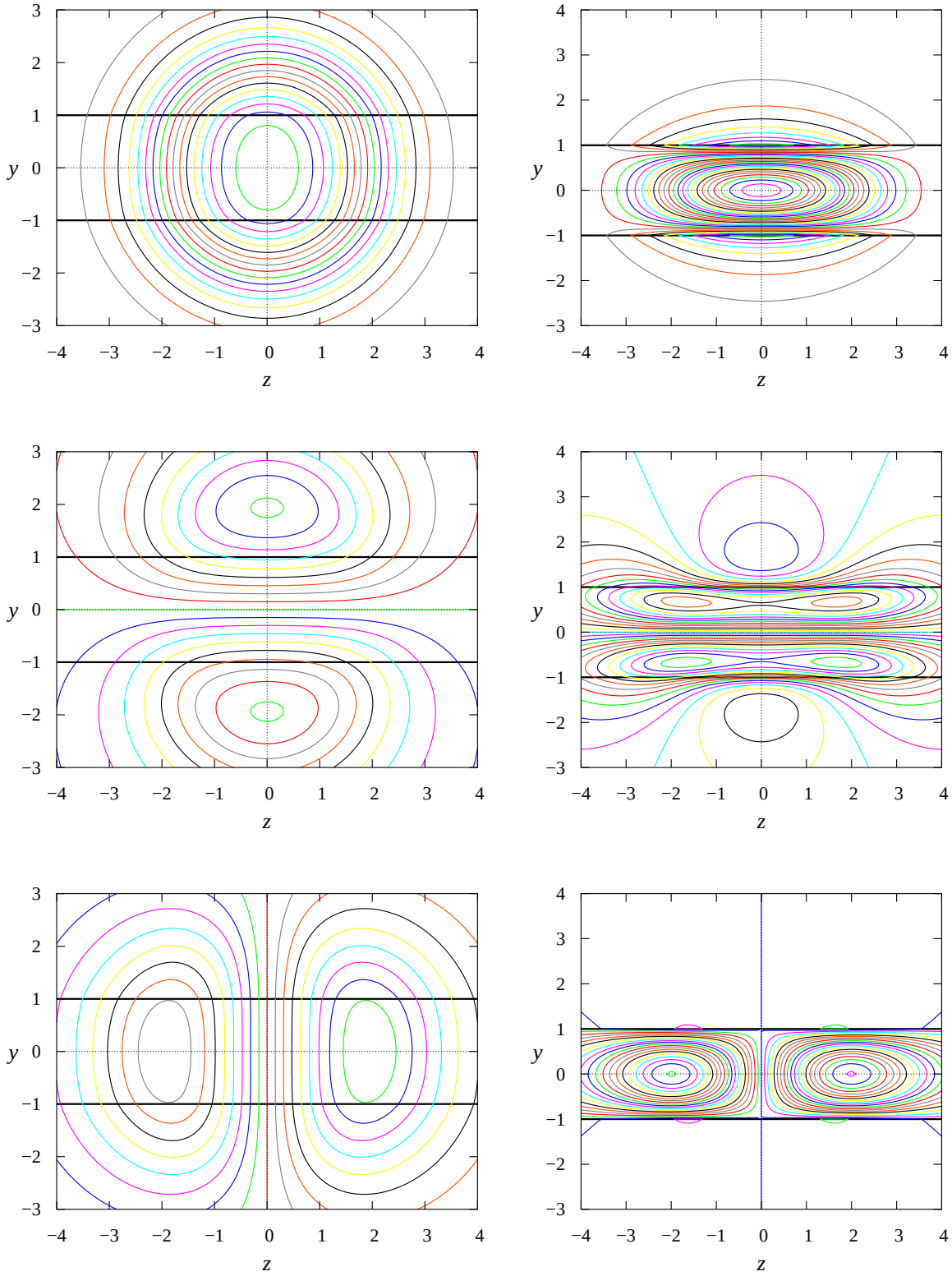

Figure 38: Isolines of the real (left) and imaginary (right) parts of $\hat{B}_x$ (top), $\hat{B}_y$ (middle) and $\hat{B}_z$ (bottom) in the $x = 0$ plane for $\bar{\omega} = 1$ and $Rm = 0$ induced by a circular current loop of radius $r_c = 2$ placed parallel to the (y, z)-plane at $\vec{x}_c = (2, 0, 0)$.

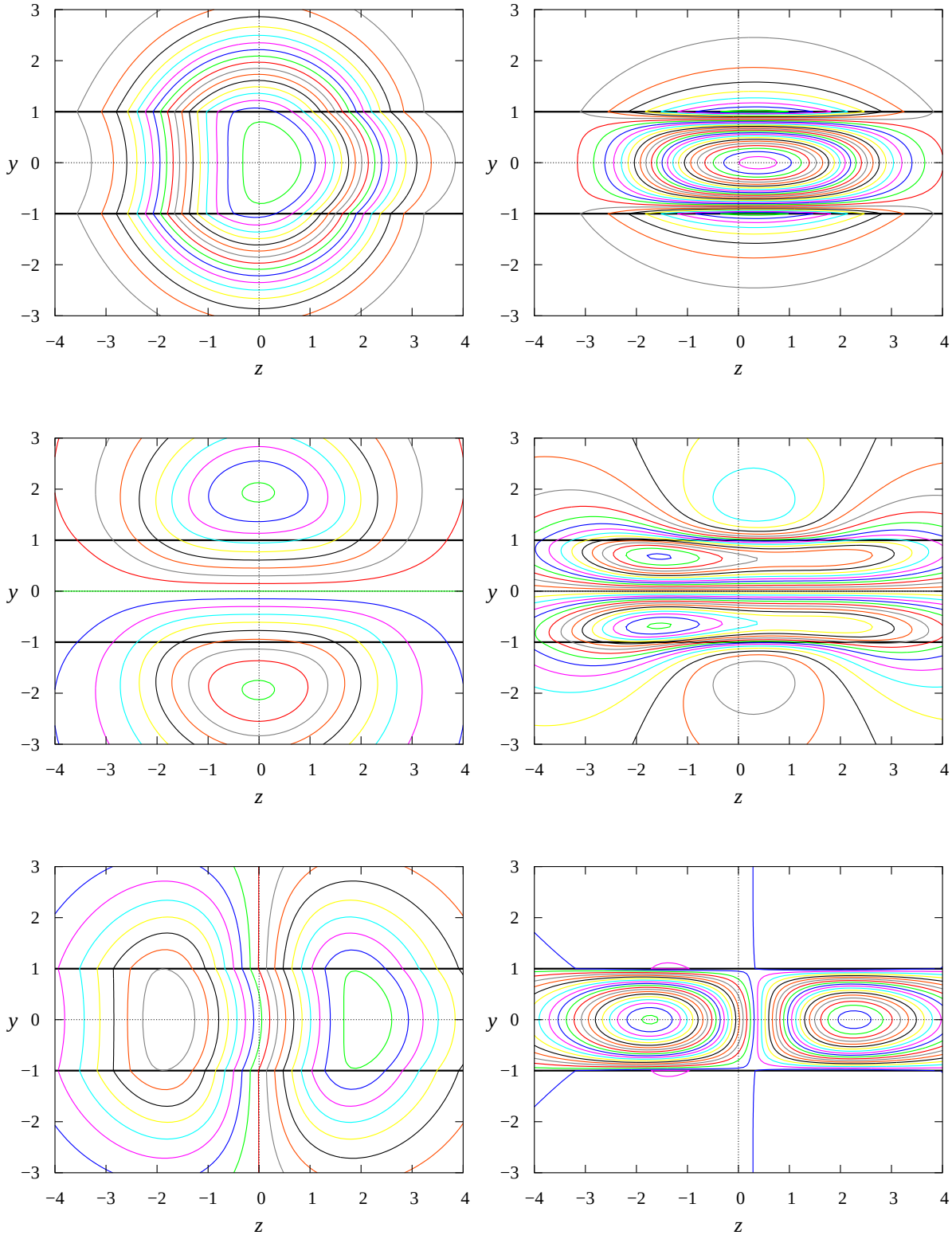

Figure 39: Isolines of the real (left) and imaginary (right) parts of $\hat{B}_x$ (top), $\hat{B}_y$ (middle) and $\hat{B}_z$ (bottom) in the $x = 0$ plane for $\bar{\omega} = 1$ and $Rm = 1$ induced by a circular current loop of radius $r_c = 2$ placed parallel to the (y, z)-plane at $\vec{x}_c = (2, 0, 0)$.

7 Conclusions

This work has introduced three models which are designed to be used for the development of eddy current flowmeters. In chapter 4 a 2D model was used to investigate improvements to the phase shift flowmeter. Secondly, in chapter 5 a axisymmetric cylindrical model was introduced which was designed to investigate the pulsed field, or transient eddy current, flowmetering technique. Finally, the mathematical basis for a fully three dimensional cylindrical model was presented in chapter 6 as a means for future investigation.

7.1 Rescaled Phase Shift Flowmeter

The concept of an improved phase shift flowmeter has been presented in chapter 4. The rescaled measurement scheme which has been presented is much less susceptible to the variation of the electrical conductivity of a liquid metal flow than the original design introduced in [31]. The rescaling has been carried out by introducing a second phase shift to the measurement scheme. Previously, only the internal phase shift which is induced by the flow and taken as a measurement between two receiving coils was considered. In this work, the external phase shift was introduced which is the phase shift between the sending and receiving coils. In contrast to the internal phase shift, the external phase shift is relatively unaffected by the velocity of the flow and depends predominantly on the conductivity of the layer. By rescaling the internal phase shift with the external, a measurement scheme is produced which can strongly reduce the effect of conductivity on the velocity measurements. For a reasonable range of conductivities the effect has been shown to be virtually eliminated. Multiple approaches to this rescaling were investigated and two effective rescalings were found. The choice between these two rescalings depends on the ac frequency of the applied field. At low frequencies $\bar{\omega} \lesssim 1$, when the phase shift varies directly with the frequency, the conductivity can be eliminated by rescaling the internal phase shift with the square of the external phase shift. At higher ac frequencies $\bar{\omega} \gtrsim 1$, where the shielding effect makes the variation of phase with the frequency non-linear, the conductivity can be eliminated by rescaling the internal phase shift directly with the external one. Note that for the example of a liquid sodium flow with $\sigma = 8.3 \times 10^6\,\mathrm{S/m}$ and channel half width giving the characteristic size as $H \sim 0.1\,\mathrm{m}$ the dimensionless parameters $\bar{\omega} \sim 1$ and $Rm \sim 1$ correspond to ac frequency $\frac{\omega}{2\pi} \sim 60\,\mathrm{Hz}$ and velocity $v \sim 1\,\mathrm{m/s}$, respectively.

The applicability of the first rescaling is limited to relatively low frequencies, especially for realistic sending coils which generate the magnetic field dominated by long-wave harmonics. A potential disadvantage of using low ac frequencies may be the relatively low sensitivity of the phase-shift flowmeter. From this point of view, it seems more attractive to operate the flowmeter in the frequency range with a moderate shielding effect where the second (direct) rescaling is applicable. The results presented in this

chapter may be useful for designing a next-generation phase-shift flowmeter which will have increased robustness to the variations of the electrical conductivity of liquid metal, which may be required in some metallurgical and other applications.

7.2 Transient Eddy Currents

A numerical investigation has been carried out into the transient transient eddy-current flowmetering method for liquid metal applications. The principle of the transient eddy current design is to create an eddy current, for example with a pulse of a magnetic field, and then somehow track the current as it is advected by a conducting flow. The eigenvalue analysis showed that eddy currents decay by roughly three orders of magnitude during the characteristic magnetic diffusion time, given by $\tau_m = \mu_0 \sigma R^2$, which is about 0.1s for a typical liquid sodium flow with $\sigma = 8.3 \times 10^6\,\mathrm{S/m}$ [28] with the length scale given by the radius of the pipe, of $R = 0.1\mathrm{m}$. A consequence of this is that the distance travelled by an eddy current during the time it is measurable scales with Rm. Thus for for small Rm the measurement device must be placed sufficiently close to the generating coil(s).

Several measurement systems were investigated, tracking different features of the eddy current distribution. These features which were considered were the zero crossing points of the magnetic flux and the extrema and spatial derivatives. The temporal derivative is equivalent to the emf, $\mathcal{E}$, and the extrema are identified by the zero crossing in the derivatives. Alongside the emf, the extrema given by zero crossings in its temporal and spatial derivatives were also investigated. The number of measurement coils which are required varies between the types of extrema. Temporal extrema requires only one loop whilst spatial extrema require two measurement coils to detect.

With a mono-harmonic eddy current distribution, the zero crossings of the emf and its spatial extrema behave in the same way, and remain separated by a quarter wavelength. The velocity of the flow can be calculated by $v = z/t$ where t is the time after the pulse generating the eddy current when the value of $\mathcal{E}$ or $\partial_z \mathcal{E}$ passes through zero at and z is the distance the zero crossing has travelled during that time. The temporal extrema of the emf follow after the zero crossing which complicates the measurement scheme as this delay depends on the conductivity of the medium as well as the eddy current distribution. This delay can be removed by using two pick-up coils placed at z_1 and z_2 then the velocity of the medium can be found as $v = (z_2 - z_1)/(t_2 - t_1)$, where t_1 and t_2 are the times at which temporal extrema are detected in the respective coil, note that the measurement loops must be sufficiently far from the initial zero crossing point.

More realistic eddy current distributions were considered. These were generated by either two anti-symmetric circular current loops or a single current loop. In the anti-symmetric set-up, the zero crossing point of emf as well as the subsequent temporal extremum was found to travel synchronously with the medium in the same way as with

the mono-harmonic wave considered before. But this was not the case for the two spatial extrema which appear at both current loops in this set-up. These two extrema were found to move at substantially different velocities from that of the medium. This result highlights the crucial importance of symmetry. The symmetry holds for zero crossing points of emf but not for the two spatial extrema in the anti-symmetric set-up. In a single-loop set-up where a a spatially symmetric eddy current distribution is generated, the spatial extremum of emf was found to travel synchronously with the medium, as was the case in the mono-harmonic wave. In this set-up, the velocity of the medium can be determined by also tracking axial extremum of the magnetic flux, which coincides with the zero crossing of the radial component of the magnetic field. It has to be noted that because of the initial tilt of the magnetic flux lines in the direction motion, the extremum of magnetic flux arrives at a given observation point ahead that of emf. This time lead can be eliminated similarly to the delay of temporal extremum of emf by using two sensors as discussed above.

Finally, we analysed the effect of a possible current asymmetry in the two-loop set-up, and showed that it gives rise to a drift of the emf zero crossing point. this leads to the conclusion that symmetry of the system is crucial for transient-eddy flowmetering. It can be inferred that a tilted single loop would also lead to an asymmetric initial eddy current distribution and would give rise to a drift of the emf zero crossing point. Asymmetry of a few per cent was found to result in the zero drift with a dimensionless velocity $Rm \sim 0.1$. For the characteristic parameters used at the beginning of this section, the respective physical velocity is $v \sim 0.1\,\mathrm{m/s}$. It means that with this level of asymmetry, which is not unlikely in practice, transient eddy current flowmetering can be reliable only for the flows with $Rm \gtrsim 1$. At lower velocities, a more accurate symmetry adjustment or calibration of the device may be required. The results of this study may be useful for designing more accurate and reliable transient eddy-current flowmeters for liquid metals.

7.3 Three Dimensional Model

The mathematical background for a three dimensional model had been derived. This model is designed to provide a framework for modelling contactless electromagnetic flowmeters, specifically for eddy current flowmeters such as the phase shift flowmeter or a transient eddy current flowmeter. The model has been designed to operate with a simple uniform flow profile defined by the magnetic Reynolds number of the flow. The models is designed with fields generated by alternating currents in mind and a dimensionless frequency is another input to the system. A set of boundary conditions for solving the model along with justification for there validity is also presented.

A technique for applying this model for a arbitrary exciting coils along with results for some simple coil designs are included, with the simple coil designs the possibility of

multiple coils is introduced. The arbitrary nature of the shape of the coil has not been displayed however as the coil is represented by a series of straight wire elements any wire is possible from simple polygons to complex solenoidal designs. This model was created to support research into liquid metal flowmeters. In its current state it can be used recreate some existing flowmeters to investigate improving accuracy and sensitivity of the sending and receiving coils, though varied coil designs. With the addition of a pulsed field approach, which can be implemented in a nearly identical way to chapter 5 this model could be used to further test the effect of asymmetry such as investigating the tilted single loop discussed above. In further work this model could serve as a basis for introducing a simple flow profile into these models, such as a Poiseuille flow, which would take the model closer still to reality. The limit of the calculation domain based on the current layer can be simply removed by utilising the solution for the coil as the applied field throughout the free space in the model, allowing inclusion of measurement coils further from the pipe.

References

[1] Milton Abramowitz and Irene A Stegun. *Handbook of mathematical functions: with formulas, graphs, and mathematical tables*, volume 55. Courier Corporation, 1964.

[2] Aleksej Alekseevič Abrikosov. *Fundamentals of the Theory of Metals*, volume 1. 1988.

[3] Roger C Baker. Electromagnetic flowmeters for fast reactors. *progress in Nuclear Energy*, 1(1):41–61, 1977.

[4] I Bucenieks. Modelling of rotary inductive electromagnetic flowmeter for liquid metals flow control. In *Proc. 8th Int. Symp. on Magnetic Suspension Technology, Dresden, Germany, 26–28 September*, pages 204–8, 2005.

[5] D Buchenau, S Eckert, and S Lenk. Contactless flow rate measurements in metallic melts. *tm–Technisches Messen*, 81(2):70–79, 2014.

[6] L Bühler, C Mistrangelo, J Konys, R Bhattacharyay, Q Huang, D Obukhov, S Smolentsev, and M Utili. Facilities, testing program and modeling needs for studying liquid metal magnetohydrodynamic flows in fusion blankets. *Fusion Engineering and Design*, 100:55–64, 2015.

[7] Jae-Eun Cha, Yeh-Chan Ahn, Kyung-Woo Seo, Ho Yun Nam, Jong Hyun Choi, and Moo Hwan Kim. The performance of electromagnetic flowmeters in a liquid metal two-phase flow. *Journal of nuclear science and technology*, 40(10):744–753, 2003.

[8] John Cockcroft. The united kingdom atomic energy authority and its functions. *British Journal of Applied Physics*, 7(2):43, 1956.

[9] MD Cowley. Flowmetering by a motion induced magnetic field. *J. Sci. Instrum.*, 42(6):406, 1965.

[10] Peter Alan Davidson. *An introduction to magnetohydrodynamics*, volume 25. Cambridge university press, 2001.

[11] N Dubovikova, C Karcher, and Y Kolesnikov. Velocity and flow rate measurement of liquid metal by contactless electromagnetic lorentz force technique. In *IOP Conference Series: Materials Science and Engineering*, volume 143, page 012022. IOP Publishing, 2016.

[12] Nataliia Dubovikova, Christian Resagk, Christian Karcher, and Yuri Kolesnikov. Contactless flow measurement in liquid metal using electromagnetic time-of-flight method. *Measurement Science and Technology*, 27(5):055102, 2016.

[13] Duncombe Edward. Some instrumental techniques for hostile environments. *Journal of Physics E: Scientific Instruments*, 17(1):7, 1984.

[14] Michael Faraday. *Experimental researches in electricity*, volume 3. Cambridge University Press, 2012.

[15] P.V. Farrell. Optical correlator method and apparatus for particle image velocimetry processing, April 30 1991. US Patent 5,011,278.

[16] Concetta Fazio, VP Sobolev, A Aerts, S Gavrilov, K Lambrinou, P Schuurmans, A Gessi, P Agostini, A Ciampichetti, L Martinelli, et al. Handbook on lead-bismuth eutectic alloy and lead properties, materials compatibility, thermal-hydraulics and technologies-2015 edition. Technical report, Organisation for Economic Co-Operation and Development, 2015.

[17] Chi-Chau Feng, WE Deeds, and CV Dodd. Analysis of eddy-current flowmeters. *Journal of applied physics*, 46(7):2935–2940, 1975.

[18] Jan Forbriger and Frank Stefani. Transient eddy current flow metering. *Meas. Sci. Technol.*, 26(10):105303, 2015.

[19] Christiane Heinicke. Spatially resolved measurements in a liquid metal flow with lorentz force velocimetry. *Experiments in fluids*, 54(6):1560, 2013.

[20] YA Hussain and RC Baker. Optimised noncontact electromagnetic flowmeter. *J. Phys. E: Sci. Instrum.*, 18(3):210, 1985.

[21] Madhusudan H Kamdar. Embrittlement by liquid metals. *Progress in Materials science*, 15(4):289–374, 1973.

[22] A_ Kolin. An electromagnetic flowmeter. principle of the method and its application to bloodflow measurements. *Proceedings of the Society for Experimental Biology and Medicine*, 35(1):53–56, 1936.

[23] N Krauter, S Franke, G Gerbeth, S Eckert, F Stefani, O Gastaldi, M Girard, Helmholtz-Zentrum Dresden-Rossendorf, and CEA Cadarache Center. Eddy current flowrate and local ultrasonic velocity measurements in liquid sodium. *Fast Reactors and related Fuel Cycles*, 2017.

[24] N. Krauter and F. Stefani. Immersed transient eddy current flow metering: a calibration-free velocity measurement technique for liquid metals. *Meas. Sci. Technol.*

[25] M Kumar, Ph Tordjeman, W Bergez, M Cavaro, K Paumel, and JP Jeannot. Towards quantitative void fraction measurement with an eddy current flowmeter for fourth generation sodium cooled fast reactors: A simplified model. *IEEE Transactions on Nuclear Science*, 63(3):1471–1476, 2016.

[26] H. Lehde and W.T. Lang. Device for measuring rate of fluid flow, 1948.

[27] Edward J McHale, Yousif A Hussain, Michael L Sanderson, and John Hemp. Capacitively-coupled magnetic flowmeter, 1985.

[28] U Muller and L Buhler. Magnetofluiddynamics in channels and containers springer. *Berlin Heidelberg*, 2001.

[29] Frederick Olmsted. Phase detection electromagnetic flowmeter-design and use. *IRE Trans Bio-Med Electron*, 9(2):88–92, 1962.

[30] J Priede, D Buchenau, and G Gerbeth. Force-free and contactless sensor for electromagnetic flowrate measurements. *Magnetohydrodynamics*, 45(3):451–458, 2009.

[31] Jānis Priede, Dominique Buchenau, and Gunter Gerbeth. Contactless electromagnetic phase-shift flowmeter for liquid metals. *Meas. Sci. Technol.*, 22:055402, 2011.

[32] Jānis Priede, Dominique Buchenau, and Gunter Gerbeth. Single-magnet rotary flowmeter for liquid metals. *J. Appl. Phys.*, 110(3):034512, 2011.

[33] Pike Edward Roy. Laser doppler velocimetry, February 11 1975. US Patent 3,866,055.

[34] JA Shercliff. Improvements in or relating to electromagnetic flowmeters, 1960.

[35] John Arthur Shercliff. *The theory of electromagnetic flow-measurement*. CUP Archive, 1987.

[36] Charles G Smith and Joseph Slepian. Electromagnetic ship's log., December 11 1917. US Patent 1,249,530.

[37] MP Spencer and AB Denison. The square-wave electromagnetic flowmeter: theory of operation and design of magnetic probes for clinical and experimental applications. *IRE Trans. Med. Electron.*, (4):220–228, 1959.

[38] Frank Stefani, Thomas Gundrum, and Gunter Gerbeth. Contactless inductive flow tomography. *Phys. Rev. E*, 70(5):056306, 2004.

[39] S Sureshkumar, Mohammad Sabih, S Narmadha, N Ravichandran, R Dhanasekharan, C Meikandamurthy, G Padmakumar, R Vijayashree, V Prakash, and KK Rajan. Utilization of eddy current flow meter for sodium flow measurement in fbrs. *Nuclear engineering and Design*, 265:1223–1231, 2013.

[40] Mahmoud Tarabad and Roger C Baker. Computation of pulsed field electromagnetic flowmeter response to profile change. *Journal of Physics D: Applied Physics*, 16(11):2103, 1983.

[41] Andr Thess, Evgeny V Votyakov, and Yurii Kolesnikov. Lorentz force velocimetry. *Phys. Rev. Lett.*, 96(16):164501, 2006.

[42] André Thess, Evgeny Votyakov, Bernard Knaepen, and Oleg Zikanov. Theory of the lorentz force flowmeter. *New J. Phys.*, 9(8):299, 2007.

[43] XJ Wang, TE Milner, and JS Nelson. Characterization of fluid flow velocity by optical doppler tomography. *Optics letters*, 20(11):1337–1339, 1995.

[44] André Wegfrass, Christian Diethold, Michael Werner, Thomas Fröhlich, Bernd Halbedel, Falko Hilbrunner, Christian Resagk, and André Thess. A universal non-contact flowmeter for liquids. *Applied physics letters*, 100(19):194103, 2012.

[45] David E Wiegand. Summary of an analysis of the eddy-current flowmeter. *IEEE Transactions on Nuclear Science*, 15(1):28–36, 1968.

[46] EJ Williams. The induction of electromotive forces in a moving liquid by a magnetic field, and its application to an investigation of the flow of liquids. *Proceedings of the physical society*, 42(5):466, 1930.

[47] B. D. Zheigur and G. Y. Sermons. Pulse method of measuring the rate of flow of a conducting fluid. *Magnetohydrodynamics*, (1):101–104, 1965.

A Appendix

A.1 Code Files

A.1.1 Phase Shift Flowmeter Code for Chapter 4

```
function [Ar]=TwoD_simple(rm,wbar,k,xrange,yrange)
  % Solution for a field genreated by standing harmoninc wave
  %
  % Axy=flowmeter.TwoD_simple(1,1,1,-5:0.1:5,-2:0.1:1)

  %%%%%%%%%%%%%%%%%%%%%%%%%    Calc Ay+ & Ay-    %%%%%%%%%%%%%%%%%%%%%%%%%
  Arp=zeros(size(yrange,2),size(xrange,2));
  [ka,c0,c1,c2,c3,d2]=coeffs(k);
  for m=1:numel(yrange)
    y=yrange(m);
    for n=1:numel(xrange)
      x=xrange(n);
      Arp(m,n)=A(y,k)*exp(1i*k*x);
    end
  end

  [ka,c0,c1,c2,c3,d2]=coeffs(-k);
  Arn=zeros(size(yrange,2),size(xrange,2));
  for m=1:numel(yrange)
    y=yrange(m);
    for n=1:numel(xrange)
      x=xrange(n);
      Arn(m,n)=A(y,-k)*exp(1i*-k*x);
    end
  end

  %%%%%%%%%%%%%%%%%%%%%%% Combines Ay+ & Ay- into A %%%%%%%%%%%%%%%%%%%%%%%
  Ar=1/2*(Arp+Arn);

  %%%%%%%%%%%%%%%%%%%%%%%%%%%%  NESTED FUNCTIONS  %%%%%%%%%%%%%%%%%%%%%%%%%%%%
  %%%%%%%%%%%%%%%%%%%%%%%%%%%%%%%% Solution %%%%%%%%%%%%%%%%%%%%%%%%%%%%%%%%
  function res=A(y,k)
    if y<=-1
      res=c3*exp(abs(k)*(y+1));
    elseif y>=1
      res=c0*exp(abs(k)*(y-1))+c1*exp(-1*abs(k)*(y-1));
    else
      res=c2*sinh(ka*y)+d2*cosh(ka*y);
    end
  end
  %%%%%%%%%%%%%%%%%%%%%%%%%%%%  Coefficients  %%%%%%%%%%%%%%%%%%%%%%%%%%%%
```

```
42   function [ka,c0,c1,c2,c3,d2]=coeffs(k)
43     ka=sqrt(k^2+1i*(wbar+k*rm));
44     c0=1/(k^2);             %sets amplitude of function based on k
45     c2=c0*abs(k)/(abs(k)*sinh(ka)+ka*cosh(ka));
46     d2=c0*abs(k)/(abs(k)*cosh(ka)+ka*sinh(ka));
47     c1=d2*cosh(ka)+c2*sinh(ka)-c0;
48     c3=d2*cosh(ka)-c2*sinh(ka);
49   end
50 end
```

```
function [Axy,X,Y]=TwoD_2wire(rm,wbar,N,xlimit,Y,s,h1,h2)
  % Solution for a field genreated by 2 wires
  %
  % Axy=flowmeter.TwoD_2wire(0,1,1024,5,-2:0.1:1.5,1,1,1)
  % for specific y values enter y_step_size as a cell containing the
  % required y value caclulation is made for x in the range
  % -1*xlimit > x => xlimit with x step size 2*xlimit/N
  %
  % wire positions are given by s, h & h1 with the wires being located in
  % the two positions given by (-s,1+h1) and (s,1+h2), thus symmetrically
  % about the y axis as a distace of s and heights h1 and h2 above the flow
  %
  % options for output [Axy],[Axy,X],[Axy,X,Y]

  %%%%%%%%%%%%%%%%%%%%%%%%% SETUP VARIABLES %%%%%%%%%%%%%%%%%%%%%%%%%%%%%%%
  % setup variables
  J = fftshift(-N/2:N/2-1);
  klimit=N*pi/xlimit;
  K=J*klimit/N;
  h1=h1+1; h2=h2+1;   % as field generated h above boundary at 1

  %%%%%%%%%%%%%%%%%%%%%%%%%%%%%%%%  SOLUTION   %%%%%%%%%%%%%%%%%%%%%%%%%%%%%
  % genreates A(hat)(y:k)
  Ayk=complex(zeros(size(Y,2),size(J,2))); % Matrix to be filled in loop

  for iK=1:N                                    % k counter
    k=K(iK);                                    % current k value
    [ka,c1,c2,c3,d2]=coeffs(k,wbar,rm,s,h1,h2); % generates coefficients
    Ayk(:,iK)=A(Y,k,ka,c1,c2,c3,d2,s,h1,h2);    % generate A(hat)(y;k)
  end

  %%%%%%%%%%%%%%%%%%%%%%%% Inverse Fourier Transform %%%%%%%%%%%%%%%%%%%%%%%
  % calulate inverse dicrete fourier transform of A(hat)
  Axy=fftshift( ifft(Ayk,[],2) ,2);
  % generates X values as second output if varargout exits
  X=((2*xlimit/N)-xlimit):(2*xlimit/N):xlimit;
end


%%%%%%%%%%%%%%%%%%%%%%%%%%%%%   SUB-FUNCTIONS   %%%%%%%%%%%%%%%%%%%%%%%%%%%%%
%%%%%%%%%%%%%%%%%%%%%%%%%%%%% Coefficient Function %%%%%%%%%%%%%%%%%%%%%%%%%%
function [ka,c1,c2,c3,d2]=coeffs(k,wbar,rm,s,h1,h2)
  ka=sqrt(k^2+1i*(wbar+k*rm));

  c0=A0(1,k,s,h1,h2);

```

```
  c2=c0*abs(k)/(abs(k)*sinh(ka)+ka*cosh(ka));
  d2=c0*abs(k)/(abs(k)*cosh(ka)+ka*sinh(ka));
  c1=d2*cosh(ka)+c2*sinh(ka)-c0;
  c3=d2*cosh(ka)-c2*sinh(ka);
end

%%%%%%%%%%%%%%%%%%%%%%%%  Function for solution  %%%%%%%%%%%%%%%%%%%%%%%%
function res=A(y,k,ka,c1,c2,c3,d2,s,h1,h2)
  belowLayer = y<-1;
  aboveLayer = y>1;
  inLayer = ~(belowLayer | aboveLayer);
  res = complex(zeros(numel(y),1));

  if any(belowLayer)
    res(belowLayer) = c3*exp(abs(k)*(y(belowLayer)+1));
  end
  if any(aboveLayer)
    res(aboveLayer) = A0(y(aboveLayer),k,s,h1,h2)...
                                      + c1*exp(-1*abs(k)*(y(aboveLayer)-1));
  end
  if any(inLayer)
    res(inLayer) = c2*sinh(ka*y(inLayer))+d2*cosh(ka*y(inLayer));
  end

end

%%%%%%%%%%%%%%%%%%%%%%%%%%  A0(y;k) function  %%%%%%%%%%%%%%%%%%%%%%%%%%
function res=A0(y,k,s,h1,h2)
  if round(k*10000)==0;
    res=zeros(size(y));  % if k close to 0, A0(y;k) set to 0
  else
    res= exp( 1i*k*s)*exp(-1*abs(k*(y-h1)))/(2*abs(k))...
      -exp(-1i*k*s)*exp(-1*abs(k*(y-h2)))/(2*abs(k));
  end
end
```

A.1.2 Transient Eddy Current Flowmeter Code for Chapter 5

```
function [ Adt,z ] = Cycol_squarewave_2wire(rm,Ff,N,zlimit,r,s,h,nPoints...
                                                              ,tau,padTo)
  %FLOWMETER_Cycol_SQUAREWAVE_2wire
  % Axisymmetric model with field generate by 2 wires with pulsed current.
  % Adt = flowmeter.Cycol_squarewave_simple(x,y,k,Rm,Ff,nPoints,tau,padTo)
  freqs = waveshape_frequencies(nPoints,Ff);
  ftpdt = waveshape_gaussianFilter_squareWave_derivative( nPoints,tau );
  data = complex(zeros(N,numel(r),nPoints)); % prealloc
  for ifreq = 1:nPoints
    if freqs(ifreq)==0
      data(:,:,ifreq)=0;
    else
      data(:,:,ifreq)=Cycol_2wire(r,N,zlimit,rm,freqs(ifreq),h,s);
    end
  end % generate solutions for frequencies
  if ~exist('padTo','var'); padTo = numel(points); end
  [Adt] = waveshape_ifft_PaddingAndDerivative(data,ftpdt,padTo);
  if nargout>1
    [~,z] = Cycol_2wire(r,N,zlimit,0,1,h,s);
  end
end

%%%%%%%%%%%%%%%%%%%%%%%%%%%%%% SUB FUNCTIONS %%%%%%%%%%%%%%%%%%%%%%%%%%%%%%
function [ frequencies ] = waveshape_frequencies( nPoints,...
                                                    FundamentalFrequency )
  %TOOLS_WAVESHAPE_FREQUENCIES
  % generates frequencies form numebr of points nad fundamental frequency
  frequencies = (0:FundamentalFrequency:(nPoints-1)*...
                    FundamentalFrequency) - FundamentalFrequency*nPoints/2;
end

function [ ftpdt ] = waveshape_gaussianFilter_squareWave_derivative(...
                                                              nPoints,tau)
  %TOOLS_WAVESHAPE_GAUSSIANFILTER_SQUAREWAVE_DERIVATIVE
  % ftpdt = WAVESHAPE_GAUSSIANFILTER_SQUAREWAVE_DERIVATIVE( nPoints,tau )
  % generates fourier transform of time derivative of square wave with a
  % gaussian filter with nPoints and a halfwidth of the peaks of tau
  tu = nPoints/4;          % index of upward peak
  td = 3/4*nPoints-1;      % index of downward peak
  height = 1 ;             % maximum height of peaks
  Au = height;             % set height up
  Ad = -height;            % set height down
  tp = 1:nPoints;          % time indicies
  if tau == 0
    % do not apply filter
```

```
    pdt = zeros(size(tp));
    pdt([tu,td+1])=[Au,Ad];
  else
    % derivative of points (with gaussian filter if tau ~=0)
    pdt = Au*(exp(-1*((tp-tu)/tau).^2)) + Ad*(exp(-1*((tp-td)/tau).^2));
  end
  ftpdt = fftshift(fft(pdt));   % generate ftpointsdt
end

function [A,z] = Cycol_2wire(r,N,zlimit,rm,wbar,h,s)
  % solution for 2 wire axisymmetric model ac with frequency wbar
  k = localGenerateK(N,zlimit);
  A = RKSolution(r,k,rm,wbar,h,s); % generate A(k,r)
  A = fftshift(ifft(A,[],1),1); % transform to A(z,r)
  A = bsxfun(@times,r.',A.');% rescale and convert A(z,r) to A(r,z)
  if nargout>1
    z=((2*zlimit/N)-zlimit):(2*zlimit/N):zlimit;
  end
end

function k = localGenerateK(N,zlimit)
  J = fftshift((-N/2):(N/2 -1));
  k = J*pi/zlimit;
end

function Ark = RKSolution(r,k,rm,wbar,h,s)
  % Generates A(r,k) from A(r)
  Ark = complex(zeros(numel(k),numel(r))); % prealloc
  for ik = 1:numel(k)
    if k(ik) == 0 % tolerance?
      Ark(ik,:) = 0;
      continue
    end
    Ark(ik,:) = RSolution(r,k(ik),wbar+k(ik)*rm,h,s);
  end
end

function [Ar] = RSolution(r,k,wbar,h,s)
  % generates A(r)
  % logical indices
  in_layer = r<1;
  layer_to_wire = (r<h) & ~in_layer;
  beyond_wire = r>=h;
  % prealloc
  Ar = complex(zeros(1,numel(r)));
  A0 = Azero(h,k,s);
  k=abs(k);
```

```
93    [A,C,D] = coeffs(k,wbar,h);
94    if any(in_layer)
95      Ar(in_layer) = A0*D* besseli(1, kappa(k,wbar)*r(in_layer) );
96    end
97    if any(layer_to_wire)
98      Ar(layer_to_wire)= A0*besseli(1, k*r(layer_to_wire)) +...
99                                      A0*C* besselk(1, k*r(layer_to_wire) );
100   end
101   if any(beyond_wire)
102     Ar(beyond_wire) = A0*A*besselk(1, k*r(beyond_wire)) +...
103                                        A0*C*besselk(1, k*r(beyond_wire) );
104   end
105 end
106
107 function A0 = Azero(h,k,s)
108   % Calulates A0
109   bkh = besselwrapper(abs(k)*h);
110   I0 = bkh(1);
111   I1 = bkh(2);
112   K0 = bkh(3);
113   K1 = bkh(4);
114   A0 = h*2*1i*sin(k*s)*K1 /( abs(k)*( I0*K1 + K0*I1));
115 end
116
117 function [A,C,D] = coeffs(k,wbar,h)
118   x = kappa(k,wbar);
119   bk = besselwrapper(k);
120   bx = [besseli(0,x), besseli(1,x)];
121   A = besseli(1,k*h)./besselk(1,k*h);
122   C = ( -x * bk(2)/bx(2) + k * bk(1)/bx(1) )./ ...
123                                      (  x * bk(4)/bx(2) + k * bk(3)/bx(1) );
124   D = (  k * bk(2)/bk(4) + k * bk(1)/bk(3) )./ ...
125                                      (  k * bx(2)/bk(4) + x * bx(1)/bk(3) );
126 end
127
128 function out = kappa(k,wbar)
129   out = sqrt(k^2+1i*wbar);
130 end
131
132 function [out] = besselwrapper(in)
133   % wrapper funciton for bessel functions
134   out = zeros(numel(in),4);
135   out(:,1) = besseli(0,in);
136   out(:,2) = besseli(1,in);
137   out(:,3) = besselk(0,in);
138   out(:,4) = besselk(1,in);
139 end
```

```
140
141 function [Adt] = waveshape_ifft_PaddingAndDerivative(data,ftpdt,padTo)
142   %TOOLS_WAVESHAPE_IFFT_PADDINGANDDERIVATIVE
143   % Adt = TOOLS_WAVESHAPE_IFFT_PADDINGANDDERIVATIVE(data,ftpdt,padTo)
144   % calculates idft of data scaled with ftpdt in 3rd dimension
145   % optional 3rd input allows symmetric padding of the spectrum
146   Adt = bsxfun(@times,data,permute(ftpdt,[3,1,2]));
147   if nargin>2
148     if padTo>size(Adt,3)
149       Adt = localSymmetricPadArrayIn3rdDimension(Adt,padTo);
150     end
151   end
152   Adt=real(ifft(ifftshift(Adt,3),[],3));
153 end
154
155 function out = localSymmetricPadArrayIn3rdDimension(array,padTo)
156   % Pad array (in spectral space) for finer resolution in real.
157   out = complex(zeros(size(array,1),size(array,2),padTo));
158   arrayStart = floor((padTo-size(array,3))/2);
159   arrayEnd = arrayStart+size(array,3)-1;
160   out(:,:,arrayStart:arrayEnd)=array;
161 end
```

A.1.3 3D Model Codes for Chapter 6

```
function [New_field,TT,RR,ZZ] = Cycol_3d(inputfile,coiltype,coildim)
  %
  inputs.(inputfile);
  % Provide coil, generate field, FFT
  nR_gen = 1;
  [tt,rr,zz] = makeCylindricalPoints(...
    [-R_grid,R_grid,-Z_domain,Z_domain],[nT,nR_gen,nZ]);
  [TT,RR,ZZ] = ndgrid(tt,rr,zz);
  XX = RR.*cos(TT); YY = RR.*sin(TT);
  [wire_points] = makecoil(coiltype,coildim);
  [field] = generate_coil_field(wire_points,XX,YY,ZZ); % 'double',[-1,1]);
  [field] = field_to_cylindrical(field,TT);
  [FTfield] = fftshift(fft( fftshift(fft( field ,[],1),1) ,[],3),3);
  R = linspace(0,R_grid,nR);
  % Generate Field
  [New_field] = Scaled_main_loop(FTfield,nZ,nT,R,R_wall,R_domain,...
                                                    v,mu0,Sigma,omega,k);
  if nargout>1;[TT,RR,ZZ]=ndgrid(tt,R,zz);end
end

function [New_field] = Scaled_main_loop(FTfield,nZ,nT,...
                                      R,R_wall,R_domain,v,mu0,sigma,omega,k)
  %% Applied field coeffs ( at r=R_domain )
  AtR = FTfield(:,:,:,1); ArR = FTfield(:,:,:,2); AzR = FTfield(:,:,:,3);
  FpR = ArR+1i.*AtR; FmR = ArR-1i.*AtR;
  %% inputs for main loop
  nN = nZ; N = (-nN/2:1:nN/2-1); % z modes
  nM = nT; if nM==1; M=0; else M = (-nM/2:1:nM/2-1); end % theta modes
  %% Pre loop allocation
  r_in_flow = R < R_wall ;
  Fp = zeros(size(R)); Fm = zeros(size(R)); Az = zeros(size(R));
  Field_spec = complex(zeros(numel(M),numel(R),numel(N),3));
  %% Main loop
  fprintf('Entering main loop... \n')
  for i_n= 1:numel(N)
    %% Loop variables
    n=N(i_n); %% wavenumber in z dir
    kn = k*n;
    if n==0;kn=1e-10;end
    x=kappa(v,kn,mu0,sigma,omega); kn=abs(kn);
    %% inner loop
    for i_m=1:numel(M); % ####
      %% Loop variables
      m = M(i_m); %wavenumber in theta dir
      M_temp = [m-1 , m , m+1];
```

```
46        BESSI_x = bsxfun(@besseli, M_temp.',x*R(r_in_flow)) ;
47        BESSI_k = bsxfun(@besseli, M_temp.',kn*R(~r_in_flow));
48        BESSK_k = bsxfun(@besselk, M_temp.',kn*R(~r_in_flow));
49        %% Scaled bessel functions for boundary conditions
50        scaled = 1;
51        BESSI_r_domain = besseli(M_temp,kn*R_domain,scaled) ;
52        BESSI_r_wall_x = besseli(M_temp,x*R_wall,scaled) ;
53        BESSI_r_wall_k = besseli(M_temp,kn*R_wall,scaled) ;
54        BESSK_r_wall_k = real(besselk(M_temp,kn*R_wall,scaled)) ;
55        %% Scaling Exponents
56        Scale_Exponent_I_k_Domain =-abs(real(kn*R_domain));
57        Scale_Exponent_Dbar = -Scale_Exponent_I_k_Domain;
58        Scale_Exponent_I_x_Wall = -abs(real(x*R_wall));
59        Scale_Exponent_I_k_Wall = -abs(real(kn*R_wall));
60        Scale_Exponent_K_k_Wall = kn*R_wall;
61        %% set Dbars
62        Dbarp = FpR(i_m,1,i_n)./ BESSI_r_domain( 3 );
63        Dbarm = FmR(i_m,1,i_n)./ BESSI_r_domain( 1 );
64        Dbar  = AzR(i_m,1,i_n)./ BESSI_r_domain( 2 );
65        %% solve boundary condition matrix
66        lastwarn('')
67        [C,Cp,Cm,D,Dp,Dm] = Scaled_solve_boundary_condition_matrix(...
68          BESSI_r_wall_x(2),BESSI_r_wall_x(3),BESSI_r_wall_x(1),...
69          BESSI_r_wall_k(2),BESSI_r_wall_k(3),BESSI_r_wall_k(1),...
70          BESSK_r_wall_k(2),BESSK_r_wall_k(3),BESSK_r_wall_k(1),...
71          Dbar,Dbarp,Dbarm,...
72          Scale_Exponent_I_k_Wall,Scale_Exponent_Dbar,...
73          Scale_Exponent_K_k_Wall,R_wall,kn,x,m) ;
74        % Calculate coefficients (& remove scaling)
75        Dbarp = Dbarp.*exp(-Scale_Exponent_Dbar);
76        Dbarm = Dbarm.*exp(-Scale_Exponent_Dbar);
77        Dbar  = Dbar .*exp(-Scale_Exponent_Dbar);
78        %
79        Cp = Cp.*exp(Scale_Exponent_I_x_Wall);
80        Cm = Cm.*exp(Scale_Exponent_I_x_Wall);
81        C  = C .*exp(Scale_Exponent_I_x_Wall);
82        %
83        Dp = Dp.*exp(Scale_Exponent_K_k_Wall);
84        Dm = Dm.*exp(Scale_Exponent_K_k_Wall);
85        D  = D .*exp(Scale_Exponent_K_k_Wall);
86        % Generate field components (in and out of flow)
87        Fp( r_in_flow) = Cp.*BESSI_x(3,:) ;
88        Fp(~r_in_flow) = Dbarp*BESSI_k(3,:) + Dp*BESSK_k(3,:) ;
89
90        Fm( r_in_flow) = Cm.*BESSI_x(1,:) ;
91        Fm(~r_in_flow) = Dbarm*BESSI_k(1,:) + Dm*BESSK_k(1,:) ;
92
```

```
      Az( r_in_flow) = C.*BESSI_x(2,:) ;
      Az(~r_in_flow) = Dbar.*BESSI_k(2,:) + D*BESSK_k(2,:) ;
      % Transform back from decoupling variables
      At = 1/2i*(Fp-Fm) ;
      Ar = 1/2 *(Fp+Fm) ;
      % Store f(theta,r,z)
      Field_spec(i_m,:,i_n,1) = At ;
      Field_spec(i_m,:,i_n,2) = Ar ;
      Field_spec(i_m,:,i_n,3) = Az ;
    end
  end
  % Invert FFT
  New_field = ifft(ifft(ifftshift(ifftshift(Field_spec,3),1),[],3),[],1);
end

function [C,Cp,Cm,D,Dp,Dm] = Scaled_solve_boundary_condition_matrix(...
                      ix,ipx,imx,ik,ipk,imk,kk,kpk,kmk,Dbar,Dbarp,Dbarm,...
                            Scale_Exponent_I_k_Wall,Scale_Exponent_Dbar,...
                                          Scale_Exponent_K_k_Wall,R,k,x,m)
  Scale_Exponent_RHS = Scale_Exponent_Dbar + Scale_Exponent_I_k_Wall;
  %% Solve coefficients for Az
  LHS1 = [... C ,  D
    x*(ipx+imx) , k*(kmk+kpk) ;
    ix          , -kk         ];
  RHS1 = [...
    k*Dbar*(imk+ipk) ;
    Dbar*ik         ];
  RHS1 = RHS1*exp( -Scale_Exponent_RHS);
  SOL1 = LHS1\RHS1;
  C = SOL1(1);
  D = SOL1(2);
  %% Solve coefficients for F+-
  LHS2 = [... C+     ,    C-                ,    D+                 ,    D-
    x*ix-(m+1)/R*ipx , -(x*ix+(m-1)/R*imx) , -(-k*kk-(m+1)/R*kpk) ,...
                                                        -k*kk+(m-1)/R*kmk ;
    0                , 0                  , kk                  , kk    ;
    ipx              , 0                  , -kpk                , 0     ;
    0                , imx                , 0                   , -kmk ];
  RHS2 = [Dbarp*(k*ik-(m+1)/R*ipk) - Dbarm*(k*ik+(m-1)/R*imk)             ;
    (Dbarp+Dbarm+2i*Dbar)*ik+2i*D + 2i*D*exp(Scale_Exponent_K_k_Wall...
                                                 + Scale_Exponent_RHS) ;
    Dbarp*ipk                                                          ;
    Dbarm*imk                                                         ];
  RHS2 = RHS2*exp(-Scale_Exponent_RHS);
  SOL2 = LHS2\RHS2;
  Cp = SOL2(1); Cm = SOL2(2); Dp = SOL2(3); Dm = SOL2(4);
end
```

```
140
141 function x = kappa(v,kn,mu0,sigma,w)
142   x = sqrt( kn.^2+1i*mu0*sigma*(w+v.*kn) );
143 end
144
145 function f = generate_coil_field(wire_points,grid1,grid2,grid3)
146   % Generates field for the coil defined by wire_points
147   f=0;for icoil = 1:numel(wire_points)
148     f=f+single_coil_field(wire_points{icoil},grid1,grid2,grid3);
149   end
150 end
151
152 function [t,r,z] = makeCylindricalPoints(limits,npoints)
153   % generates cylindrical grid
154   if numel(limits)==4;limits = [-pi,pi,limits];end
155   t = linspace(limits(1),limits(2),npoints(1)+1);t(end)=[];
156   r = linspace(limits(3),limits(4),npoints(2));
157   z = linspace(limits(5),limits(6),npoints(3)+1);z(end)=[];
158 end
159
160 function  [fieldtrz] = field_to_cylindrical(fieldxyz,TT)
161   % converts cartesian field to cylindrical field
162   fieldtrz(:,:,:,1)=fieldxyz(:,:,:,2).*cos(TT)-fieldxyz(:,:,:,1).*sin(TT);
163   fieldtrz(:,:,:,2)=fieldxyz(:,:,:,1).*cos(TT)+fieldxyz(:,:,:,2).*sin(TT);
164   fieldtrz(:,:,:,3)=fieldxyz(:,:,:,3);
165 end
```

A.2 Pre-Print Papers

arXiv:1705.02939v2 [physics.ins-det] 21 Sep 2017

Numerical analysis of transient eddy-current flowmetering method

Richard Looney and Jānis Priede

Flow Measurement Research Centre, Coventry University, UK

E-mail: J.Priede@coventry.ac.uk

Abstract. We present a comprehensive numerical analysis of transient eddy-current flowmetering method for liquid metals. This type of flowmeter operates by tracking eddy-current markers excited by the magnetic field pulses in the flow of a conducting liquid. Using a simple mathematical model, where the fluid flow is replaced by a translating cylinder, a number possible alternative measurement schemes are considered. The velocity of the medium can be measured by tracking zero crossing points and spatial or temporal extrema of the electromotive force (emf) induced by transient eddy currents in the surrounding space. Zero crossing points and spatial extrema of the emf travel synchronously with the medium whereas temporal extrema experience an initial time delay which depends on the conductivity and velocity of the medium. Performance of transient eddy-current flowmetering depends crucially on the symmetry of system. Eddy current asymmetry of a few per cent makes the detection point drift with a velocity corresponding to a magnetic Reynolds number $Rm \sim 0.1$. With this level of asymmetry transient eddy-current flowmetering can be reliably applicable only to flows with $Rm \gtrsim 0.1$. A more accurate symmetry adjustment or calibration of flowmeters may be necessary at lower velocities.

Some materials have been removed due to 3rd party copyright. The unabridged version can be viewed in Lancester Library - Coventry University.

arXiv:1704.00199v2 [physics.ins-det] 21 Sep 2017

Concept of Improved Electromagnetic Phase-Shift Flowmeter for Liquid Metals with Variable Conductivity

Richard Looney and Jānis Priede

Flow Measurement Research Centre, Coventry University, UK

E-mail: J.Priede@coventry.ac.uk

Abstract. We present a concept of an improved phase-shift flowmeter that has a significantly reduced sensitivity to the variation of the electrical conductivity of a liquid metal. A simple theoretical model of the flowmeter is considered where the flow is approximated by a solid finite-thickness conducting layer moving in the presence of an ac magnetic field. In contrast to the original design [Priede et al., Meas. Sci. Technol. 22 (2011) 055402], where the flow rate is determined by measuring only the phase shift between the voltages induced in two receiving coils, the improved design measures also the phase shift between the sending and the upstream receiving coil. These two phase shifts are referred to as internal and external ones, respectively. We show that the effect of electrical conductivity on the internal phase shift, which is induced by the flow, can be strongly reduced by rescaling it with the external phase shift, which depends mostly on the conductivity of medium. Two different rescalings are found depending on the ac frequency. At low frequencies, when the shielding effect is negligible, the effect of conductivity is strongly reduced by rescaling the internal phase shift with the external one squared. At higher frequencies, the same is achieved by rescaling the internal phase shift directly with the external one.

Keywords: Electromagnetic flowmeter, liquid metal, eddy current

PACS numbers: 41.20.Gz, 47.60.Dx, 47.65.-d, 47.80.Cb

Some materials have been removed due to 3rd party copyright. The unabridged version can be viewed in Lancester Library - Coventry University.